

UC Irvine

UC Irvine Electronic Theses and Dissertations

Title

Thermal Transport in Additively Manufactured Metamaterials

Permalink

<https://escholarship.org/uc/item/7sr3n08f>

Author

Farzinazar, Shiva

Publication Date

2021

Peer reviewed|Thesis/dissertation

UNIVERSITY OF CALIFORNIA,  
IRVINE

Thermal Transport in Additively Manufactured Metamaterials

DISSERTATION

submitted in partial satisfaction of the requirements  
for the degree of

DOCTOR OF PHILOSOPHY

in Mechanical and Aerospace Engineering

by

Shiva Farzinazar

Dissertation Committee:  
Professor Lorenzo Valdevit, Chair  
Professor Ramin Bostanabad  
Professor Jaeho Lee

2021



## **DEDICATION**

*To*

*My parents, Shahla and Bijan.*

*Who believed in me, even when I didn't believe in myself.*

# TABLE OF CONTENTS

<b>LIST OF FIGURES.....</b>	<b>vi</b>
<b>LIST OF TABLES.....</b>	<b>xvii</b>
<b>ACKNOWLEDGEMENTS.....</b>	<b>xviii</b>
<b>CURRICULUM VITAE.....</b>	<b>xx</b>
<b>ABSTRACT OF THE DISSERTATION.....</b>	<b>xxiii</b>
<b>CHAPTER 1.....</b>	<b>1</b>
1.1. Motivation .....	1
1.2. Background on Thermal Metamaterials.....	2
1.3. Role of Additive Manufacturing.....	5
1.4. Heat Transfer Mechanisms in Thermal Metamaterials .....	6
1.5. Experimental Validation of Thermal Metamaterials .....	10
1.6. Outline of Doctoral Research .....	12
<b>CHAPTER 2.....</b>	<b>15</b>
2.1. Introduction to 3D Heat Guiding Structures for Thermal Management in Electronics.....	15
2.2. Topology Optimization of 3D Heat-Guiding Structures.....	19
2.2.1. Density-based Topology Optimization Algorithm Development.....	19
2.3. Results and Discussion.....	22
2.3.1. Thermo-mechanical Topology Optimization of Heat Guiding Structures .....	22
2.3.2. Thermo-Mechanical Optimization Results .....	24
2.3.3. Manufacturing and Characterization of 3D Heat-Guiding Structures.....	27
2.4. Conclusions.....	32
<b>CHAPTER 3.....</b>	<b>34</b>

3.1.	Introduction to ultralight hollow nickel microlattices.....	34
3.2.	Materials and Methods.....	36
3.3.	Results and Discussion.....	42
3.3.1.	Compression Dependent Thermal Conductivity .....	42
1.3.2.	Temperature-Dependent Thermal Conductivity .....	44
1.3.3.	Thermo-Mechanical Evaluation of Hollow Nickel Microlattices.....	45
3.4.	Conclusions.....	47
<b>CHAPTER 4.....</b>	<b>48</b>	
4.1.	Introduction to Shape Memory Polymer Microlattices .....	48
4.2.	Materials and Methods.....	50
4.3.	Results and Discussion.....	60
4.3.1.	Temperature-Dependent Thermal Conductivity of SMP Microlattices.....	60
4.3.2.	Programmable Thermal Conductance of SMP Microlattices .....	64
4.4.	Conclusions.....	71
<b>CHAPTER 5.....</b>	<b>74</b>	
5.1.	Introduction to Thermal Properties of Glassy Carbon Metamaterials .....	74
5.2.	Theoretical Approaches.....	76
5.2.1.	Phonon Transport Modeling of Carbon Nanostructures.....	76
5.3.	Materials and Experimental Approaches.....	80
5.3.1.	Fabrication of Glassy Carbon Structures .....	80
5.3.2.	Electrical Resistance Thermometry .....	80
5.4.	Results and Discussion.....	82
5.4.1.	Electrical Conductivity Measurement .....	82
5.4.2.	Thermal Conductivity Measurement .....	84
5.4.3.	Heat Capacity Measurement .....	85
5.5.	Conclusions.....	87
<b>CHAPTER 6.....</b>	<b>89</b>	
6.1.	Contributions of the Dissertation.....	90
6.2.	Future Research Directions.....	92

6.2.1. Passive thermal switches using 4D printed architected materials .....	92
6.2.2. Thermal rectification in nanoscale architected materials .....	97
<b>References .....</b>	<b>102</b>
<b>Appendix A .....</b>	<b>119</b>
A.1. View Factor Derivation .....	119

## LIST OF FIGURES

**Figure 1-1:** a) Demonstration of the heat flux when a block of material is placed between a heat source and a heat sink. Heat flux manipulation by b) thermal shielding, c) thermal concentration, and d) thermal inversion concepts..... 3

**Figure 1-2** a) Schematic of tunable multifunctional thermal metamaterials. The designed assemblies of thermal metamaterials as unit cells enable the manipulation of local heat flux for multiple functions such as thermal shifter, concentrator, diffuser, and rotator[4]. b) Schematic and fabricated device of the radiative thermal camouflage. Experimentally measured temperature profiles with an IR camera are demonstrated for a pure background, a background with an object on the surface, and an object on the surface camouflaged by the structured thermal surface. c) Co-optimized conduction and radiation-based thermal metamaterials for selective control of the heat flow through the enhanced design of both the anisotropic thermal conductivity of the emitter body and its surface emissivity..... 4

**Figure 1-3** Lattice miniaturization from mm to nm scale from reference [6]. a) Hollow nickel microlattices manufactured by SPPW polymer templates in conjunction with electroless nickel plating and removing the polymeric template [36]. b) Solid beam alumina lattice structure manufactured by P $\mu$ SL made of a hybrid of solid PEGDA and alumina nanoparticles followed by a sintering process[7]. c) Hollow-beam alumina lattice manufactured by two-photon DLW, alumina atomic layer deposition, and oxygen plasma etching of the internal polymer template [37]. d) Solid-beam glassy carbon lattice manufactured by two-photon DLW and subsequent pyrolysis at 900°C..... 6



**Figure 2-1** a) Heat transfer path in a conventional packaging scenario where heat-generating component and heat sink are aligned. In this case, components with different temperature tolerances can easily be impacted if positioned in the heat transfer path. b) Heat transfer path in a non-conventional packaging scenario where a heat sink may not be aligned with a heat source. In the presence of several components with different temperature tolerances in the system, novel heat guiding structures with zigzag or S shape designs would be favorable for optimal routing of the heat flow from the heat source to the heat sink. These heat guiding structures may create an efficient heat transfer path while minimizing the thermal interaction with the components of different temperature tolerances. c) Thermo-mechanical optimization process for complex packaging scenarios. The thermal boundary conditions include a heat flux ( $q''$ ) on the heat source side while fixing the temperature on the heat sink side ( $T_{\text{sink}}$ ). The mechanical boundary conditions represent a force applied on the heat sink side and a fixed end on the heat source side..... 19

**Figure 2-2:** Boundary conditions and the resultant thermal, mechanical, and thermo-mechanical topology optimization on the following designs. a) Initial structure with parameters of  $\theta=30$ ,  $L=10$  mm,  $W=5$  mm,  $t= 2$  mm, and  $D = 4$  mm. b) Initial structure with parameters of  $\theta=45$ ,  $L=10$  mm,  $W=7$  mm,  $t= 2$  mm, and  $D = 4$  mm. c) Initial structure with parameters of  $\theta=60$ ,  $L=10$  mm,  $W=12$  mm,  $t= 2$  mm, and  $D = 4$  mm. d) Initial structure with parameters of  $L=10$  mm,  $W=10$  mm,  $t= 2$  mm, and  $D = 4$  mm. e) Initial structure with parameters of  $L_1= 30$  mm,  $L_2=12$  mm,  $W= 15$  mm,  $t_1= 4$  mm,  $t_2= 2.5$  mm, and  $D= 15$  mm. The solid reference structures for designs (a)-(d) have identical dimensions as their representing initial structures but 2 mm thickness in the y-direction. The solid reference structure for design (e) has identical dimensions as its initial structure but with  $W/\sqrt{2} = D/\sqrt{2}= 10.6$  mm.

The infill reference structure for all designs (a)-(e) is identical to their initial design but creates a 50% volume fraction with a rectilinear infill pattern..... 25

**Figure 2-3:** Demonstration of the design (e) 3D printed steel structures after post-processing and emissivity coating. a) A reference characterization sample was fabricated for characterizing the properties of additively manufactured steel along with b) the initial structure ( $\nu = 100\%$ ), c) the reference structure with 50% volume of the initial structure ( $\nu = 50\%$ ), and d) the optimized heat guiding structure ( $\nu = 50\%$ ). ..... 28

**Figure 2-4:** a) Demonstration of the IR thermography experimental setup for the reference structure (Top) and the optimized heat guiding structure (Bottom) b) Numerical analysis of the reference sample (Top) and the optimized heat guiding structure (Bottom) with the measured boundary conditions of heat flux of  $5.1 \text{ Wcm}^{-2}$  on the top and a constant temperature of  $33 \text{ }^\circ\text{C}$  in the copper sample holder. The inset figures represent the direction of heat flow using the red arrows. While the reference structure restrictions cause the heat flux concentration in the narrow regions, the optimized heat guiding structure has an optimized distribution of material to prevent heat flux concentration. c) IR images demonstrating the temperature contour in the reference structure (Top) and the optimized heat guiding structure (Bottom). The scale bar in inset images represents 5 mm. .... 30

**Figure 3-1** a) The hollow doped nickel microlattice in addition to the unit cell with geometric features.  $\theta$  was set to  $60^\circ$  while ranges of 9-10.5mm for H, 1-2 $\mu\text{m}$  for thickness and 500-650 $\mu\text{m}$  for the diameter was explored b) Corresponding IR image of the experimental setup along with the temperature distribution of a unit cell. c) The experimental setup used for thermal conductivity measurement of hollow nickel microlattices. The applied clamps are used to change the heater's height in thermal conductivity measurement under compression.

d) The FEM simulation of the whole setup illustrates the heat transfer throughout the stack.  
 ..... 37

**Figure 3-2** Probability density function for the emissivity values of the sample2 with a darker surface finish. The image taken by the IR camera with the 25um add-on lens resolution is shown in the inset ..... 39

**Figure 3-3** Lattice structure model for radiative conductivity and notations ..... 42

**Figure 3-4** a) The strain is defined as  $\delta = (l_0 - l)/l_0$  in which  $l$  is identified in each image. Increasing the applied force causes the unit cells to slide, reducing  $\theta$  in a non-uniform manner. The representative average  $\theta$  value and volume fraction for each compression cycle is reported. b) The experimental data and analytical modeling for two samples with the same volume fraction and different surface finishes are illustrated as a function of  $\theta$  on the left axis. The analytical model is verified by the FEM results for unit cells with angles ranging from 15 to 75°. Increasing strain results in a decrease in the structural length and an increase in the structure's area. Consequently, the Fourier equation explains the reduction in the conduction contribution of the effective thermal conductivity ( $k_{eff}=ql/\Delta TA$ ). c) The radiation contribution is defined as the ratio of the radiative thermal conductivity over the effective conductivity. Reducing  $\theta$  leads to a lower contribution of radiation, correlated with reducing the effective thermal conductivity..... 43

**Figure 3-5** a) The effective thermal conductivity of the samples with 0.09% and 0.15% volume fraction values was measured as a function of temperature. The difference between the blue and red data points illustrates the contribution of surface emissivity in samples sharing the same volume fraction. The slope of the dashed lines shows the rate of growth in the effective thermal conductivity as a result of radiation contribution. b) The radiation

contribution of all samples is derived as a function of temperature while the dashed lines demonstrate the analytical modeling..... 45

**Figure 3-6** a) The design space demonstrates the potential effective thermal conductivity values as a function of volume fraction and surface emissivity using Equation (4) Beyond 1% volume fraction, all lines (representing different emissivity values) converge; demonstrating conduction as the primary mode of heat transfer. Comparatively, radiation contribution signifies below 1% volume fraction, exposing the difference in the effective thermal conductivity at a specific volume fraction. b) Hollow nickel microlattice placement in the material property plot of specific Young's modulus versus effective thermal conductivity. Dashed outlines indicate the allocated region for each material using the Ashby model for cellular solids[159], while markers represent the measured data points. Hollow nickel microlattices can obtain higher mechanical strength and lower effective thermal conductivity than other mesoscale cellular materials..... 46

**Figure 4-1** a) 4D printing of SMP microlattices using the P $\mu$ SL technique. b) Schematic of the Kelvin Foam (KF) sample with  $\theta = 45^\circ$ ,  $l_{KF} = 1380 \mu\text{m}$ ,  $d_{KF}$  ranging from  $303 \mu\text{m}$  to  $428 \mu\text{m}$  (Left) plus the Octet Truss (OT) sample with  $l_{OT} = 1380 \mu\text{m}$ , and  $d_{OT}$  ranging from  $93 \mu\text{m}$  to  $131 \mu\text{m}$  (Right). c) 4D printed SMP KF (Left) and OT (Right) samples with corresponding volume fractions of 4%, 5%, and 7%. The scale bar represents 2 mm. Detailed geometrical configurations for all structures can be found in Table S2 of Supplementary Material. d) Shape memory effect of SMP architected materials. Shape programming happens as a result of heating, followed by deformation and cooling. Shape recovery to its original shape occurs upon heating. The scale bar is 1 cm. .... 53

**Figure 4-2** a) We characterize the thermal properties of SMP microlattices and the contribution of both conduction and radiation heat transfer modes using the IR thermography methodology. In response to the low intrinsic thermal conductivity of SMP ( $0.2\text{-}0.3\text{ Wm}^{-1}\text{K}^{-1}$ ), high IR emissivity (0.94), and high porosity (>93%) of these architected materials, radiation contribution is significant in SMP microlattices. b) The primary heat transfer modes—conduction and radiation— in OT and KF SMP microlattices. Tunability of geometry configuration in SMP microlattices results in the programmability of their thermal properties. Therefore, we use mechanical compression for reconfiguring their geometry and monitor their thermal conductance as a function of mechanical strain. c) IR images of the KF (Left) and OT (Right) samples. The IR images contain information on the temperature gradient of each unit cell for calculating the thermal properties of SMP microlattices. .... 54

**Figure 4-3** a)  $\text{Tan}\delta$  of 3D printed SMP. b) Measured storage modulus of the bulk SMP using dynamic mechanical analysis (DMA) and the derived volume fraction of the frozen bonds as a function of temperature on the secondary axis. c) Measured thermal conductivity of bulk SMP and the applied Maxwell effective medium theory model for explaining the transition behavior in the thermal conductivity of the bulk SMP material..... 56

**Figure 4-4** Lattice structure model applied for radiative conductivity and notations a) Octet truss and b) Kelvin foam lattice. The heat flow is parallel to the z-direction..... 59

**Figure 4-5** a) Measured thermal conductivity of OT samples, and b) KF samples with 4%-7% volume fraction ratios. The dotted and solid lines represent the analytical predictions for the conduction contribution and radiation contribution, respectively. The increase in the conduction contribution is attributed to the changes in the intrinsic thermal conductivity of bulk SMP as a function of temperature. The increase in the radiation contribution results

from increasing the temperature in both samples following the Stefan-Boltzmann law. c) Contour plot of the effective thermal conductivity as a function of volume fraction and temperature for c) OT and d) KF samples. The dashed lines represent the constant thermal conductivity values, while the shaded regions are all thermal conductivity values in-between the dashed lines. By increasing the volume fraction, the radiation contribution in both samples decreases to reach the value of zero when the effective thermal conductivity converges to the intrinsic thermal conductivity of bulk SMP at the volume fraction of 1. ... 63

**Figure 4-6** a) By heating the SMP microlattices above their glass transition and applying an external compression, their thermal conductance can be tuned and retain the programmed value even after removing the compression at below glass transition temperatures. As a result of heating the microlattices above their glass transition, they recover to their initial configuration; therefore, their thermal conductance restores. Programmable thermal conductance in the b) OT and c) KF samples with an initial 5% volume fraction up to 36% strain. The IR images correspond to each strain cycle for deriving the conductance information. d) The measured conductance values for the OT sample illustrate that by increasing the volume fraction and strut densification, the effective thermal conductance increases by compression. Therefore, increasing the thermal conductance of OT lattices is attributed to conduction contribution. e) The measured conductance values for the KF sample demonstrate no strut densification while decreasing the view factors (i.e., radiation contribution) causes the decreasing trend in the effective thermal conductance. Therefore, decreasing the thermal conductance of KF lattices is attributed to radiation contribution. 65

**Figure 4-7** Impact of volume fraction increase vs. strut densification effect to the sharp rise of conduction contribution in thermal conductance of the OT sample with 5% initial volume fraction..... 67

**Figure 4-8** Close-up images of the compressed OT lattice with 0.05 volume fraction at a) 14%, b) 24%, and c) 36% strain. The strut borders of the beams viewing the camera have been highlighted in white, and the contact points resulting from densification have been shown in red—the local strut densification results in a decrease in thermal transport length from one junction to another. .... 68

**Figure 4-9** Mechanical deformations of a single kelvin foam unit cell at a) 0% strain and b)36% strain. The color bar demonstrates the amount of deformation in mm..... 70

**Figure 4-10** Analytical calculation of thermal conductance in a compressed KF unit cell up to 36% strain. The conduction contribution increases due to increasing the volume fraction, while the radiation contribution decreases due to a reduced accumulative contribution from the strut view factors..... 71

**Figure 5-1** Thermal conductivity contour exploring diffuse to ballistic phonon transport regimes as the strut thickness and the pitch scale, respectively. Each line accounts for a constant thermal conductivity of carbon lattice structures (right). The contour model assumes the size effect in phonon transport by diffuse boundary scattering..... 79

**Figure 5-2** Effective thermal conductivity of glassy carbon nanolattices by incorporating the porosity provided by the architecture of the unit cells..... 79

**Figure 5-3** Electrical resistance thermometry technique for thermal conductivity, electrical conductivity, and heat capacity measurement of nanowires and nanolattices..... 81

**Figure 5-4** a) DC and AC electrical resistance measurement at room temperature. The linear fit on the I-V curve carries information about the resistance of the wire. b) The electrical resistance has been derived using the slope of the DC linear fit to the ohmic region of the I-V curve at each average temperature. .... 83

**Figure 5-5** Electrical conductivity of the wires as a function of global heating of the chamber. The electrical conductivity increases as a result of thermally activated electrons. The dashed line represents the modeling for the thermally activated electrons..... 84

**Figure 5-6:** a) Swiping the third harmonic of the voltage from 10 to 1000 Hz. The values below 50 Hz are frequency-independent; therefore, we can calculate the thermal conductivity using Equation 5. The dependency of the third harmonic of the voltage on frequency contains information on the thermal conductivity and heat capacity of the glassy carbon wires. b) The thermal conductivity of glassy carbon nanowires increases as a function of temperature as an intrinsic behavior of amorphous materials. .... 85

**Figure 5-7:** a) Third harmonic of the voltage as a function of frequency at temperatures between 300 K to 645 K. The third harmonic of the voltage contains information about the thermal conductivity of the glassy carbon wire below 50 Hz and carries information on the heat capacity plus thermal conductivity in frequency ranges above 50 Hz b) The calculated volumetric heat capacity as a function of temperature. The dashed line represents the modeling of the volumetric heat capacity of phonons for glassy carbon nanowires. .... 87

**Figure 6-1:** LCE-based architected materials can create a thermal connection in struts made out of LCE upon heating without any external stimuli. The structure would reverse to its original shape upon cooling. The reversible thermal contact created due to exposure to heat can be realized to define a new class of thermal switches..... 93



**Figure 6-2:** Thermal conductivity of LCE architected metamaterial before (Left) and after the (Right) transition. The effective thermal conductivity increases at first with the increase of volume fraction due to rising trends in conduction and radiation contributions and then decreases with the sharp reduction in the radiation contribution. .... 95

**Figure 6-3:** Reconfiguring LCE struts reduces the view factor between most struts after transition, as shown in the table. .... 95

**Figure 6-4:** The switching ratio of the LCE architected metamaterial as a function of volume fraction. The conduction switching ratio increases with the volume fraction; however, the radiation switching ratio first decreases then increases due to the ratio of radiative thermal conductivity trends demonstrated in Figure 6-3. The analysis is done for different surface emissivity values to identify the role of radiation. Activation of the radiation heat transfer mode deteriorates the performance of the LCE thermal switch. .... 96

**Figure 6-5:** The FEM results demonstrate the temperature distribution in the architected thermal switch at different volume fractions. The plot presents the switching ratio as a function of volume fraction with different intrinsic thermal conductivities of LCE when the thermal conductivity of the structural polymer is fixed at  $0.1 \text{ Wm}^{-1}\text{K}^{-1}$ . The switching ratio increases with the increase of volume fraction since conduction becomes the dominant mode of heat transfer. The increase of LCE thermal conductivity results in a larger switching ratio of the effective thermal conductivity values, .... 97

**Figure 6-6:** a) Experimental setup with heating and sensing membranes to measure thermal conductance in reverse and forward directions. b) Ray-tracing simulation setup for the asymmetric nano strut as a building block of nanolattices. The left end diameter is fixed at

1 $\mu$ m, but the right side diameter changes from 1  $\mu$ m to 10 nm. The boundaries are assumed to be diffuse..... 99

**Figure 6-7:** Preliminary ray-tracing simulation results for the asymmetric nano strut demonstrated in **Figure 6-6 (b)**. The simulation considers the full detail of the geometry for ballistic phonon transport. Phonons were injected in both directions, and the rectification was calculated based on the difference between forward and reverse heat flux values over the forward heat flux value. The top and bottom surface boundaries are assumed to be periodic..... 100

**Figure 6-8:** The asymmetric nanolattice design for realizing a potential thermal rectification. The gradient in the diameter of the struts creates an asymmetric geometry..... 101

**Figure A-0-1:** a) Configuration factor between an inclined cylinder and planes of void surfaces b) between adjacent tilted cylinders..... 119

**Figure A-0-2:** Schematic of adjacent equal bars located at an angle of  $\alpha$  towards each other. .... 121

## LIST OF TABLES

<b>Table 2-1:</b> Comparison between the normalized thermal resistance ( $R_{structure}/R_{initial}$ ) of the optimized topology structures and the reference structure of the studied heat guides shown in <b>Figure 2-2</b> .....	27
<b>Table 3-1:</b> Feature parameters in addition to the surface finish of the samples used for experiments. Truss angle ( $\theta$ ), length ( $l$ ), wall thickness ( $t$ ), and bar diameter ( $D$ ) were measured using SEM with an accuracy of $\pm 2^\circ$ , $\pm 3\%$ , $\pm 10\%$ , $\pm 15\%$ respectively. The volume fraction ( $v$ ) has been calculated based on the CAD model of each unit cell.....	37
<b>Table 4-1</b> Designed and measured dimensional parameters of the 3D printed microlattices .....	52
<b>Table 4-2</b> Volume fraction and conduction contribution correlations utilized for the OT and KF lattice structures.....	57
<b>Table 4-3</b> Change in the volume fraction ( $v$ ) and strut densification contributions in transferring the heat through conduction at different strains. The reducing value of $L_2$ as a function of strain indicates the decrease in the thermal resistance or the increase in thermal conductance due to strut densification. ....	69
<b>Table 4-4</b> Mechanical deformations of a single kelvin foam unit cell at a) 0% strain and b)36% strain. The color bar demonstrates the amount of deformation in mm.....	70

## ACKNOWLEDGMENTS

I would like to express my deepest appreciation to my committee members, Professor Lorenzo Valdevit, Professor Ramin Bostanabad, and Professor Jaeho lee, for their support during the course of my Ph.D. program. I'm extremely grateful to Dr. Valdevit for all his support and guidance during the completion of this thesis. I want to extend my sincere thanks to Dr. Phong Luong, Professor Marc Madou, Professor Roger Rangel, and Professor Faryar Jabbari for their guidance and endorsement during the final months of my Ph.D. program.

I'm grateful to my former and fellow labmates Dr. Laia Ferrer Argemi, Dr. Ziqi Yu, Dr. Zongqing Ren, Jonathan Sullivan, and Xiao Nie for transferring their skills, stimulating discussions, all the fun we had, and creating a safe space far from home. I have been fortunate to call all these people my friends.

I would also like to thank Dr. Tobias Schaedler from HRL laboratories for the collaboration opportunity on the hollow nickel lattice project and Professor Howon Lee from Seoul National University for our collaborative work and all his constructive feedbacks on the SMP project. Many thanks to Professor Valdevit's lab members, especially Dr. Jens Bauer, for trusting me with the carbon nanowires and the opportunity to learn more about nanoscale additive manufacturing. Special thanks to Dr. Jae Choon Kim from Samsung Electronics for sharing his immense knowledge on electronic packaging and all the good memories in the term of our collaboration. I would like to thank the IDMI facility at UCI, especially Benjamin Dolan, for his support and training for metal additive manufacturing.

Last but not least, I'm greatly indebted to my parents and my sister for believing in me, lifting me up, and providing their moral support whenever I needed it the most. Completing this chapter of my life would not have been possible without the support and nurturing of my partner, Mohammad Hossein. They remind me every day how being tough is always a choice when I am being challenged.



# CURRICULUM VITAE

## Education

---

### University of California, Irvine

Ph.D. in Mechanical and Aerospace Engineering (2016-2021)

### University of California, Irvine

M.S. in Mechanical and Aerospace Engineering (2016-2018)

### University of Tehran, Tehran, Iran

B.S. in Mechanical Engineering (2011-2015)

## Research Projects

---

### Programmable Thermal Transport in 4D printed Architected Materials

*Collaboration with Howon Lee's group at Rutgers University (Feb. 2020- Sep. 2021)*

- Characterized thermal properties of bulk shape memory polymers and modeled the glass transition impact on thermal conductivity
- Characterized the switching behavior in thermal conductance of shape memory polymer microlattices as a function of compression using IR thermography
- Designed architected LCE-based thermal switch structures

### Architected Materials for Electronic Packaging

*SAMSUNG (Jun. 2019 – Jun. 2021)*

- Designed optimized metallic structures using topology optimization for minimizing the thermal cross-talk in 2.5D packaging structures
- Fabricated optimized metallic structures using SLM additive manufacturing technique
- Characterized the thermal resistance of optimized metallic structures using IR thermography

### Phase Change Dynamics and 2-dimensional 4-bit Memory in $\text{Ge}_2\text{Sb}_2\text{Te}_5$

*SRC GRC Task (May 2019 - Aug. 2019)*

- Performed Optothermal simulations using the crystallization dynamics to predict the temporal evolution and resultant reflectivity of GST phases

### Thermo-Mechanical Characterization of Nano-scale Architected Materials

*NSF CMMI (Mar. 2019 – Apr. 2021)*

- Performed thermal conductivity measurement of highly strained pyrolytic glassy carbon nanowires using  $3\omega$  electrical resistance thermometry (In collaboration with Lorenzo Valdevit’s Group at UCI)

**Thermal Transport in Hollow Nickel Microlattices**

*NASA ESI Program (May 2018 - Mar. 2019)*

- Developed IR thermography setup for thermal conductivity measurement of mesoscale cellular materials
- Characterized conduction and radiation contributions in ultralight hollow nickel microlattices as a function of temperature and compression

**Micro Thermal Stage Design Optimization**

*Bodle Technologies (Feb. 2018- Aug. 2018)*

- Designed and optimized the heating stage for phase change material display applications

**Plasmo-thermomechanical Radiation Detector with On-chip Optical Readout**

*Collaboration with Boyraz group at UCI (Nov. 2017- Feb. 2018)*

- Performed Optothermal simulations to predict the thermal response of IR detector fishbone antennas

**Publications**

---

**Journal papers** .....

- (1) **Farzinazar, S.**; Wang, Y.; Yang, C.; Owens, C.A.; Lee, H.; Lee, J.; Programmable Thermal Transport in 4D Printed Architected Materials, (Under preparation)
- (2) **Farzinazar, S.**; Ren, Z.; Lim, J.; Kim, J.C.; Lee, J.; Thermomechanical Topology Optimization of 3D Heat Guiding Structures for Electronic Packaging, JEP, (Accepted)
- (3) Sevison, G.A.; **Farzinazar, S.**; Burrow, J.A.; Perez, C.; Kwon H.; Lee, J.; Asheghi, M.; Goodson, K.E.; Saragan, A.; Hendrickson, J.; Agha, I.; Phase change dynamics and 2-dimensional 4-bit memory in Ge<sub>2</sub>Sb<sub>2</sub>Te<sub>5</sub> via telecom-band encoding, ACS Photonics 7, 480–487, 2020
- (4) **Farzinazar, S.**; Schaedler, T.A.; Valdevit, L.; Lee, J.; Thermal Transport in Hollow Metallic Microlattices, APL Materials 7, no. 10, 2019
- (5) Zhao, Q.; Khan, M.W.; **Farzinazar, S.**; Lee, J.; Boyraz, O.; Plasmo-thermomechanical Radiation Detector With On-chip Optical Readout, Optics Express 26, no. 23, 2018

**Conference papers** .....

- (6) **Farzinazar, S.**; Lee, J.; Thermal Conductivity Measurement of Mesoscale Lattices Using Steady-State Infrared Thermography, IEEE ITherm, Las Vegas, NV, May 2019.

(7) **Farzinazar, S.**; Ren, Z., Lee, J.; Thermal Conductivity of Graphite Microlattices, IEEE ITherm, San Diego, CA, May 2018.



# **ABSTRACT OF THE DISSERTATION**

Thermal Transport in Additively Manufactured Metamaterials

by

Shiva Farzinazar

Doctor of Philosophy in Mechanical and Aerospace Engineering

University of California, Irvine, 2021

Professor Lorenzo Valdevit, Chair

Fundamental thermal management problems, from macroscopic issues such as global warming to microscale problems such as electronic cooling, demonstrate the need for unconventional tools to manipulate heat flow across a wide range of length scales. The ability to fabricate materials that exhibit highly anisotropic thermal properties, ideally tunable under service conditions, would be game-changing in several applications. Metamaterials, i.e., porous solids consisting of periodic repetitions in three dimensions of carefully designed unit cells, could provide an avenue towards these goals. This doctoral thesis investigates thermal transport mechanisms in complex additively manufactured metamaterials, enabling a new strategy for manipulating heat flow and leading to programmable thermal behavior.

A common challenge of conventional cooling solutions in electronic packaging is thermal cross-talk and the formation of local hotspots due to uniform heat dissipation from the heat source to the heat sink. Thermal metamaterials can address these challenges by providing an optimized solution for non-uniform heat dissipation. A suitable approach for the design of metamaterials enabling ideal heat routing while maintaining mechanical stability is topology optimization. A density-based topology optimization method is presented to identify thermally conductive and mechanically stable structures for optimal heat guiding under various heat source-sink arrangements. As a proof-of-concept experiment, we fabricate thermo-mechanically optimized 3D heat guiding structures using Laser Powder Bed Fusion (LPBF) technique and develop an infrared (IR) thermography methodology to characterize their thermal properties. Our results reveal that the thermal resistance of the

topology optimized structures outperforms that of reference structures at the same volume. This approach enables new avenues for optimal heat guiding, thus advancing state-of-the-art thermal management in electronics.

Periodic metamaterials (e.g., microlattices) provide another design framework to generate mechanically stable thermal metamaterials for preferential heat routing, whereby the effective thermal properties are determined by the interplay of metamaterials topology and constituent material properties. This thesis investigates heat transfer mechanisms in architected metamaterials by exploring the role of architecture on the conduction and radiation contributions. We model and characterize extremely low-density metallic hollow microlattices and polymeric shape memory lattices, both of which enable recoverable deformations in excess of 50% when compressed. An analytical model previously proposed for highly porous foams is adapted to regular lattice topologies, allowing expressions for conduction as a function of volume fraction, geometrical factor, constituent material properties, and radiation as a function of volume fraction, surface emissivity, view factor of the struts, and absolute temperature. Through IR thermography, we experimentally identify the individual contribution of each heat transfer mode. In particular, the impact of high surface emissivity and high surface-to-volume ratio on the resultant radiation contribution are explored. In contrast with monolithic solid materials, we find that radiation has a more significant contribution to heat transfer, even at low absolute temperatures.

We experimentally demonstrate the possibility of modulating the thermal properties of architected metamaterials by geometrical reconfiguration using an external mechanical stimulus. We show that large-scale compression of stretching-dominated lattice topologies, characterized by deformation behavior involving buckling and densification, increases contact among micro-struts, thus increasing conductive thermal transport. In contrast, deformation in bending-dominated lattice topologies leads to a change in view factor among micro-struts without altering the physical contacts, thus decreasing radiative thermal transport. These findings suggest that thermal transport in mechanically recoverable architected materials can be programmed upon external stimuli, a viable strategy for designing future dynamic or adaptive thermal control devices and thermal information processing systems.

In closing, we explore the possibility of generating superior thermal metamaterials by architecting solids at the nanoscale, thus allowing the exploitation of size effects on the thermal conduction mechanism.

# CHAPTER 1

## INTRODUCTION

### 1.1. Motivation

Although material requirements are well understood for simple objectives like improving insulation for thermal management of a system, guiding heat flux in complex scenarios is a remaining challenge. The slow progress made in heat transfer control can be attributed to the parallel existence of conjugated modes of heat transfer and the lack of novel 3D structures to control the heat transfer at will. Thermal metamaterials are porous solids consisting of periodic repetitions in three dimensions of carefully designed unit cells that can transfer heat beyond the capacity of existing monolithic materials. The idea of thermal metamaterials has altered the design of thermal regulating devices with the possibility of manipulating the heat flow arbitrarily [1]. The design of exotic metamaterials has provided unprecedented thermal [2]–[5], mechanical [6]–[8], optical [9]–[10], and acoustic [11] properties, with application in multiple technological fields. New approaches with improved efficiency, accuracy,

adaptiveness, tunability, and compactness are emerging to solve traditional thermal management problems.

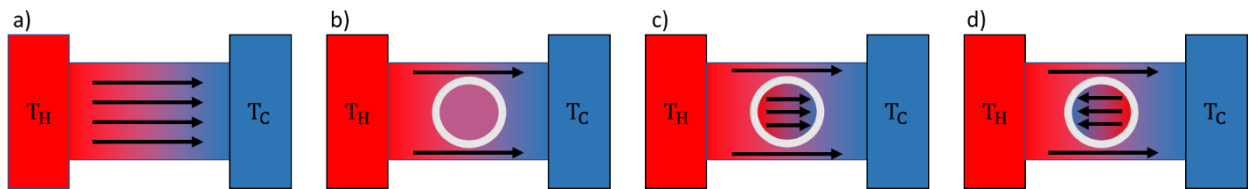
Controlling heat is particularly important to address world-class problems across many orders of magnitude in length scale, such as global warming or energy crisis on the macroscale and overheating electronic devices on the microscale [12]. Thermal metamaterials can control the heat flow through conduction, convection, and radiation modes with novel approaches. However, in this case, the geometrical parameters of the metamaterial structures can play a more dominant role than the physical properties of their constituting material [13]. Therefore, further investigation is required for exploring the geometrical impacts on controlling the heat flux while identifying the contributions from individual heat transfer modes.

Herein, we explore the impact of geometry on controlling the heat flux through architected thermal metamaterials. First, we study the thermo-mechanical topology optimization approach for introducing structures with optimal heat routing to address the thermal management challenges in electronic packaging. Subsequently, we investigate the role of topology in the thermal properties of lattice-based architected materials and introduce a new mechanism for the programmability of heat transfer. Finally, we develop analytical solutions to identify the contributions from different heat transfer modes and experimentally investigate tunable thermal properties in architected thermal metamaterials.

## **1.2. Background on Thermal Metamaterials**

When a block of monolithic material is placed between a heat source and a heat sink, the heat flows from a higher to a lower temperature domain by establishing a uniform

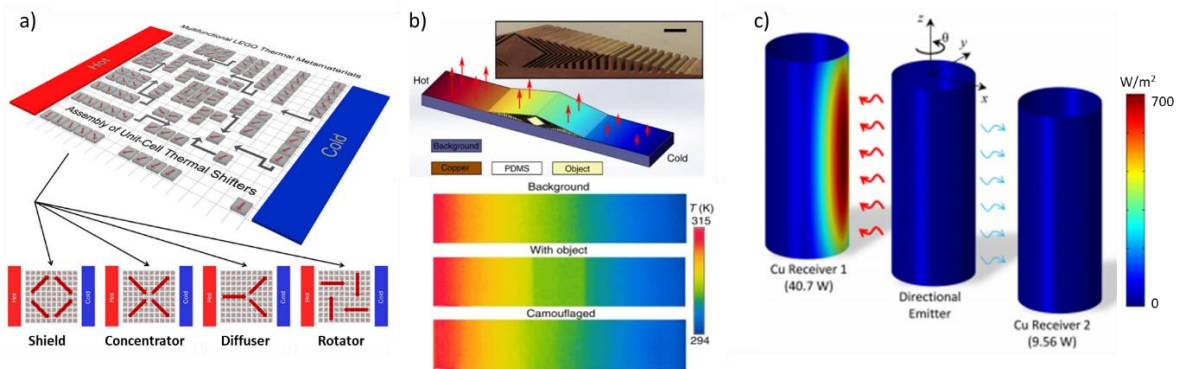
temperature gradient across the material (**Figure 1-1 (a)**). However, by applying thermal metamaterials, this uniform temperature distribution can be disturbed, and the desired routing of the heat flux can be achieved, as demonstrated in **Figure 1-1 (b-d)**. Most research studies on thermal metamaterials have focused on how transformation thermodynamics could be utilized to design functional structures [14][15]. As a result, thermal metamaterial designs based on the conduction heat transfer mode have been demonstrated through numerical [16][17] and experimental [18]–[20] efforts.



**Figure 1-1:** a) Demonstration of the heat flux when a block of material is placed between a heat source and a heat sink. Heat flux manipulation by b) thermal shielding, c) thermal concentration, and d) thermal inversion concepts.

The past decade has witnessed significant advancements towards practical demonstration of energy-free thermostats [21], thermal camouflage [22], active thermal cloaking devices [23], and tunable multifunctional thermal metamaterials [4] (**Figure 1-2 (a)**). Similar to thermal conduction, manipulation of heat flux through the radiation heat transfer is also well-established. While nanophotonic structures can be implemented to engineer the spectral and spatial characteristics of thermal radiation [24]–[28], surface coatings are still great candidates for changing the radiative properties of flat surfaces [29]. Recently, structured thermal surfaces were explored for concealing the thermal radiation signal of an object [30]. This radiative thermal camouflage is designed to be reliable for scenarios where the background does not have a uniform temperature profile ( **Figure 1-2(b)**). With heat flow phenomena arising from heat transfer by radiation plus conduction,

optimum designs are strongly preferred for simultaneous manipulation of heat flux through both modes of heat transfer. Dede *et al.* [31] investigated thermal composite metamaterials with co-optimized anisotropic thermal conductivity and external surface emissivity for combined radiative and conductive control of heat flow ( **Figure 1-2(c)**). While these composite metamaterials highlight opportunities to customize radiative intensity patterns and control thermal energy transfer for complex multi-body scenes, they do not address the manufacturing challenges nor exhibit any experimental demonstration of the concept. Additionally, with effective properties of thermal metamaterials primarily depending on their topology rather than their composition, designing an optimized structure with a single constituent material is of great interest. These requirements necessitate advanced manufacturing techniques in addition to the novel design of thermal metamaterials that can manipulate the heat flow in complex 3D thermal management problems.



**Figure 1-2** a) Schematic of tunable multifunctional thermal metamaterials. The designed assemblies of thermal metamaterials as unit cells enable the manipulation of local heat flux for multiple functions such as thermal shifter, concentrator, diffuser, and rotator[4]. b) Schematic and fabricated device of the radiative thermal camouflage. Experimentally measured temperature profiles with an IR camera are demonstrated for a pure background, a background with an object on the surface, and an object on the surface camouflaged by the structured thermal surface. c) Co-optimized conduction and radiation-based thermal metamaterials for

selective control of the heat flow through the enhanced design of both the anisotropic thermal conductivity of the emitter body and its surface emissivity.

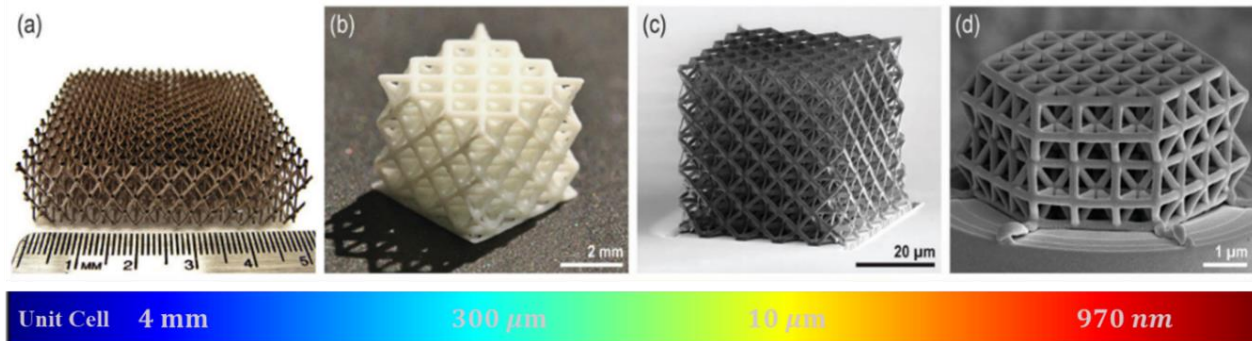
### **1.3. Role of Additive Manufacturing**

Advances in material processing and availability have revolutionized the development of humankind since the stone age. The key driving force for developing the metamaterials discussed above has been the emergence of additive manufacturing techniques. Additive manufacturing allows customized structures from metals, ceramics, and polymers, without the need for molds or machining techniques required for the conventional formative and subtractive fabrication approaches. Innovation of processes like selective laser melting (SLM), stereolithography (SLA), selective laser sintering (SLS), and electron beam melting (EBM) has resulted in the creation of structures with submillimeter feature size resolution. Although these methods provide increased design freedom, they are very limited in the rate of production [6]. The evolution of high-resolution additive manufacturing techniques such as self-propagating photopolymer waveguide (SPPW) [32], projection micro-stereolithography (P $\mu$ SL) [33], and direct laser writing (DLW) [34][35] have led to the production of progressively smaller lattice structures (a classic metamaterial topology) (**Figure 1-3**) with unit cell sizes below 1 $\mu$ m. However, fabrication techniques required for creating nanolattices are confined to polymer-based materials, additive manufacturing, self assembly-based processes, and low throughput regardless of their high resolution.

Besides their advantages, all additive manufacturing techniques have technical challenges associated with implementation. A couple of their significant challenges are the limited palette of materials available for fabrication and not introducing macroscopic flaws that neutralize the favorable properties gained from nanomaterials. However, despite the



limitations, additive manufacturing continues to exhibit great potential for applications in aerospace, biomedical, automotive, and energy field to create complex geometries with advanced material properties.



**Figure 1-3** Lattice miniaturization from mm to nm scale from reference [6]. a) Hollow nickel microlattices manufactured by SPPW polymer templates in conjunction with electroless nickel plating and removing the polymeric template [36]. b) Solid beam alumina lattice structure manufactured by P $\mu$ SL made of a hybrid of solid PEGDA and alumina nanoparticles followed by a sintering process[7]. c) Hollow-beam alumina lattice manufactured by two-photon DLW, alumina atomic layer deposition, and oxygen plasma etching of the internal polymer template [37]. d) Solid-beam glassy carbon lattice manufactured by two-photon DLW and subsequent pyrolysis at 900°C.

#### 1.4. Heat Transfer Mechanisms in Thermal Metamaterials

The diffusive nature of heat flux in the macroscale relies on controlling the thermal transport energy through the material for heat flux manipulation purposes [18]. Most research studies at the macroscale have focused on promoting heat transfer through a high thermal conductivity medium or suppressing the heat flow via an insulating material. Therefore, engineering the thermal conductivity is crucial to manipulating the heat flow. Porous materials (lattices) consisting of periodic repetitions of architected cells [38] are brilliant solutions for controlling the heat flux. Inspired by their lightweight and excellent mechanical properties, natural cellular materials such as bone, cork, and wood led to the creation of architected materials as early as 1970. One of their first applications is hexagonal

honeycombs as the sandwich cores in the aviation industry [39]. To exploit the multifunctional properties of architected materials in the microscale, the capability of predicting their effective properties is of utmost importance. Here we separately experimentally identify the contribution from each mode of heat transfer in the effective thermal properties of mesoscale architected materials.

One of the main concepts that allow estimates of the effective thermal conductivity of architected materials is the analogy between electrical and thermal conductivity [40]. However, the thermal resistance circuit only delivers upper and lower bounds and does not capture the detailed effect of the specific material architecture [41]. A summary of standard mathematical and empirical correlations based on the thermal resistance analogy for estimating the effective thermal conductivity can be found in references [42]–[45]. These effective medium theory approaches treat the architected material as a matrix of constituent material with pores made of air as secondary material. However, the effective medium theory approaches can lose their prediction accuracy with a complex 3D orientation of the pores in the architected materials. At the continuum level, in addition to the intrinsic thermal properties of the constituent material and their quantified contribution through volume fraction, the topology of the pores (i.e., size, shape, shape, connectivity, and orientation of the pores) have a fundamental role in the effective thermal properties of architected materials [38][46]. Therefore, the conduction contribution can be derived as below:

$$\kappa_{cond} = A \cdot \bar{\rho} \cdot \kappa_{solid} \quad \mathbf{(1-1)}$$

where  $\bar{\rho}$  is the volume fraction of the structure,  $\kappa_{solid}$  is the thermal conductivity of the constituent solid, and  $A$  is the geometrical factor that accounts for the tortuous shape of the ligaments in the architected material.

On the other hand, phonon transport and phonon scattering are majorly responsible for heat transfer at the micro and nanoscale. Phonons can exhibit both wave-like and particle-like behavior in thermal transport phenomena. Earlier studies on the thermal conductivity of silicon materials and nanostructures have substantially contributed to addressing phonon transport at the micro/nanoscale [47][48]. By treating phonons as incoherent particles, classical theories such as Boltzmann Transport Equation (BTE) have accurately captured the size dependent thermal conductivity of silicon thin films [49] and high purity nanowires [50][51]. Under the standard isotropic approximations, the BTE particle model can be described as [52]:

$$\kappa_{cond} = \frac{1}{3} \int C v \Lambda d\omega \quad \mathbf{(1-2)}$$

where  $\omega$  is the phonon frequency,  $C$  is the volumetric heat capacity,  $v$  is the phonon velocity, and  $\Lambda$  is the phonon mean free path. The nanoscale geometric features of metamaterials can increase the boundary scattering of phonons and reduce the thermal conductivity due to a decrease in the mean free path [53]. The combination of high porosity and classical size effects can lead to ultralow thermal conductivity in sophisticated nanoarchitected materials[54], which is not attainable even by the existing lightest monolithic silica aerogels [55].

In the absence of forced convection (i.e., active cooling), the only mechanism that must be considered is natural convection. While it is a fair approximation to ignore the contribution from natural convection in metallic architected materials, it is expected to play a significant

role in the architected structures with ceramic or polymer constituent materials. However, if the cell sizes are small enough ( $<10$  mm), the impact of natural convection within the cells is negligible, even in the case of ceramic/polymeric architected materials [56].

Aside from conduction and convection heat transfer modes, radiation plays a dominant role in the heat transfer of architected materials. While the contribution on this mode of heat transfer has been majorly highlighted in the high-temperature applications [57][58], Kaviany [59] demonstrated how radiation heat transfer is significant in low-temperature insulation applications as well as in high-temperature combustion applications for porous mediums. However, there are substantial difficulties in predicting radiative heat transfer in architected materials due to the complexity of the geometry and inherent complications associated with the transport mechanism. Different methods of addressing radiative heat transfer in high porous mediums have been explored in the literature. Some theories model the porous material as a dispersion of opaque particles of given shapes and utilize the Mie theory or the geometric optic laws [60][61]. Glicksman *et al.* [62] demonstrated radiative heat transfer in cellular foams by modeling their structure as random arrangements of opaque struts with constant thickness to create regular dodecahedron cells. Kuhn *et al.* [63] utilized infinitely long cylinders to model the struts and employed the Mie scattering theorem to calculate the radiative characteristics. Later, Doermann and Sacadura [60] proposed a model that improved the previous ones by considering particle modeling, obtained from the microscopic analysis of carbon open-cell foams, and was a more accurate representation of the actual geometry. A decade later, Kaemmerlen *et al.* [64] utilized polystyrene bulk medium's morphological data and optical properties to model radiative heat transfer in extruded foams (XPS). The radiative properties of these XPS foams were defined by considering the

contributions of each wall and strut using the independent scattering hypothesis. Other researchers employed inverse methods based on direct measurements of the optical properties [65][66]. Another approach for addressing the role of radiation heat transfer is through ray tracing Monte Carlo simulations at the local scale [67]. Petrasch *et al.* [68] explored the radiation heat transfer in reticulated porous ceramics using Monte Carlo simulations by reconstructing the foam microstructure through X-ray tomography. However, previous analytical approaches underestimate the radiation contribution due to the inaccuracy of the geometry estimation, and Monte Carlo simulations require a substantial computational effort and should only be restricted to the study of the detailed effect of the architecture. Therefore, a more reliable analytical approach is necessary to realize an accurate representation of the geometry of the architected materials to calculate the role of radiation contribution.

### **1.5. Experimental Validation of Thermal Metamaterials**

Experimental measurements of thermal properties in metamaterials are challenging due to their complex geometries and interconnected heat transfer mechanisms, in addition to the inherent limitations of standard thermal characterization techniques. State-of-the-art measurement techniques of thermal conductivity can be categorized into two main groups: steady-state and transient methods. Thermal conductivity measurement under steady-state conditions is based on the characterization of heat flux and temperature gradient across the sample, while transient methods are generally used to measure thermal diffusivity by recording the temperature as a function of time. The main steady-state techniques include the guarded hot plate method, heat flow meter, axial heat flow method, and pipe method. The

guarded hot plate method [69] is generally used for characterizing materials with low thermal conductivity ( $<0.8 \text{ Wm}^{-1}\text{K}^{-1}$ ) by applying a temperature gradient with a known heat flux value across the sample. The temperature measurement is performed when the sample reaches the steady-state condition, and the thermal conductivity can be calculated using the heat flux value, sample thickness, surface areas, and the temperature gradient [70]. The design of the heat flow meter technique is very similar to the guarded hot plate method, with a difference in utilizing the heat flux sensor instead of the heater [71]. In addition, the most widely used method for low-temperature thermal conductivity measurement is the axial heat flow technique at which a temperature gradient is created by locating the sample between two reference samples of known thermal conductivity to form a column with a heater and a heat sink at the two ends [71]. This method is helpful for the thermal characterization of samples with thermal conductivity values ranging from 0.2 to  $\sim 200 \text{ Wm}^{-1}\text{K}^{-1}$  [72]. The last technique in the category of steady-state thermal conductivity measurement methods is the pipe method, also referred to as the radial heat flow method. In this technique, a core heater is placed at the central axis of the sample, and a heat sink is placed outside the sample's surroundings [73]. For minimizing the heat loss to the top and bottom of the sample, a large length to radius aspect ratio is employed for sample preparation. This method is utilized for measuring the thermal conductivity of metals, high conductivity inorganics, and polymer composites with values ranging from 0.02-200  $\text{Wm}^{-1}\text{K}^{-1}$  [70]. However, in-contact temperature sensors such as thermocouples are employed to measure the temperature gradient in all these steady-state techniques, which adds to the measurement uncertainties due to their inherent thermal contact resistance.

The transient thermal conductivity measurement category consists of the hot wire, plane source, and laser flash methods. The hot wire method, which is a modification of the steady-state pipe method, applies a hot wire embedded in the test sample that acts as a heater and a temperature sensor [74][75]. The fundamental principles of this method are close to the plane source method, but a thin spiral pattern of the heater is placed in between two test samples for heating and sensing purposes in the plane source technique [76][77]. The laser flash method [78] is the most frequently used technique for measuring the thermal conductivity of solid materials due to its wide temperature (373-3273 K) and thermal conductivity ( $>0.01 \text{ Wm}^{-1}\text{K}^{-1}$ ) ranges [70]. In this method, a small disk of the test sample is heated by the laser pulse, and temperature changes are monitored using an infrared detector. Although the infrared detector eliminates the uncertainties of the previous in-contact thermometry methods, employing complex architected structures and decoupling the contribution from different heat transfer modes are remaining challenges in the existing thermal characterization techniques. Therefore, there is a specific requirement for developing a thermal characterization technique compatible with complex 3D architected materials, employs a non-contact thermometry technique for eliminating the contact resistance error, and identifies the contributions from each heat transfer mode.

## **1.6. Outline of Doctoral Research**

This thesis develops and extends the understanding of heat transfer mechanisms in architected metamaterials using theoretical modeling and experimental approaches. Chapter 2 dives into creating optimized additively manufactured architectures for thermal management in electronic packaging applications. We create a numerical platform for

topology optimization of heat guiding structures and develop 3D structures with volume fraction constraints of the package by optimizing for thermal, mechanical, and thermomechanical objective functions. We use a state-of-the-art metal additive manufacturing technique, Laser Powder Bed Fusion (LPBF), to fabricate topologically optimized and reference structures with identical masses and encompassing volumes. We evaluate the thermal performance of both optimized and reference structures using IR thermography and identify the thermal impact of applying optimized lightweight metallic structures in electronic packaging. Chapter 3 investigates thermal transport in metallic microlattices with 99% porosity. We thoroughly investigate the effect of architecture on conduction and radiation heat transfer modes using analytical approaches and IR thermography. First, we investigate the effective thermal conductivity of these ultralight metallic microlattices as a function of temperature using samples with the same volume fraction but different surface emissivity values. Next, we identify the radiation contribution as a function of engineering strain and explore the placement of metallic microlattices in the material property space. Chapter 4 covers programmable thermal transport in shape memory polymer (SMP) microlattices. We examine the contribution of conduction versus radiation in these polymeric microlattices by implementing an IR thermography-based experimental setup. We develop an analytical model for capturing the role of architecture using the existing theoretical approaches for highly porous mediums. We leverage the shape recoverability to modulate the geometrical configurations as a result of compression. We explore the changes in thermal properties as a function of compression and explain different thermal conductance trends in two classic lattice designs: the stretching-dominated Octet truss and the bending-dominated Kelvin foam. Chapter 5 presents a preliminary study aimed at designing and



demonstrating nanolattice materials with unprecedented combinations of high strength and low thermal conductivity. In addition to the role of porosity, tuning the thermal conductivity is investigated using increased contributions of heat-carrier scattering events with boundaries and microscopic heterogeneities. Glassy carbon nanolattices are analyzed using theoretical approaches of the semi-classical Boltzmann Transport Equation (BTE). Glassy carbon struts are fabricated using two-photon polymerization Direct Laser Writing (2pp-DLW), followed by pyrolysis. Subsequently, the thermal properties of glassy carbon struts are measured using  $3\omega$  electrical resistance thermometry, and the impact of architecture is predicted using the existing theoretical models. Finally, Chapter 6 summarizes key findings, explores potential directions for future study, and provides an outlook for additively manufactured thermal metamaterials.

# CHAPTER 2

## Topology Optimized Metallic Metamaterials for Electronic Packaging Application

### 2.1. Introduction to 3D Heat Guiding Structures for Thermal Management in Electronics

Enhancing computing capabilities at the device and die levels while increasing electronics' speed, efficiency, and reliability makes thermal management ever more challenging. Conventional cooling solutions based on higher thermal conductivity materials or heat exchangers dissipate the heat from a source to a sink only in a unidirectional manner, and they cannot guide the heat flow when the heat source and heat sink are unaligned. Earlier studies on guiding the heat flux have investigated this concept via ballistic phonon transport in holey silicon [79], through silicon via integrated thermoelectric cooling [80], thermal cloaks [81][18][82], and copper-PDMS based thermal shifters [4]. However, the existing macroscale approaches for thermal management in electronic packaging still rely on creating thermally conductive channels from a heat source to the heat sink using the through-hole vias [83], creating a cavity in the printed circuit board, and using high thermal

conductivity inlays [84]. Compared to 2D packaging scenarios, investigations on thermal management strategies for 3D packages are still limited. For instance, standard methods for resolving the thermal challenges in 3D ICs include floor plan optimization, reducing heat sink thermal resistance, lowering the chip's power consumption, and applying thermal vias [85]. These conventional solutions are effective when a heat-generating component is aligned with a heat sink (**Figure 2-1 (a)**). However, with a limited routing space in a 3D package, alternative solutions may be required for the thermal routing of unaligned heat source and heat sink components(**Figure 2-1(b)**). Therefore, to achieve the desired thermal objectives, novel heat guiding structures are required to acquire optimal heat flow routing under non-uniform power distribution.

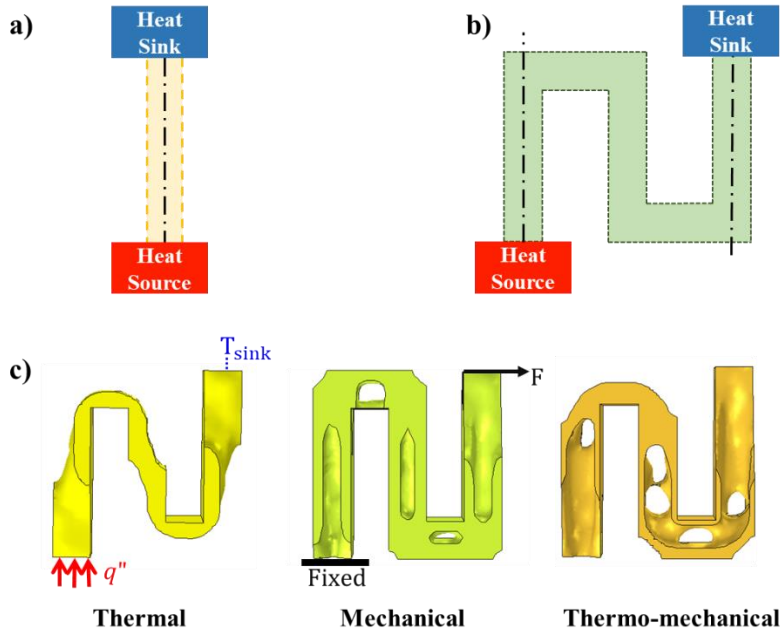
Capabilities of heat guiding structures to control the heat flux effectively [4][5][18][20][86] and to guide the heat in unaligned configurations of heat source and heat sink can lead to optimal solutions for complex packaging scenarios [2][3]. For example, 3D metamaterial solutions for heat guiding structures can potentially protect components with different temperature tolerances while effectively dissipating heat to address the demand for high integration density [87][88]. There have been fundamental studies on the possibility of developing thermal heat guiding structures and manipulating heat flows in 3D structures [82]. Dede *et al.* established optimized 3D heat routing structures for power electronics gate drive PCB thermal management [89]. While most of those designs accommodated thermal management challenges in electronic packaging, further investigation is still required for the thermo-mechanical performance of the heat guiding structures in macroscale power semiconductor devices. The introduction of the topology optimization technique created a world of possibilities for the optimal design of heat guiding structures under desired

objectives. Existing studies have extensively investigated topology optimization with mechanical boundary conditions for maximizing mechanical stiffness [90]–[96] and thermal boundary conditions for maximizing temperature diffusivity. Iga *et al.* considered thermal conduction and convection boundary loading in the topology optimization of structural designs [97]. Zhang *et al.* developed a numerical topology optimization model for isotropic and anisotropic structures to achieve the optimization goal of the least dissipation of heat transport potential capacity [98]. Lundgaard *et al.* presented a density-based topology optimization method for thermal energy systems by coupling fluid and heat transfer models [99]. Zhou *et al.* applied design-dependent convection in conjunction with conduction topology optimization for industrial applications[100]. Topology optimization has been successfully applied to electronic systems, enabling actively cooled system integration into downhole electronics [101], thermal-composite design optimization for thermal management of printed circuit board (PCB)-based electronics [2], design of power semiconductor modules using topology optimization for efficient cooling [102], 3D packages with effective heat removal [103], and heat sinks for tablets [103], and heat sinks for tablets [104]. However, further investigations in systems subjected to coupled thermo-mechanical constraints are still required for electronic packaging applications.

To combine the objectives of maximizing mechanical stiffness while minimizing the temperature gradient, thermo-mechanical topology optimization can be employed [105]. For example, Dede [106] performed thermo-mechanical topology optimization to decrease component weight and increase gravimetric power density in the thermal bracket of a magnetic inductor; Takezawa *et al.* [107] investigated thermo-mechanical topology optimization in arbitrary two-dimensional shapes considering the thermal expansion effect;

Zhu *et al.* [108] studied the temperature-constrained topology optimization for thermoelastic structures under a design-dependent temperature field. However, thermo-mechanical topology optimization in earlier studies has been mainly focused on using multiple materials [109][110], and the optimal designs are generally confined to 2D domains [111]–[115] or are challenging to manufacture [116].

In this study, we developed a thermo-mechanical topology optimization framework based on the finite element method (FEM) for designing novel 3D homogenous heat guiding structures with optimized thermal and mechanical properties, subject to a 50% volume fraction constraint. **Figure 2-1(c)** demonstrates the development of thermo-mechanically optimized heat guiding structures for an unaligned heat source/sink configuration. Thermal, mechanical, and thermomechanical objective functions result in unique topologies that satisfy all applied boundary conditions. A 30  $\mu\text{m}$  minimum dimension constraint has been applied to our design space to ensure the manufacturability of 3D metallic thermo-mechanically optimized heat guiding structures via Laser Powder Bed Fusion (LPBF).



**Figure 2-1** a) Heat transfer path in a conventional packaging scenario where heat-generating component and heat sink are aligned. In this case, components with different temperature tolerances can easily be impacted if positioned in the heat transfer path. b) Heat transfer path in a non-conventional packaging scenario where a heat sink may not be aligned with a heat source. In the presence of several components with different temperature tolerances in the system, novel heat guiding structures with zigzag or S shape designs would be favorable for optimal routing of the heat flow from the heat source to the heat sink. These heat guiding structures may create an efficient heat transfer path while minimizing the thermal interaction with the components of different temperature tolerances. c) Thermo-mechanical optimization process for complex packaging scenarios. The thermal boundary conditions include a heat flux ( $q''$ ) on the heat source side while fixing the temperature on the heat sink side ( $T_{\text{sink}}$ ). The mechanical boundary conditions represent a force applied on the heat sink side and a fixed end on the heat source side.

## 2.2. Topology Optimization of 3D Heat-Guiding Structures

### 2.2.1. Density-based Topology Optimization Algorithm Development

Topology optimization-based finite element methods have been explored in the past to enable heat flow control in arbitrary (e.g., non-circular or non-spherical) geometries [117][118] and bifunctional cloaking [119]. In this chapter, we utilized the 2D thermal conductivity design approach proposed by Dede [118] for heat flux shielding and expanded the approach to a 3D design space domain. Heat flux shielding is a suitable choice for

minimizing the magnitude of the temperature gradient and heat flow within a selected region of a system. Furthermore, this approach allows us to achieve the optimized topology for a given volume fraction while minimizing thermal compliance. For mechanical optimization, a density model with regularization via the Helmholtz equation was used [120]. The optimization problem can be stated as follows:

$$\begin{aligned}
 \min J(z) &= \omega J_m + (1 - \omega) J_\theta & \mathbf{(2-1)} \\
 \text{s.t. } g_j &= \frac{\sum_{e \in \varepsilon_j} v_e \rho_e}{\sum_{e \in \varepsilon_j} v_e} - \bar{v}_j \leq 0 \quad j = 1, \dots, N_c \\
 &e = 1, \dots, N_e \\
 J_m &= u^T K u \\
 J_\theta &= \theta^T \kappa \theta
 \end{aligned}$$

where the objective function  $J(z)$  is defined in terms of mechanical  $J_m$  and thermal  $J_\theta$  objectives, with  $0 \leq \omega \leq 1$  a weight factor ( $\omega = 0.5$  was used for our calculations).  $g_j, j = 1, \dots, N_c$  is the  $j_{th}$  volume constraint to sub-regions of the design domain  $\{\varepsilon_j\}$  [121].  $v_e$  and  $\rho_e$  are the area and density of element  $e$ , respectively; and  $\bar{v}_j$  is the upper limit for the volume constraint  $j$ . We use the equilibrium equation for steady-state linear elastic deformation for defining the mechanical objective function ( $J_m$ ), where  $K$  and  $u$  are the stiffness matrix and displacement vector, respectively. In addition, we consider steady-state conduction in a three-dimensional (3D) domain as the thermal objective function ( $J_\theta$ ), where  $\kappa$  is the thermal conductivity matrix, and  $\theta$  is the nodal temperature vector.

Sufficient penalization of the intermediate densities ( $\rho_e$ ) by an interpolation function is required for convergence of the solution: here, the SIMP (Solid Isotropic Material with Penalization) approach has been implemented in COMSOL. The penalization factor ( $p$ ) can

be set to values greater than 1 for penalizing the intermediate densities [101] for thermal, mechanical, and thermomechanical topology optimization simulations [120]. By utilizing gradient-based optimization techniques, the problem is relaxed by allowing intermediate values of  $0 \leq \rho_e \leq 1$  for the design parameter to exist. The design parameters are bounded from below with  $\rho_{min}$  with the value of 0.001; therefore  $0 < \rho_{min} \leq \rho_e \leq 1$  and we can derive the penalized density ( $\rho_p$ ) as below:

$$\rho_p = \rho_{min} + (1 - \rho_{min})\rho_e^p \quad (2-2)$$

We initialize the optimization process by providing an initial design space and utilizing the material properties of LPBF-manufactured stainless steel (SS316L) for all calculations, with Young's modulus of  $\sim 150$  GPa [122] and thermal conductivity of  $\sim 15$  Wm<sup>-1</sup>K<sup>-1</sup>[123]. Evaluating the sensitivity of the overall objective function with respect to the control variable  $\rho_e$  can be rephrased as calculating the derivative of the objective function  $\left(\frac{\partial J}{\partial \rho_e}\right)$  which can be derived from the sensitivity analysis summarized as below [124]:

$$\frac{\partial J}{\partial \rho_e} = -p\rho_e^{p-1}(1 - \rho_{min})(\omega J_m + (1 - \omega)J_\theta) \quad (2-3)$$

Based on the sensitivity input, the Method of Moving Asymptotes (MMA) [125], which was initially developed for structural optimization problems, is used to update the solution and converge towards optimality.

Optimized electronic packaging heat guide design should deliver a successful thermal management solution and mechanical stability. Therefore, by combining thermal and mechanical requirements, we used Comsol's optimization module and the Globally Convergent of the Method of Moving Asymptotes (GCMMA) [126] as the optimization method with thermal and mechanical boundary conditions. The method of moving asymptotes was



chosen for two main reasons. First, the method was proven to work very well on various topology optimization problems[127]. Second, the method is very popular for parallel computations because of the separable nature of approximations

## **2.3. Results and Discussion**

### **2.3.1. Thermo-mechanical Topology Optimization of Heat Guiding Structures**

Defining an effective thermal path design is crucial for transferring the excessive heat to the heat sink, protecting the components with different thermal tolerances from hot surroundings, and preventing heat leakage. However, the limited available space of the proximity between the heat source and the heat sink makes this task challenging. Moreover, the package should be designed such that the stress in any component does not exceed the permissible extent of that material and can withstand the thermo-mechanical cyclic loading imposed during the system operation. Knowing that the maximum volume fraction of the utilized metal in the PCB board of packaging structures is about 50%, we used this value as a limiting design parameter. Hence, we solved the density-based topology optimization problem for 3D heat guiding structures with an objective volume fraction of 50%. Error! Reference source not found. demonstrates a series of investigated designs for the possible 3D heat guiding structures where the thermal path from the heat source to the heat sink deviates from conventional packaging scenarios. The initial structures have been chosen to demonstrate the impact of varying distances from the heat source to the heat sink in non-conventional thermal management cases. With the additive manufacturing capability, multiple reference structure choices were available for evaluating the performance of the

optimized heat guiding structures. Here, two reference structure designs with a 50% volume fraction were studied. The solid reference structure mimics its initial structure but with 50% of the cross-sectional area. The infill reference structure has an identical geometry as the initial structure but a rectilinear-infill pattern representing 50% porosity. The rectilinear-infill pattern was chosen for its common usage in additive manufacturing [128]–[130] and its opportunities for complex numerical studies.

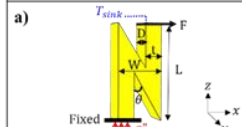
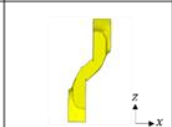


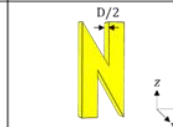

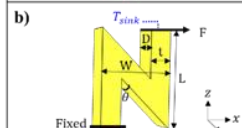
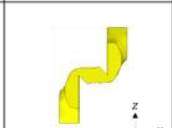


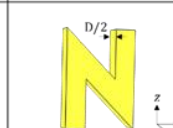

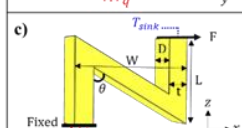
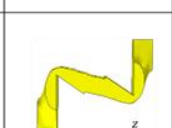

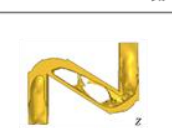
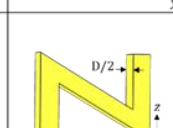
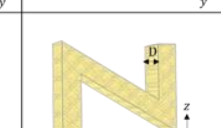
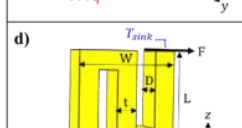
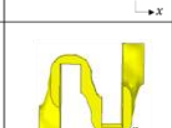


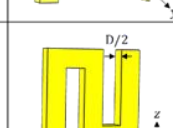
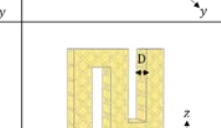
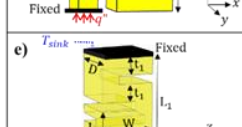
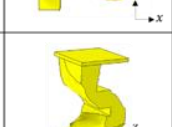
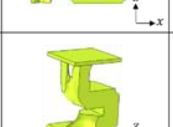
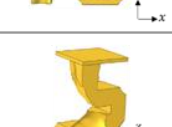
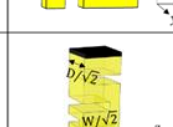
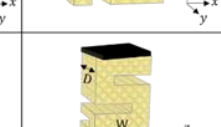
Although multiple reference structure choices were available, such as 50% volume infill patterns for additive manufacturing, a different selection of the infill patterns and density distribution in volume infill reference structures would directly impact the resultant thermal and mechanical properties. Therefore, we needed to have a base standard reference structure for comparing with the topology optimized structures. The reference structure for each investigated design mimics the initial structure but with 50% of the cross-sectional area. The initial design domains with 100% volume fraction provide the smallest thermal resistance for the heat transfer. Therefore, we normalize the thermal resistance of both the optimized topology and the reference structures to the thermal resistance of their initial structure. The topology optimization algorithm creates a path between the heat source and the heat sink with the smallest thermal resistance while preserving the requirements of the density-based objective function. A lower thermally resistive path guarantees a lower maximum temperature at the heat source.

The thermal boundary conditions include applying a heat flux with a representative value of  $250 \text{ Wcm}^{-2}$  [131] on the heat source side and a constant temperature of  $27 \text{ }^\circ\text{C}$  on the heat sink side. The mechanical boundary conditions include a 100 N compression force on the heat

sink side (conversion of the maximum stress around through-silicon vias on the device layer[132]) and a fixed end on the heat source side. At each structure, the boundary conditions are applied to a small window of 2 mm × 2 mm placed at the beam ends with a thickness of 4 mm. The boundary conditions for the investigated design domains were applied to an initial structure with a 100% volume fraction ( **Figure 2-2(a-e)**).

### **2.3.2. Thermo-Mechanical Optimization Results**

The investigated designs show thermal, mechanical, and thermo-mechanical topology optimization results in **Figure 2-2(a-e)**. The solid reference structure of each design for **Figure 2-2(a-d)** mimics the initial structure but with 2 mm thickness in the y-direction. For **Figure 2-2(e)**, W and D values in the solid reference structure were reduced to 10.6 mm, and other parameters remained as demonstrated in the initial structure to reach 50% volume fraction in the reference structure. The infill reference structure has the same thickness as the initial structure in the y-direction (D), but the implemented porosity creates the 50% volume fraction.

Boundary conditions on the initial structure	Thermally optimized structure	Mechanically optimized structure	Thermo-mechanically optimized structure	Solid reference structure	Infill reference structure
a) 					
b) 					
c) 					
d) 					
e) 					

**Figure 2-2:** Boundary conditions and the resultant thermal, mechanical, and thermo-mechanical topology optimization on the following designs. a) Initial structure with parameters of  $\theta=30$ ,  $L=10$  mm,  $W=5$  mm,  $t=2$  mm, and  $D=4$  mm. b) Initial structure with parameters of  $\theta=45$ ,  $L=10$  mm,  $W=7$  mm,  $t=2$  mm, and  $D=4$  mm. c) Initial structure with parameters of  $\theta=60$ ,  $L=10$  mm,  $W=12$  mm,  $t=2$  mm, and  $D=4$  mm. d) Initial structure with parameters of  $L=10$  mm,  $W=10$  mm,  $t=2$  mm, and  $D=4$  mm. e) Initial structure with parameters of  $L_1=30$  mm,  $L_2=12$  mm,  $W=15$  mm,  $t_1=4$  mm,  $t_2=2.5$  mm, and  $D=15$  mm. The solid reference structures for designs (a)-(d) have identical dimensions as their representing initial structures but 2 mm thickness in the y-direction. The solid reference structure for design (e) has identical dimensions as its initial structure but with  $W/\sqrt{2}=D/\sqrt{2}=10.6$  mm. The infill reference structure for all designs (a)-(e) is identical to their initial design but creates a 50% volume fraction with a rectilinear infill pattern.

By applying the thermal boundary conditions demonstrated for each design in **Figure 2-2(a-e)** and examining the temperature gradient across the structure, the thermal resistance for each of the designs was calculated using  $R_{structure} = \frac{\Delta T}{q}$ . For evaluating the thermal performance of each design, thermal resistance was also calculated in the corresponding reference structure. **Table 2-1** summarizes the normalized thermal resistance

$(R_{structure}/R_{initial})$  for both thermal and thermo-mechanical optimization results of each investigated design at which  $R_{initial}$  is the thermal resistance of the initial structure. The initial structures have the largest cross-sectional area (smallest thermal resistance) compared to the optimized and the reference structures; therefore, normalizing the thermal resistance values of the optimized and reference structures to the thermal resistance of the initial structure results in values greater than 1. Since the functions applied to the optimization process do not result in the same topology, the thermo-mechanically optimized structures have inherent tradeoffs in the final structure's thermal and mechanical performance. This tradeoff is demonstrated as a higher normalized thermal resistance in thermo-mechanically optimized structures when compared to the thermally optimized structures for all the studied designs. As simulation results show, the normalized thermal resistance ratios of the infill reference structures are ~50% greater in all designs except for the serpentine design (e), with a ~33% increase compared to the solid reference structures. This increase in thermal resistance is due to a smaller cross-sectional area of the infill reference structure—2.6 mm<sup>2</sup> in designs (a)-(d) and 86.8 mm<sup>2</sup> in the serpentine design (e)—compared to the solid reference structure—4 mm<sup>2</sup> in designs (a)-(d) and 112.4 mm<sup>2</sup> in the serpentine design (e)—. The solid reference structure is selected for future comparisons in this study.

The optimization process results in a heat guiding structure with a maximum stiffness of 6.08 [N/m] in design (e), while its solid reference counterpart showed a stiffness of 4.24 [N/m]. Furthermore, by normalizing the stiffness values to the stiffness of the initial structure of design (e) (8.95 [N/m]), the optimized heat guiding structure demonstrates a 43%

improvement in the normalized stiffness. Using this optimization process, various electronic packaging designs with numerous constraints can be studied.

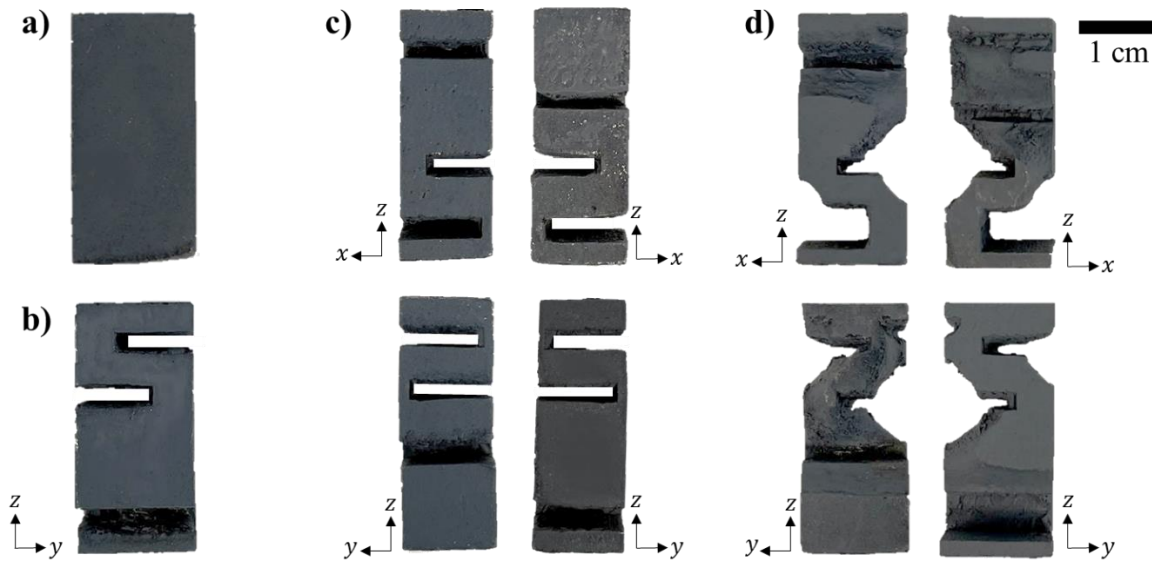
**Table 2-1:** Comparison between the normalized thermal resistance ( $R_{structure}/R_{initial}$ ) of the optimized topology structures and the reference structure of the studied heat guides shown in **Figure 2-2**.

Design	Thermally optimized structure	Thermo-Mechanically optimized structure	Solid reference structure	Infill reference structure
a	1.31	1.43	1.89	2.85
b	1.34	1.49	1.87	2.83
c	1.63	1.78	1.93	2.99
d	1.55	1.82	1.94	2.89
e	1.29	1.37	2.01	2.67

### 2.3.3. Manufacturing and Characterization of 3D Heat-Guiding Structures

To experimentally validate the concept of heat guiding for packaging applications and characterize their thermal properties, the heat guiding structure of design (e) was benchmarked for manufacturing using a Laser Powder Bed Fusion (LPBF) technique. . The structures were fabricated during the 3D manufacturing process corresponding to their input CAD files by selectively melting and consolidating thin layers of SS316L metal powder using a scanner laser beam. The process parameters were optimized via a broad sweep of experiments at many parameter sets, a standard procedure for fabricating porosity-free samples [133][134]. The structures were printed at 400 W laser power, 230 mm/s scan speed, 60  $\mu\text{m}$  hatch spacing, and 30  $\mu\text{m}$  layer thickness. **Figure 2-3** demonstrates the SS316L 3D printed samples based on the design (e). As shown in **Figure 2-2(e)**, the dimensions of this design with 15 mm width and 30 mm height were slightly larger than designs (a-d). The reason behind this selection was the bottom-up manufacturability of the structures. Mechanical supports were implemented within the structural gaps for the 3D printing

process that were later removed manually. A reference characterization sample was fabricated for characterizing the intrinsic thermal properties of the 3D printed SS316L (**Figure 2-3(a)**). **Figure 2-3(b)** demonstrates the fabricated initial structure followed by its corresponding solid reference structure with 50% volume fraction (**Figure 2-3(c)**) and the topology optimized heat guiding structure (**Figure 2-3 (d)**) after post-processing.

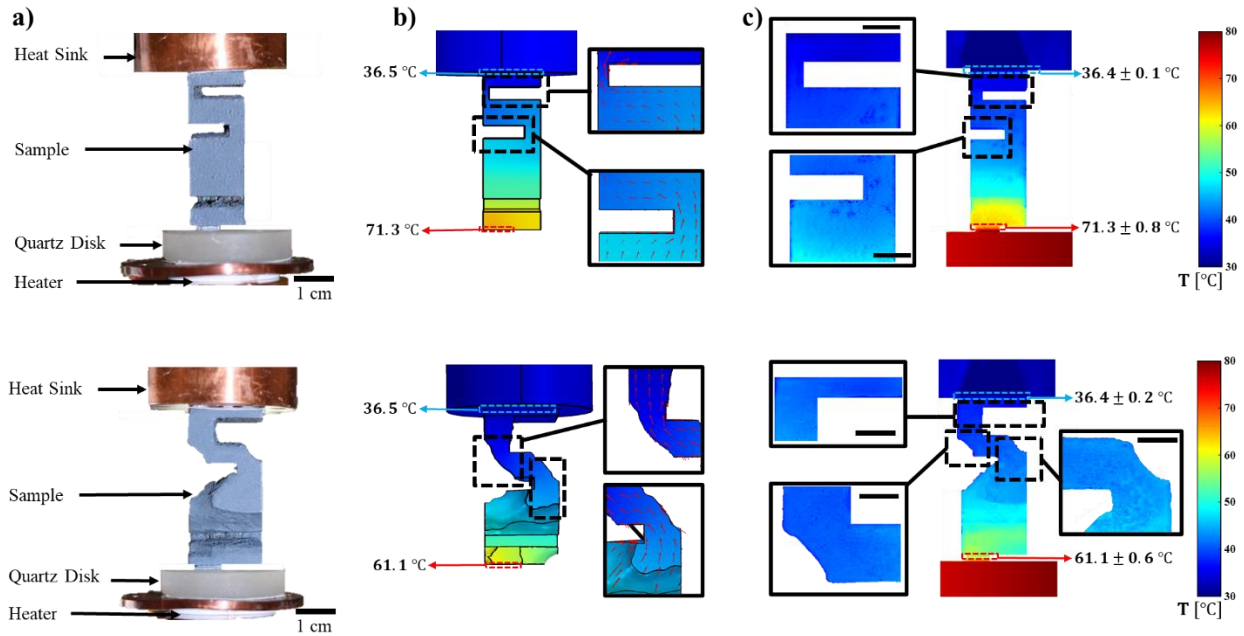


**Figure 2-3:** Demonstration of the design (e) 3D printed steel structures after post-processing and emissivity coating. a) A reference characterization sample was fabricated for characterizing the properties of additively manufactured steel along with b) the initial structure ( $\nu = 100\%$ ), c) the reference structure with 50% volume of the initial structure ( $\nu = 50\%$ ), and d) the optimized heat guiding structure ( $\nu = 50\%$ ).

The post-processed samples were coated with a high emissivity coating spray (RUST-OLEUM high heat primer) and were thermally characterized using the infrared thermography method [135]. The samples were placed in a JANIS VPF-800 vacuum chamber in a vacuum level below  $10^{-5}$  Torr (high vacuum range). The surface emissivity of the applied coating was calibrated as  $0.810 \pm 0.013$ . The estimated error in the calibrated emissivity results in temperature reading with  $\pm 0.5$  °C inaccuracy. Using the calibrated emissivity value, the thermal conductivity of the reference characterization sample was measured as  $14.18 \pm 1.13$

$\text{Wm}^{-1}\text{K}^{-1}$  through utilizing the infrared thermography methodology discussed in Farzinazar *et al.* [135]. This value is in good agreement with previously reported thermal conductivity values for additively manufactured stainless steel 316L (SS316L) samples [123]. Iceberg Thermal DRIFTIce 0.5 mm thermal pad with thermal conductivity of  $13 \text{ Wm}^{-1}\text{K}^{-1}$  (provided by the vendor) was used as the Thermal Interface Material (TIM) between the fabricated samples and the heat source/heat sink. A constant heat flux of  $5.1 \text{ Wcm}^{-2}$  was applied to both reference design and optimized heat guiding structures with a similar volume fraction of 50%. A reference quartz disk with known thermal conductivity of  $1.38 \text{ Wm}^{-1}\text{K}^{-1}$ , a diameter of 25 mm, and a thickness of 6.33 mm was used to calibrate the heater's incoming heat flux (**Figure 2-4(a)**). The actual experimental setup was oriented such that the heater was placed on the top and the heat sink at the bottom. However, since in most packaging scenarios the heat sink is placed on top of the package, the experimental setup image was flipped (**Figure 2-4 (a)**) for a direct comparison with a practical application design. The IR images show the temperature contour across the samples and the quartz disk due to the applied heat flux **Figure 2-4(c)**. The measurement of incoming heat flux and temperature gradient in both samples resulted in thermal resistance of  $171.1 \pm 12.8 \text{ KW}^{-1}$  and  $121.1 \pm 9.3 \text{ KW}^{-1}$  in the reference and optimized heat guiding structures.





**Figure 2-4:** a) Demonstration of the IR thermography experimental setup for the reference structure (Top) and the optimized heat guiding structure (Bottom) b) Numerical analysis of the reference sample (Top) and the optimized heat guiding structure (Bottom) with the measured boundary conditions of heat flux of  $5.1 \text{ Wcm}^{-2}$  on the top and a constant temperature of  $33 \text{ }^\circ\text{C}$  in the copper sample holder. The inset figures represent the direction of heat flow using the red arrows. While the reference structure restrictions cause the heat flux concentration in the narrow regions, the optimized heat guiding structure has an optimized distribution of material to prevent heat flux concentration. c) IR images demonstrating the temperature contour in the reference structure (Top) and the optimized heat guiding structure (Bottom). The scale bar in inset images represents 5 mm.

As demonstrated in **Figure 2-4** Error! Reference source not found. (c), the maximum temperature in the reference structure is  $71.3 \text{ }^\circ\text{C} \pm 0.8 \text{ }^\circ\text{C}$  whereas, in the optimized heat guiding structure with a similar volume fraction, this value reaches  $61.1 \text{ }^\circ\text{C} \pm 0.6 \text{ }^\circ\text{C}$ . Numerical simulation results with the measured heat flux value of  $5.1 \text{ Wcm}^{-2}$  and a constant temperature of  $33 \text{ }^\circ\text{C}$  in the copper anchored heat sink was performed for both reference and the optimized heat guiding structures (**Figure 2-4(b)**). The thermal contact resistance is crucial for determining the maximum and minimum temperatures across the fabricated samples. We characterized the thermal contact resistance on the sample/TIM interfaces on the heat source

and the heat sink sides using the calibrated heat flux values and the temperature gradient across the sample/TIM interface. On the heat sink side, the values were  $1.5 \pm 0.3 \times 10^{-4} \text{ Km}^2/\text{W}$  and  $1.3 \pm 0.2 \times 10^{-4} \text{ Km}^2/\text{W}$  in the reference and the optimized structure, respectively. On the heat source side, the thermal contact resistance was estimated as  $2.8 \pm 0.6 \times 10^{-4} \text{ Km}^2/\text{W}$  and  $2.6 \pm 0.5 \times 10^{-4} \text{ Km}^2/\text{W}$  in the reference and the optimized structure, respectively. The thermal contact resistances are smaller on the heat sink side. The main reasons are (1) a higher apparent contact pressure (due to the weight of the system) and (2) a smoother surface quality (due to better polishing). On the heat sink interface, the corresponding estimated thermal contact resistances were used in the simulations. On the heat source side, the contact resistance values were adjusted in the simulation using a parametric study to  $2.6 \times 10^{-4} \text{ Km}^2/\text{W}$  in the reference structure and  $2.2 \times 10^{-4} \text{ Km}^2/\text{W}$  in the optimized structure for meeting the measured maximum temperature values. The difference between the estimated average thermal contact resistance values and the simulation results can be attributed to the uncertainties in temperature measurement, heat flux calibration, and the resolution of the Infrared camera— $25 \mu\text{m}/\text{pixel}$ — for thermal interface investigations. It is worth mentioning that the reported thermal contact values are consistent with the thermal contact resistance values of elastomer-like gap pads reported in the literature [136].

Advanced 2.5D and 3D packages could be suffered from nontrivial thermal management challenges such as thermal crosstalk and high hot spot heat fluxes that are in the order of  $1 \text{ kWcm}^{-2}$ . The associated packaging structures may benefit from the new capabilities to guide heat in the unaligned heat source and sink configurations through topology optimization. As demonstrated in **Table 2-1**, the thermo-mechanical topology optimization of heat guiding structures results in a degradation in performance as a tradeoff for solving for mechanical

objective function in conjunction with the thermal objective function. However, thermal topology optimization and thermo-mechanical topology optimization result in structures with a smaller normalized thermal resistance (lower average temperature) than their reference structure counterpart with an identical volume fraction. Our experimental and numerical investigations on the design (e) heat guiding structure have confirmed lower thermal resistance in topologically optimized structures. On average, the optimized heat guiding structure demonstrated a  $50 \text{ KW}^{-1}$  smaller thermal resistance compared to its reference structure counterpart. This difference in thermal resistance can be translated into a  $180 \text{ }^\circ\text{C}$  higher temperature in the reference structure when the heat flux varies from 10 to  $100 \text{ Wcm}^{-2}$ . In addition to the thermal-mechanical co-optimization, future research and development in multidisciplinary optimization may provide joint efforts to improve thermal management techniques at multiple levels. The optimized complex heat guiding designs can be achieved through the 3D printing technique, which needs more studies to improve its process flow, compatibility, and scalability. Moreover, investigations on the implementation methods are also required to address the chip integration and provide package-level solutions.

## **2.4. Conclusions**

Recent advancements in electronic packaging require customized thermal management solutions to enable guiding the excessive heat in unaligned configurations of heat source and heat sink and fulfilling the mechanical requirements. We presented a density-based topology optimization method to find thermally conductive and mechanically stable structures for optimal heat guiding in non-conventional packaging scenarios. We investigated serpentine

designs with different effective lengths from the heat source to heat sink that is potentially suited for guiding the heat from the system level hotspot to the heat sink while securing the possible adjacent components with different temperature tolerances. Using density-based thermo-mechanical topology optimization and assuming 50% volume fraction constraint, we fabricated a prototype of the thermally optimized design (e) heat guiding structures. Our experimental results demonstrated 29% lower thermal resistance than its reference counterpart with an identical volume fraction. This finding suggests that topology-optimized heat guiding structures can control the heat flux and provide higher thermal performance than their reference structure counterparts with an equal volume fraction constraint. Future electronic packaging may benefit from the combined efforts across the advanced optimization process and manufacturing techniques for optimal thermal management solutions. Consequently, the resultant heat guiding structures from topology optimization and 3D manufacturing can potentially be used as a stepping stone towards thermal computing in the future.

# CHAPTER 3

## Engineering Thermal Properties in Metallic Microlattices

### 3.1. Introduction to ultralight hollow nickel microlattices

Recent advances in additive manufacturing have led to architected materials with strongly hierarchical topologies and distinctive properties such as ultrahigh strength, ultrahigh surface-to-volume ratio, and ultralow density [7], [36], [37], [137]. High precision additive manufacturing techniques such as self-propagating photopolymer waveguides (SPPW)[138], direct laser writing (DLW) [34][35], and projection micro-stereolithography (PμSL) [139] have enabled the fabrication of lattices with submicron feature sizes [6] [140]–[142] and high porosity up to 99.9%. These microlattices and nano-lattices can offer remarkably high specific stiffness and strength [143], or full recovery from extensive compressive strains (> 50%) and associated structural damping [36][37], despite their constituent materials being inherently brittle. When designed and fabricated at low relative densities, these architected materials will provide an exceptionally low thermal conductivity, even with highly conductive constituents [144]. This combination of mechanical and thermal properties could make these materials ideal for thermal

insulation in several aerospace systems, from gas turbines to hypersonics, where a combination of high strength and low thermal conductivity is desirable. Schaedler *et al.* [36] demonstrated that hollow nickel microlattices could be fabricated using SPPW and electroless plating to span more than seven orders of magnitude in length scale, which provides excellent control over the design and resultant properties [145]. Furthermore, high recoverability upon each cyclic loading creates an opportunity for thermal management via modulation of the applied force. The thermal properties of these microlattices are explored in this work. While the unique mechanical properties of architected microlattices have been actively investigated in recent literature [146][36][37][32][145], their associated thermal properties, including the capability of manipulating heat flows, have received little attention. Dou *et al.* measured the thermal conductivity of nanoscale lattices [147] using electrical resistance thermometry while heating the structure from 95 to 300K with a microfabricated heater in contact with the lattice. However, neither Dou *et al.* nor other studies on the thermal characterization of highly porous media [148]–[151] have explored the effect of mechanical loading on thermal transport, the variation of thermal conductivity at high temperatures, or the contribution of radiation to the effective thermal conductivity. Using a noncontact temperature measurement approach, we developed a novel methodology to minimize the errors created by other in-contact metrologies for the thermal conductivity measurement of highly porous structures. This approach allows us to decouple the dominant heat transfer modes in highly porous structures—conduction and radiation—and study their contributions individually. This methodology also eliminates the resultant error from the thermal contact resistance between the hollow nickel microlattice and its adjacent objects. Here, we report the effective thermal

conductivity of hollow nickel microlattices as a function of temperature and mechanical loading.

### 3.2. Materials and Methods

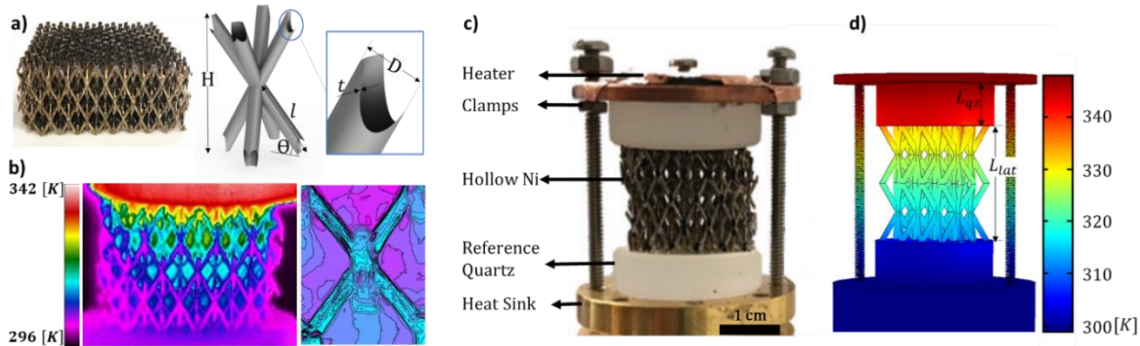
All samples were fabricated at HRL Laboratories with the SPPW method. This technology enables the formation of three-dimensional hollow nickel microlattices from a two-dimensional exposure mask [138]. The fabrication procedure consists of fabricating the polymeric sacrificial layer, coating the sample with electroless doped Ni deposition (93% Ni and 7% P by weight), and etching the sacrificial core, ultimately resulting in a series of octahedral unit cells with hollow struts that are connected at nodes [145][152][153] (**Figure 3-1 (a)**). The coating material was not annealed after the deposition, resulting in a supersaturated solid solution of phosphorous in a crystalline nickel lattice. This technique results in feature sizes in the order of  $1\ \mu\text{m}$ . Considering the mean free path of nickel in the range of 6 nm [154], the contribution of boundary scattering is minimal, and therefore, macroscopic heat transfer governs the energy balance equations. All lattice feature dimensions have been characterized using the Scanning Electron Microscopy (SEM) and the results are summarized in **Table 3-1**.

The thermal conductivity measurement was performed using the setup demonstrated in **Figure 3-1(c)**. The sample was assembled between two quartz disks, and the stack was placed between a heat source and an anchored heat sink in a vacuum environment. A JANIS VPF-800 vacuum chamber was utilized for housing the sample, and an Edwards T-station 75 turbopump was used for maintaining the vacuum level below  $10^{-5}$  Torr (high vacuum range) for each measurement. By turning on the heater, the heat propagates from the top toward the

anchored heat sink. The hollow nickel microlattice is an effective medium, and the nonlinear temperature gradient results from both conduction and radiation heat losses, as confirmed by finite element simulations (**Figure 3-1 (d)**). The incoming heat flux was calculated using the known thermal properties of the quartz disk and the temperature gradient within the quartz. The effective thermal conductivity of the lattice was computed using the temperature gradient in IR images (**Figure 3-1 (b)**) and the incoming heat flux.

**Table 3-1:** Feature parameters in addition to the surface finish of the samples used for experiments. Truss angle ( $\theta$ ), length ( $l$ ), wall thickness ( $t$ ), and bar diameter ( $D$ ) were measured using SEM with an accuracy of  $\pm 2^\circ, \pm 3\%, \pm 10\%, \pm 15\%$  respectively. The volume fraction ( $v$ ) has been calculated based on the CAD model of each unit cell.

	Sample 1	Sample 2	Sample 3
$v$	0.09%	0.09%	0.15%
$D$ ( $\mu\text{m}$ )	650	650	500
$l$ (mm)	3.9	3.9	3.9
$\theta$ ( $^\circ$ )	60	60	60
$t$ ( $\mu\text{m}$ )	1	1	2
Surface finish	Polished	Rough	Polished



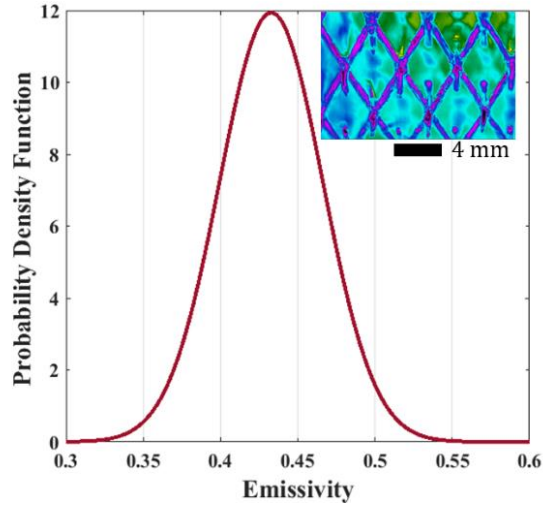
**Figure 3-1** a) The hollow doped nickel microlattice in addition to the unit cell with geometric features.  $\theta$  was set to  $60^\circ$  while ranges of 9-10.5mm for  $H$ , 1-2 $\mu\text{m}$  for thickness and 500-650 $\mu\text{m}$  for the diameter was explored b) Corresponding IR image of the experimental setup along with the temperature distribution of a unit cell. c) The experimental setup used for thermal conductivity measurement of hollow nickel microlattices. The applied clamps are used to change the heater's height in thermal conductivity measurement under compression. d) The FEM simulation of the whole setup illustrates the heat transfer throughout the stack.



The IR thermography is set to distinguish the emitted infrared radiation from an object as a function of the emissivity and temperature of the object, distance to the camera, the ambient and reflected temperature (temperature of the surrounding objects), and the relative humidity of the ambient [155]. For calibration, an isothermal condition is achieved for the lattices and glasses individually by placing the object between two parallel heaters in a vacuum environment until the temperature gradient fades away. Using an image processing technique, the background is eliminated for each IR image, and the temperature is recorded for variable emissivity values. The peak value in the probability density function plot resulted in  $\epsilon_{rough, \nu=0.09\%} = 0.043 \pm 0.03$  for the dark surface finish sample,  $\epsilon_{polished, \nu=0.09\%} = 0.024 \pm 0.02$  for the sample with the reflective surface and  $\epsilon_{glass} = 0.81 \pm 0.02$  for the quartz windows. These values were used as an input for the camera for all temperature measurements. The emissivity values calibrated at the highest measured temperature for thermal conductivity, 480 K, only increased 5% and 6% for the lattice structures with higher and lower emissivity values, respectively (**Figure 3-2**). This finding justifies using a single emissivity value for temperature measurement in all temperature-dependent thermal conductivity data acquisition. In addition, the intrinsic thermal conductivity of microcrystalline electroless nickel is reported as  $60 \text{ Wm}^{-1}\text{K}^{-1}$  [156], while the intrinsic thermal conductivity of pure nickel reaches  $90 \text{ Wm}^{-1}\text{K}^{-1}$  [157]. Based on the measured temperature gradient across the lattice and the heat flux and emissivity values and using FEM simulations result, the intrinsic thermal conductivity of our hollow nickel microlattices is estimated as  $60.7 \text{ Wm}^{-1}\text{K}^{-1}$ .

The temperature map of the lattice from the IR camera is post-processed to eliminate the background noise and calculate the emissivity of each pixel. The probability density function

for each lattice structure is derived, and the most probable value of occurrence is designated as the object's emissivity. Here we demonstrate the Probability density function for sample 2 calibrated at 340 K (**Figure 3-2**).



**Figure 3-2** Probability density function for the emissivity values of the sample2 with a darker surface finish. The image taken by the IR camera with the 25um add-on lens resolution is shown in the inset

Various theoretical and empirical correlations were used in the literature for modeling the thermal conductivity of 2-dimensional composites [43][158][41]. Ashby [159] proposed that the conduction contribution in a connected network of struts should incorporate the thermal properties of the constituent material, the topology of the unit cell, and the volume fraction of the structure. Therefore, the effective thermal conductivity of cellular solids inside the vacuum environment can be described as  $k_c = \frac{1}{3} \cdot \bar{\rho} \cdot k_{sol}$ , where  $\bar{\rho}$  is the volume fraction of the solid (also known as the relative density of the architected material), and  $k_{sol}$  is the intrinsic thermal conductivity of the constituent solid. The factor 1/3 represents the fraction of struts aligned with the heat flux direction. As for the microlattices under consideration this fraction equals  $\sin\theta$ , we express the conductive contribution to the effective thermal conductivity as:

$$k_{cond} = \sin\theta \cdot \bar{\rho} \cdot k_{sol} \quad (3-1)$$

where the volume fraction of solid,  $\bar{\rho}$ , can be expressed at first order as [160]:

$$\bar{\rho} = 2\pi \cdot D \cdot t / (\cos^2 \theta \cdot \sin\theta \cdot l^2) \quad (3-2)$$

where  $D$ ,  $t$  and  $l$  are the diameter, thickness, and length of the hollow struts, respectively, and  $\theta$  is the angle of the struts with the horizontal plane, as illustrated in **Figure 3-1(a)**.

The effective thermal conductivity is a summation of the conduction and radiation contributions,  $k_{cond}$  and  $k_{rad}$ . Following the approach suggested by *Zhao et al.* [161], the radiative thermal conductivity is calculated based on the radiation heat flux, a function of the view factors, radiosity, calibrated emissivity, volume fraction, and temperature. The effective thermal conductivity is then a summation of the conduction and radiation contributions. We used the diffraction theory and the geometric optic laws to use the Rosseland mean coefficient [162] for the radiative analytical model. The effect of strut shapes and their angular configuration on irradiance was employed using the view factors. Details on the derivation of view factors are provided in **Appendix A**. The radiation contribution to the conductivity was calculated based on the surface-to-volume ratio of hollow nickel microlattices.

Hence the effective thermal conductivity can be expressed as:

$$k_{eff} = k_{cond} + k_{rad} = \sin\theta \cdot \bar{\rho} \cdot k_{sol} + [(q_{rad,Y})_{emission} + (q_{rad,Y})_{reflection}] / (\Delta T \cdot L_{lat}^{-1}) \quad (3-3)$$

with  $\Delta T$  as the vertical temperature gradient in the sample and  $L_{lat}$  depicted in **Figure 3-1(d)**.

To calculate the radiative conductivity ( $k_{rad}$ ), the radiative heat flux must be solved ( $q_{rad}''$ ).

The total heat flux will be the summation of conduction and radiation contributions:

$$q_{net}'' = q_{cond}'' + q_{rad}'' = -k_{eff} dT/dy \quad (3-4)$$

Where  $q_{rad}$  comprises of reflection and emission contributions. As a result, the total irradiation ( $Q_{rad}$ ) will be examined in the z-direction at first as follows:

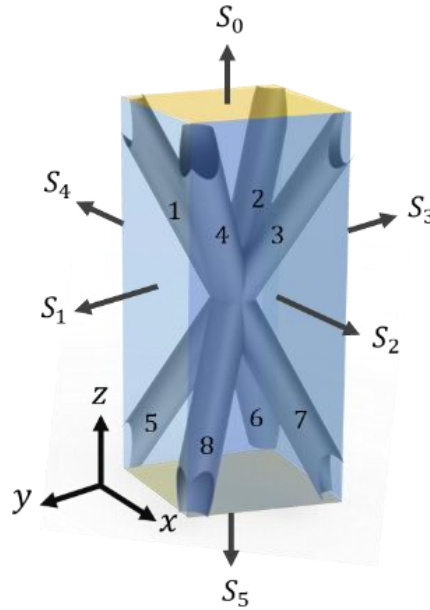
$$Q_{rad,z} = (Q_{rad,z})_{emission} + (Q_{rad,z})_{reflection} \quad \mathbf{3-5 (a)}$$

$$(Q_{rad,z})_{emission} = \sum_{i=1}^8 A_i F_{iS_0} \epsilon \sigma T^4 + \sum_{n=S_1}^{S_5} J_n F_{nS_0} A_n \quad \mathbf{(b)}$$

$$(Q_{rad,z})_{reflection} = \sum_{n=S_1}^{S_5} \sum_{i=1}^8 (J_n F_{ni} A_n) R F_{iS_0} + \sum_{i=1}^8 \sum_{j=1, j \neq i}^8 \epsilon A_i F_{ij} \sigma T^4 R F_{iS_0} \quad \mathbf{(c)}$$

In the equations above,  $\sigma = 5.669 \times 10^{-8} W m^{-2} K^{-4}$  is the Stefan–Boltzmann constant,  $R = 1 - \epsilon$  is the solid reflectivity,  $A_i$  is the solid surface of the  $i$ th strut ( $i = 1, 2, \dots, 8$ ) within a unit cell,  $J_n$  and  $A_n$  are the irradiation and surface area of the void surfaces ( $n = S_1 - S_5$ ),  $F_{iS_0}$  is the configuration factor from the  $i$ th strut to surface  $S_0$ ,  $F_{nS_0}$  is the configuration factor from the  $n$ th surface to surface, while  $F_{ni}$  is the configuration factor from the  $n$ th surface to the  $i$ th strut surface.  $F_{ij}$  is the configuration factor between struts, which is equal to zero if the  $j$ th rod is the continuation of the  $i$ th rod (i.e.  $F_{28} = 0$ ). All configuration factors are derived based on their angular position towards each other and void surfaces (**Appendix A**), and irradiation was calculated based on the equations provided by *Zhao et al.* [161]. The total irradiation in both x and y directions follow the same approach; therefore, the radiative conductivity is calculated as below:

$$k_{rad} = q_{rad}'' / [(T_h - T_c) \cdot H] \quad (3-6)$$



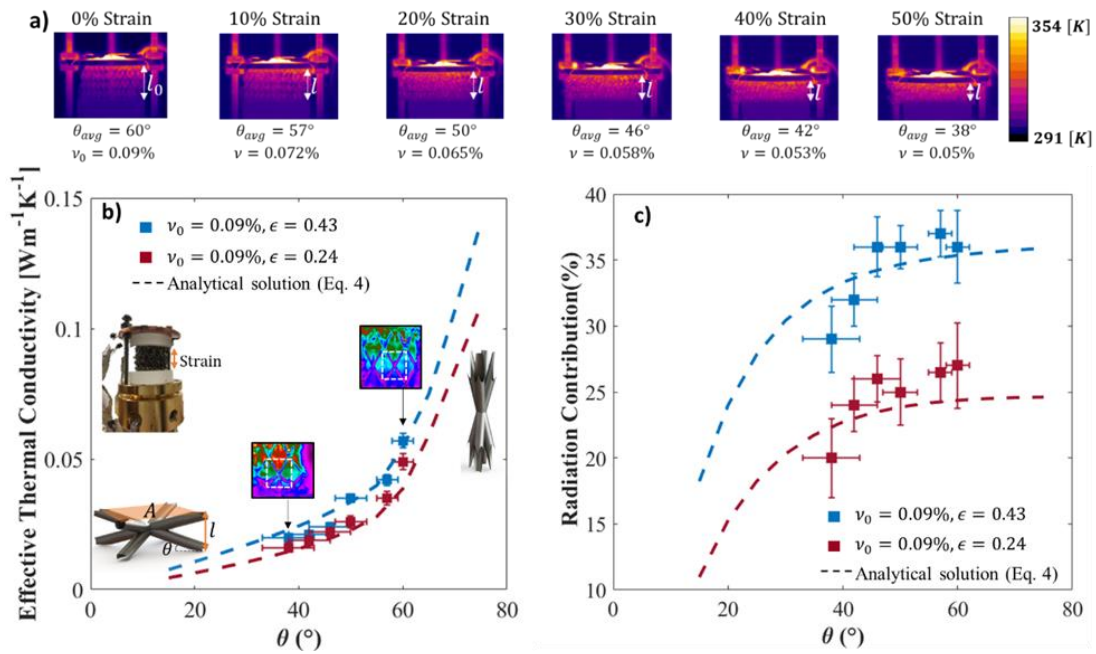
**Figure 3-3** Lattice structure model for radiative conductivity and notations

### 3.3. Results and Discussion

#### 3.3.1. Compression Dependent Thermal Conductivity

High recoverability after compressive deformation of hollow nickel microlattices motivated us to measure the effective thermal conductivity under varying compression levels. Each compression cycle creates a discontinuity inside the medium due to crack initiation, especially at nodes that are more prone to crack formation. We discovered that after three loading-unloading cycles, the crack initiation saturates; thus, we were able to study the impact of strain as an individual factor. Herein, the strain is defined as the ratio of the height reduction in the sample to the initial height (engineering strain). The measurement was performed in a vacuum environment, and the effective thermal conductivity was measured under compression from 0% to 50% strain for the samples with a 0.09% volume fraction.

By increasing the force, unit cells start sliding on top of the glass in the lateral space domain and obtain a smaller  $\theta$  each time. The change in  $\theta$  is not uniform across the structure; as a result, we report each strain cycle with a representative average  $\theta$  value (**Figure 3-4 (a)**) ranging from  $60 \pm 2^\circ$  for the 0% strain and  $38 \pm 6^\circ$  for the 50% strain. As illustrated in **Figure 3-4 (b)**, increasing the strain causes a reduction in the effective thermal conductivity. This effect can be rationalized by noting that the applied strain reduces the strut angle,  $\theta$ , thus affecting the conductive contribution to the effective conductivity both directly [**Equation (3-1)**] and through the volume fraction [**Equation (3-2)**]. While the volume fraction is a concave function of  $\theta$ , the effective thermal conductivity keeps decreasing by decreasing the  $\theta$  value, ultimately resulting in the trend displayed in **Figure 3-4 (b)**. The dashed lines represent our analytical solution, obtained using **Equation (3-3)**.



**Figure 3-4** a) The strain is defined as  $\delta = (l_0 - l)/l_0$  in which  $l$  is identified in each image. Increasing the applied force causes the unit cells to slide, reducing  $\theta$  in a non-uniform manner. The representative average  $\theta$  value and volume fraction for each compression cycle is reported. b) The experimental data and analytical modeling for two samples with the same volume fraction and different surface finishes are illustrated as a function of  $\theta$  on

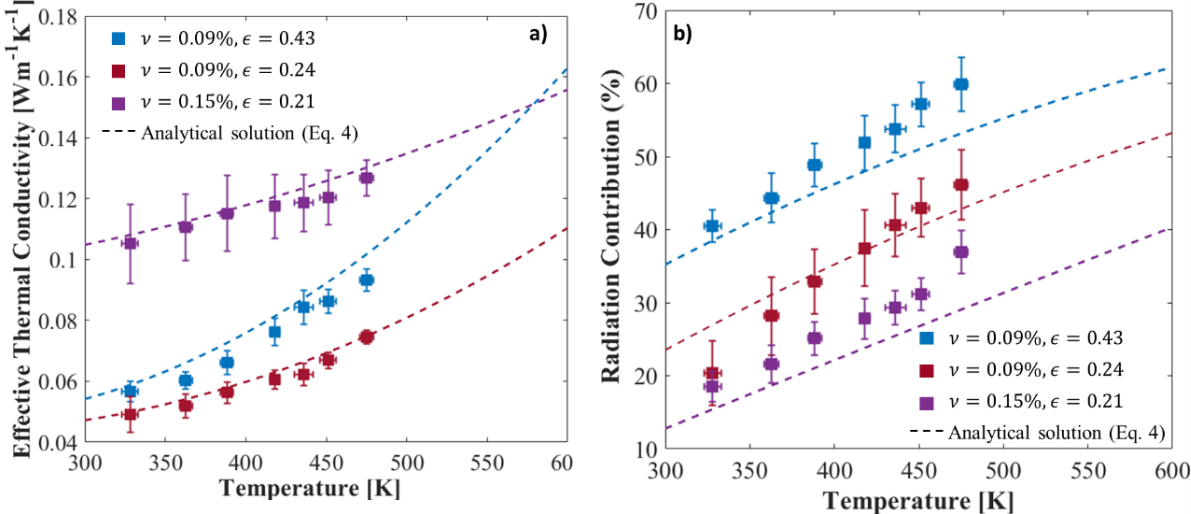
the left axis. The analytical model is verified by the FEM results for unit cells with angles ranging from 15 to 75°. Increasing strain results in a decrease in the structural length and an increase in the structure's area. Consequently, the Fourier equation explains the reduction in the conduction contribution of the effective thermal conductivity ( $k_{\text{eff}}=ql/\Delta TA$ ). c) The radiation contribution is defined as the ratio of the radiative thermal conductivity over the effective conductivity. Reducing  $\theta$  leads to a lower contribution of radiation, correlated with reducing the effective thermal conductivity.

Additionally, reducing  $\theta$  leads to the reduction of view factors in radiation contribution. The reduction is caused by the decrease in angle, leading to reduced radiative interaction between struts and surroundings. The radiation contribution as a function of  $\theta$  illustrates how the increase in view factors cause a significant input of radiative conductivity on the overall effective thermal conductivity at 320 K, **Figure 3-4 (c)**.

### 1.3.2. Temperature-Dependent Thermal Conductivity

Even though the intrinsic thermal conductivity of metals does not change significantly at temperatures higher than ambient [163], the radiative thermal conductivity and the resultant effective thermal conductivity strongly depend on the temperature, **Figure 3-5 (a)**. The dashed lines in **Figure 3-5** demonstrate the radiative conductivity modeling of the hollow nickel microlattices, and their slope is derived by the surface emissivity and surface-to-volume ratio of the samples. Hollow nickel microlattices with the volume fraction of 0.09% exhibit a significant radiation contribution of  $20.40 \pm 4.46\%$  and  $40.50 \pm 2.23\%$  in the case of the polished and rough samples, respectively (**Figure 3-5 (b)**). This phenomenon is mainly due to these samples' high surface-to-volume ratio ( $\sim 1000 \text{ mm}^{-1}$ ), which signifies the radiation contribution even at low temperatures. The sample with the 0.15% volume fraction shows a higher thermal conductivity compared to the polished sample with a similar surface emissivity ( $\epsilon_{\text{polished},v=0.15\%} = 0.21 \pm 0.02$ ). This is mainly due to the increase in the

conduction contribution as a result of increasing the solid constituent of the material. The sample with the rough surface finish demonstrates the highest effective thermal conductivity value at 560 K among all samples due to the highest thermal conductivity growth rate governed by larger surface emissivity. These findings indicate that surface finish could be another approach to change the effective thermal properties at ultra-low-density ranges without affecting the mechanical properties for high-temperature applications.



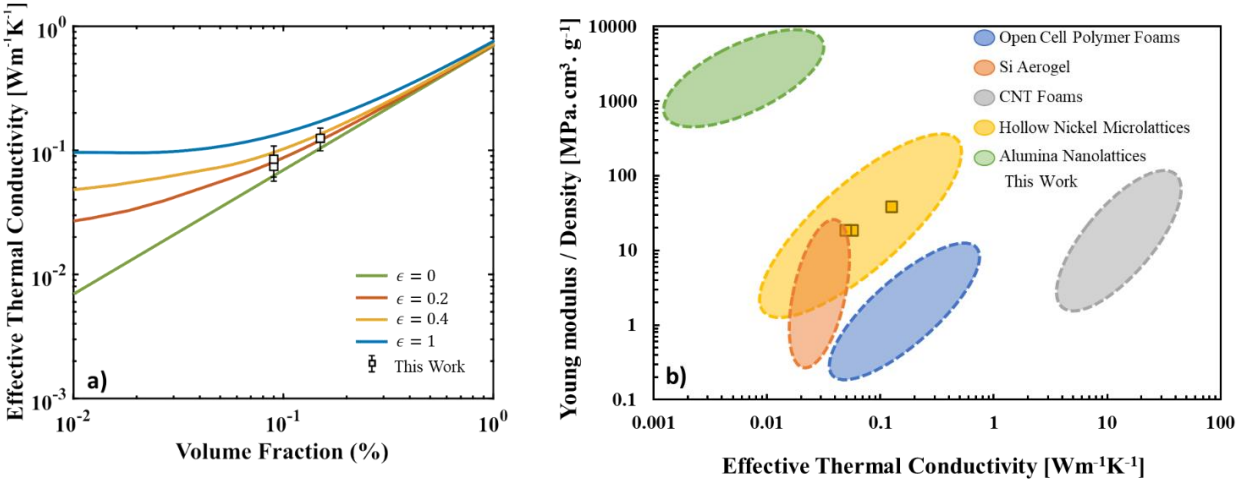
**Figure 3-5** a) The effective thermal conductivity of the samples with 0.09% and 0.15% volume fraction values was measured as a function of temperature. The difference between the blue and red data points illustrates the contribution of surface emissivity in samples sharing the same volume fraction. The slope of the dashed lines shows the rate of growth in the effective thermal conductivity as a result of radiation contribution. b) The radiation contribution of all samples is derived as a function of temperature while the dashed lines demonstrate the analytical modeling.

### 1.3.3. Thermo-Mechanical Evaluation of Hollow Nickel Microlattices

Using the reported mechanical properties of hollow nickel microlattices [36][160], we examined the thermomechanical performance of these structures on a plot of specific Young’s modulus vs. effective thermal conductivity, **Figure 3-6(b)**. Exploiting the architecture in hollow nickel microlattices results in a reduction of thermal conductivity 1000 times from the metal section to the foams. The scaling law of Young’s modulus for these structures follows



as  $E \sim \bar{\rho}^2$  in contrast to its competitors in the ultralight aerogel and carbon nanotube foam (CNT) family ( $E \sim \bar{\rho}^3$ ); therefore the architectural order of these microlattices makes their relative compressive modulus privileged compared to silica Aerogels [164], open-cell polymer foams<sup>35</sup>, and CNT foams<sup>36</sup> in a similar volume fraction range. A direct correlation between the effective Young's modulus and effective thermal conductivity with the volume fraction results in designated areas in **Figure 3-6(b)**. These ellipses are evaluated to be a function of the volume fraction and bulk properties of the constituent material ( $E_{sol}, \rho_{sol}, k_{sol}$  in which  $E_{sol}$  and  $\rho_{sol}$  are the Young's modulus and the density of the bulk material, respectively). **Figure 3-6(b)** illustrates a design space for reaching an ultralow thermal conductivity value by modifying the volume fraction and surface finish of the lattice structure.



**Figure 3-6** a) The design space demonstrates the potential effective thermal conductivity values as a function of volume fraction and surface emissivity using Equation (4) Beyond 1% volume fraction, all lines (representing different emissivity values) converge; demonstrating conduction as the primary mode of heat transfer. Comparatively, radiation contribution signifies below 1% volume fraction, exposing the difference in the effective thermal conductivity at a specific volume fraction. b) Hollow nickel microlattice placement in the material property plot of specific Young's modulus versus effective thermal conductivity. Dashed outlines indicate the allocated region for each material using the Ashby model for cellular solids[159], while markers

represent the measured data points. Hollow nickel microlattices can obtain higher mechanical strength and lower effective thermal conductivity than other mesoscale cellular materials.

### **3.4. Conclusions**

Hollow nickel microlattices offer volume fractions up to an order of magnitude lower than conventional materials and provide a specific Young's modulus superior to conventional ultralight materials. Beyond the well-known mechanical advantages, we have shown the thermal properties of the microlattices by measuring the effective thermal conductivity as a function of compression and temperature. The hollow nickel microlattices possess a high surface area to volume ratio; this yields a significant radiation contribution that is apparent even at temperatures where radiation is not typically considered a dominant mode of heat transfer. Our measurements demonstrated that the increasing contribution of radiation subsequently increases the effective thermal conductivity of the lattice structure as the temperature is raised. Analytical modeling highlighted the radiation as the dominant heat transfer mode in hollow nickel microlattices with the surface emissivity of 0.43 at a temperature as low as 420 K. Furthermore, measuring the effective thermal conductivity under compressive strain values ranging from 0-50% resulted in a 67% drop in the effective thermal conductivity; this is due to the change of angle in the struts and reduction of the volume fraction of structure. These findings indicate that architected cellular materials provide an excellent platform for controlling thermal and mechanical properties and developing multi-functional thermal metamaterials.

# CHAPTER 4

## Programmable Thermal Transport in Shape Memory Polymer Microlattices

### 4.1. Introduction to Shape Memory Polymer Microlattices

Resolving the prime challenge of controlling heat transfer is crucial to meeting the critical problems of energy conversion systems, information processing, and electronic thermal management. However, unlike the advanced programming capabilities of the mechanical [167]–[171], optical [172]–[175], and electrical [176]–[178] systems, the tunability of thermal systems is still remarkably restrained. The advancement of metamaterials has enabled nonlinear and controllable structures, which exceed the physical properties found in nature [179]. Thermal metamaterials with the traditional purpose of heating, cooling, and energy harvesting are emerging with remarkable efficiency and compactness [12]. Engineering the thermal conductivity has led to a unique manipulation of heat flux. At the macroscale level, thermal conductivity anisotropy can be created using thermally conductive and thermally insulating materials [18]·[180]·[181]. In contrast, at the microscale level, the

design of thermal metamaterials relies on engineering the thermal conductivity with coherent phonon transport [182], phononic crystals [183], and local resonances [184]. In addition to conduction, radiative heat transfer has also been engineered to manipulate the heat flux[30]. While nanophotonics has enabled regulating the spectral and spatial characteristics of thermal radiation [24]–[26],[28][185][186], surface coatings have remained a practical candidate for controlling the emissivity over a large surface area [29]. Although certain functionalities like cloaking [22]·[17]·[82]·[187]·[81], rotation [18]·[188], and concentration [189]·[190] can be realized using thermal metamaterials, their conventional design process still lacks programmable thermal properties required for tunable heat flux manipulation purposes.

Architected materials are engineered materials with controlled micro-architectures designed to have physical properties determined by micro-structural geometry rather than the chemical composition. The hierarchical topologies in architected materials have led to unique properties such as ultra-high stiffness [7], ultra-low density [191], and ultrahigh surface-to-volume ratios that introduce a significant radiation contribution [135] in the thermal transport phenomenon. Since the geometrical arrangement of micro-structural elements determines radiation view factors in architected materials, mechanical deformation of architected materials results in a change in radiative thermal transport, potentially leading to a non-negligible shift in the overall thermal properties. Furthermore, when deformed significantly, connectivity among internal micro-structure may be altered, affecting conductive thermal transport in architected materials. This deformation-dependent thermal transport in architected materials opens up new opportunity to create materials with programmable thermal transport when shape-shifting materials are incorporated.

Shape memory polymer (SMP) materials that can actively deform and reconfigure when exposed to external stimuli such as electricity [192], light [193], sound [194], water [195], and heat [196] have been widely studied for their profound potential for adaptive systems. The emerging pathway to create dynamic and adaptive architectures involves 3D printing with such shape-shifting materials. This approach has been recently termed 4D printing, with the 4th dimension being time [197]·[198]. Incorporating SMP into metamaterials design will enable the active and reversible transformation of the 3D spatial arrangement of the microstructural elements, which could lead to the modulation of their effective properties. Therefore, 4D printed metamaterials with inherently reversible deformation[199] and programmable mechanical properties [200]·[201] have an unmatched potential for creating unprecedented adaptive and tunable material systems. Examples of 4D printed SMP-based metamaterials include active composites of SMP fibers in an elastomeric matrix to realize complex three-dimensional configurations [202]·[203], programmable, layered SMP composite for smart folding structures [204], chiral-lattice SMP metamaterials for adjustable Poisson's ratio [205], and multi-material SMP architectures for programmable mechanical grippers [171]. Although the mechanical properties of these SMP metamaterials have been comprehensively investigated in previous works [206]·[205], their thermal properties and capability for programmable thermal transport have received little attention.

## **4.2. Materials and Methods**

SMP microlattices were fabricated in collaborative work at Ruger's University (Dr. Howon Lee's lab) with a high-precision additive manufacturing technique —projection micro-stereolithography (P $\mu$ SL)—. P $\mu$ SL uses digital dynamic photomask to build complex 3D

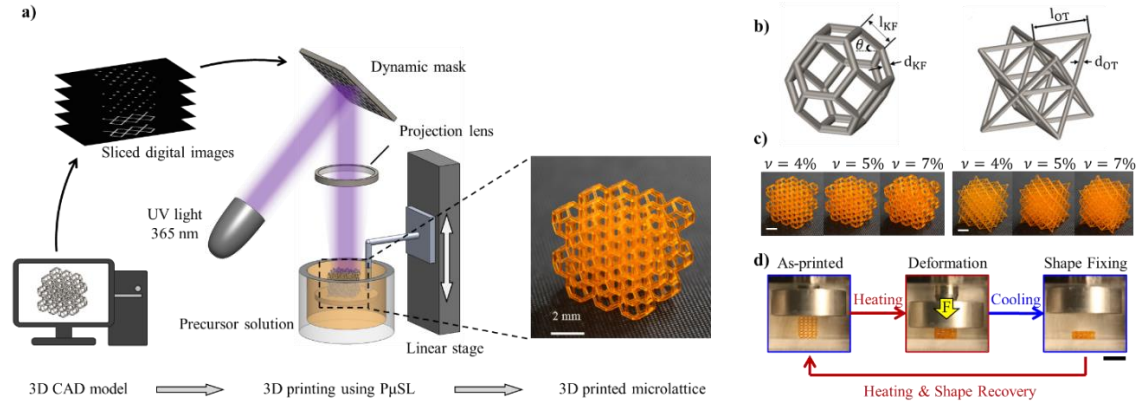
objects in a layer-by-layer fashion rapidly [207]. **Figure 4-1(a)** shows that the 3D computer-aided design (CAD) model of a microlattice is digitally sliced into a series of 2D images. A digital image is displayed on the dynamic mask, followed by the irradiation of a UV light up the mask. Then the light reflected off the mask carries the corresponding image and is focused through a projection lens on the surface of photocurable SMP precursor solution. As a result, a liquid precursor solution is converted into a solid layer with the desired shape. Once a layer is completed, the linear stage moves the sample holder down to solidify the next layer with the following digital image projection. A 3D object is additively built by repeating this process for all the layers. The optical lateral resolution of the system is about 13  $\mu\text{m}$ . In this study, an exposure time of 5 sec was given to cure each layer having a thickness of 50  $\mu\text{m}$ . Two microlattices were fabricated in this study; Kelvin Form (KF) and Octet Truss (OT) microlattices. **Figure 4-1(b)** shows the unit cells for KF and OT microlattice, respectively, and their dimensional parameters. Specifically,  $\theta = 45^\circ$ ,  $l_{\text{KF}} = 1380 \mu\text{m}$ ,  $d_{\text{KF}}$  ranging from 303  $\mu\text{m}$  to 428  $\mu\text{m}$  were used for KF samples, while  $l_{\text{OT}} = 1380 \mu\text{m}$  and  $d_{\text{OT}}$  ranging from 93  $\mu\text{m}$  to 131  $\mu\text{m}$  were used for OT samples (**Table 4-1**). By varying the diameter of struts, samples with volume fractions of 4%, 5%, and 7% for KF and OT were fabricated. Printed samples were rinsed in ethanol for 30 sec 3 times to wash out uncured precursor solution. Then they were allowed to dry in air overnight until the absorbed ethanol was removed, followed by a post-curing in a UV oven for 2 hours.

**Table 4-1** Designed and measured dimensional parameters of the 3D printed microlattices

Sample		Designed Parameters			Measured Parameters
		$l$ ( $\mu\text{m}$ )	$d$ ( $\mu\text{m}$ )	$\nu_{rel}$	$\nu_{rel}$
<b>Octet-truss</b>	OT1	1380	93	3%	4.1%
	OT2	1380	107	4%	5.0%
	OT3	1380	120	5%	6.4%
	OT4	1380	131	6%	7.4%
<b>Kelvin-foam</b>	KF1	1380	303	4%	3.9%
	KF2	1380	338	5%	5.0%
	KF3	1380	400	7%	6.7%

In this chapter, we present programmable thermal transport in architected materials using 4D printed SMP microlattices. We used projection micro-stereolithography (P $\mu$ SL) [207] (**Figure 4-1 (a)**) to additively manufacture SMP octet-truss (OT) and Kelvin foam (KF) architectures (**Figure 4-1 (b)**) that display distinctive stretching-dominated and bending-dominated deformation, respectively [208]·[209]. Effective thermal conductivity of both microlattices in different effective densities (**Figure 4-1 (c)**) was measured at varying temperatures using infrared (IR) thermography. Furthermore, they were mechanically compressed while their thermal conductance was monitored to investigate the change in conductive and radiative thermal transport during compression. Once the SMP microlattices are heated above their glass transition temperature ( $T_g$ ), the material transitions from glass to rubbery state; therefore, they can be easily deformed by applying a compression force, as demonstrated in **Figure 4-1(d)**. By cooling the samples below their  $T_g$ , they reenter the glassy state and retain a fixed shape even after removing the compression force. As a result of reheating the samples above their  $T_g$ , they fully recover and regain their original configuration. Taking advantage of the shape memory effect of the SMP, we also demonstrate

that thermal transport in the 4D printed architected materials can be tailored via mechanical programming and fully restored.

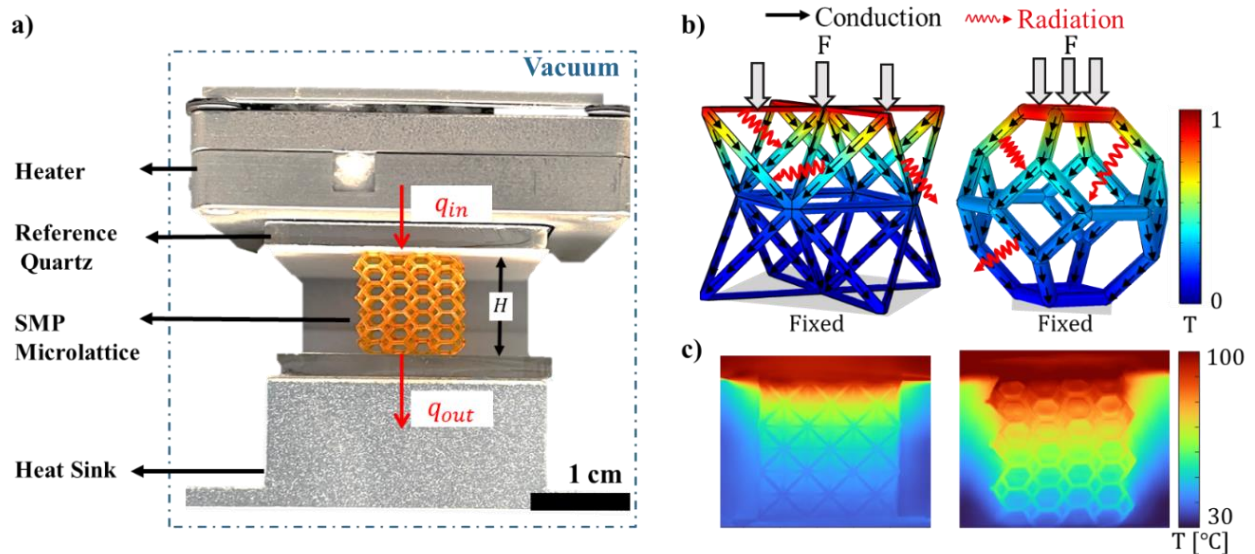


**Figure 4-1** a) 4D printing of SMP microlattices using the P $\mu$ SL technique. b) Schematic of the Kelvin Foam (KF) sample with  $\theta = 45^\circ$ ,  $l_{KF} = 1380 \mu\text{m}$ ,  $d_{KF}$  ranging from  $303 \mu\text{m}$  to  $428 \mu\text{m}$  (Left) plus the Octet Truss (OT) sample with  $l_{OT} = 1380 \mu\text{m}$ , and  $d_{OT}$  ranging from  $93 \mu\text{m}$  to  $131 \mu\text{m}$  (Right). c) 4D printed SMP KF (Left) and OT (Right) samples with corresponding volume fractions of 4%, 5%, and 7%. The scale bar represents 2 mm. Detailed geometrical configurations for all structures can be found in Table S2 of Supplementary Material. d) Shape memory effect of SMP architected materials. Shape programming happens as a result of heating, followed by deformation and cooling. Shape recovery to its original shape occurs upon heating. The scale bar is 1 cm.

For thermal characterization of SMP microlattices, IR thermography [135] was used in conjunction with a vacuum level below  $10^{-4}$  Torr. **Figure 4-2(a)** demonstrates the experimental setup for measuring thermal conductivity and thermal conductance of the SMP microlattices. The samples were located in-between a compressible heat source and an anchored heat sink. Two reference quartz blocks with a known thermal conductivity of  $1.38 \text{ Wm}^{-1}\text{K}^{-1}$  were utilized for calibrating the heat flux entering and leaving the microlattice control volume. The difference between the measured heat flux in the top and bottom reference quartz blocks is correlated with the radiation losses in the system. Therefore, the radiation heat flux can be calculated as  $q_{rad} = q_{in} - q_{out}$ . Emissivity calibration of the SMP microlattices in an isothermal boundary condition resulted in mid-IR emissivity values of



0.94±0.01 and 0.94±0.03 before and after glass transition, respectively. These values are in agreement with the mid-IR emissivity values reported for SMP materials in literature [210]. The calibrated emissivity values were used for temperature measurements of each corresponding sample, as demonstrated in **Figure 4-2(c)**. Therefore, by using the calibrated heat flux and the resultant temperature gradient in the SMP microlattices, the effective thermal conductivity was calculated using Fourier's law ( $\kappa_{eff} = q_{in}H / \Delta T$ ) where  $\Delta T$  is the temperature gradient across the sample, and H is the height of the sample as demonstrated in **Figure 4-2(a)**. The high surface-to-volume ratio of the SMP microlattices (32-45 mm<sup>-1</sup>), in addition to their high IR emissivity (0.94), results in a significant contribution of radiative heat transfer, even near room temperatures. **Figure 4-2(b)** illustrates the conduction contribution of the solid struts and radiation heat transfer among individual struts and their surrounding non-participating media.



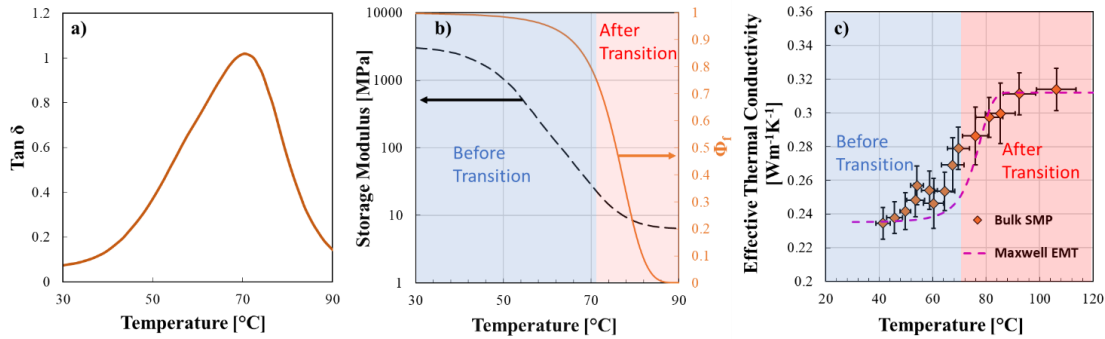
**Figure 4-2** a) We characterize the thermal properties of SMP microlattices and the contribution of both conduction and radiation heat transfer modes using the IR thermography methodology. In response to the low intrinsic thermal conductivity of SMP (0.2-0.3 Wm<sup>-1</sup>K<sup>-1</sup>), high IR emissivity (0.94), and high porosity (>93%) of

these architected materials, radiation contribution is significant in SMP microlattices. b) The primary heat transfer modes—conduction and radiation— in OT and KF SMP microlattices. Tunability of geometry configuration in SMP microlattices results in the programmability of their thermal properties. Therefore, we use mechanical compression for reconfiguring their geometry and monitor their thermal conductance as a function of mechanical strain. c) IR images of the KF (Left) and OT (Right) samples. The IR images contain information on the temperature gradient of each unit cell for calculating the thermal properties of SMP microlattices.

For realizing the role of conduction in the SMP microlattices, a bulk SMP sample was thermally characterized using the IR thermography methodology. Dynamic mechanical analysis (DMA) was done on the bulk SMP specimens with dimensions of 25 mm x 8 mm x 1 mm. A dynamic mechanical analyzer (Q800, TA Instruments) with a tensile loading mode was utilized, and the experiments were conducted with a strain of 0.2 %, frequency of 1 Hz, preload of 0.001 N, and force track of 150 %. Storage modulus, loss modulus, and  $\tan \delta$  were measured as a function of temperature with a temperature increasing rate of  $1 \text{ }^\circ\text{C min}^{-1}$ . The results of  $\tan \delta$  – the ratio of loss to storage modulus—indicate that the bulk SMP has a glass transition temperature of  $71^\circ\text{C}$  (**Figure 4-3 (a)**). In addition, we used the bulk SMP's storage modulus to identify the fraction of “frozen bond” to “active bond” that coexisted in the polymer. The frozen bonds represent the fraction of the C-C bonds with no conformational motion, while the active bonds are correlated with the C-C bonds that undergo free localized conformational motion[211].[212]. Therefore, at the glassy state, the frozen bonds are predominant. We used the approach proposed by Liu *et al.*[213] and identified the volume fraction of frozen bonds as a function of temperature (**Figure 4-3 (b)**) using the equation below:

$$E(T) = \frac{1}{\frac{\phi_f}{E_i} + \frac{1-\phi_f}{3NkT}} \quad (4-1)$$

Where  $\phi_f$  is the fraction of frozen bonds,  $E_i$  is the modulus of internal energetic deformation,  $N$  is the cross-link density,  $k$  is Boltzmann's constant ( $k = 1.38 \times 10^{-23}$  Nm/K), and  $T$  is the temperature. Applying the measured thermal conductivity data at glassy and rubbery states in conjunction with the Maxwell effective medium theory [42], we could explain the transition behavior in the intrinsic thermal conductivity of the bulk SMP sample ( **Figure 4-3(c)**).



**Figure 4-3** a)  $\text{Tan}\delta$  of 3D printed SMP. b) Measured storage modulus of the bulk SMP using dynamic mechanical analysis (DMA) and the derived volume fraction of the frozen bonds as a function of temperature on the secondary axis. c) Measured thermal conductivity of bulk SMP and the applied Maxwell effective medium theory model for explaining the transition behavior in the thermal conductivity of the bulk SMP material.

The effective thermal conductivity of the SMP microlattices is a combination of conduction ( $\kappa_{cond}$ ) and radiation ( $\kappa_{rad}$ ) heat transfer contributions, i.e.,  $\kappa_{eff} = \kappa_{cond} + \kappa_{rad}$ . Convection is negligible if the unit cell sizes are below 10 mm, even in the case of low-conducting polymer foams [38]. Additionally, by providing a vacuum environment, the convection contribution was eliminated in all thermal measurements.

Ashby[159] proposed that the conduction contribution in a connected network of struts should incorporate the thermal properties of the constituent material, the topology of the unit cell, and the volume fraction of the structure. Therefore, the effective thermal conductivity of cellular solids inside the vacuum environment can be described as  $k_c = A \cdot \bar{\rho} \cdot k_{sol}$ , where  $A$

is the geometrical factor,  $\bar{\rho}$  is the volume fraction of the solid (also known as the relative density of the architected material), and  $k_{sol}$  is the intrinsic thermal conductivity of the constituent solid. The geometrical factor is the fraction of struts aligned with the heat flux direction derived from finite element analysis. The volume fraction of the samples is calculated using the dimensions provided in the CAD model, and the solid thermal conductivity is utilized using the analytical prediction of the bulk SMP. The first order of the volume fraction and the conduction contribution in the effective thermal conductivity have been identified in **Table 4-2** for both OT and KF structures using the illustrated parameters in **Figure 4-1 (b)**.

**Table 4-2** Volume fraction and conduction contribution correlations utilized for the OT and KF lattice structures.

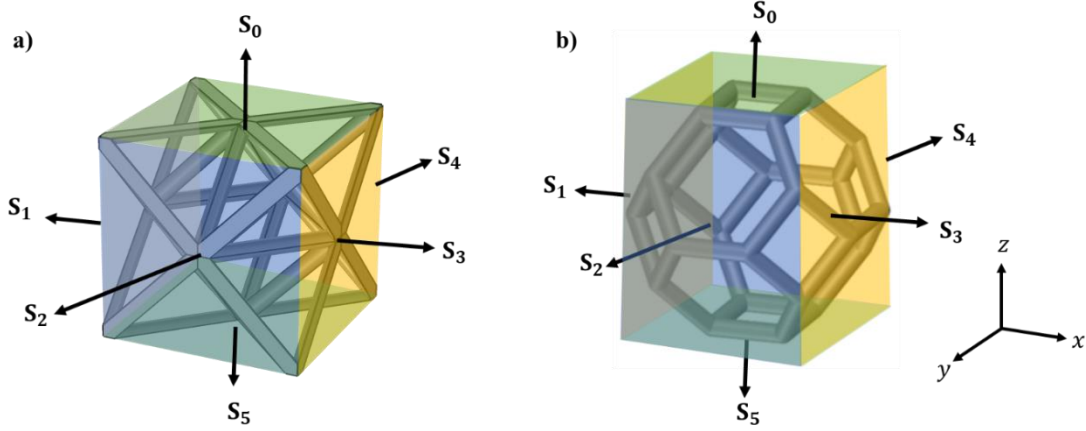
	<b>Octet Truss</b>	<b>Kelvin Foam</b>
Volume Fraction ( $\nu$ )	$\frac{3\sqrt{2}}{2} \pi \left(\frac{d_{OT}}{l_{OT}}\right)^2$	$\frac{3\sqrt{2}}{8} \pi \left(\frac{d_{KF}}{l_{KF}}\right)^2$
Conduction Contribution ( $\kappa_{cond}$ )	$\frac{1}{3} \bar{\rho}_{OT} \kappa_{solid}$	$\frac{6}{25} \bar{\rho}_{KF} \kappa_{solid}$

The volume fraction of the printed samples was measured using mass divided by the total volume of the microlattice. Mass of each printed structure was obtained using a digital scale (ML303E, Mettler Toledo), while volume was obtained by measuring each sample's length, width, and height. The bulk density of the SMP was measured  $\rho_{Bulk} = 1254 \text{ kg/m}^3$  from a 3D printed solid cylinder with a diameter of 10 mm and a height of 10 mm[200].

The major challenge in predicting radiation contribution in architected materials arises from their complex architecture and the inherent complexity associated with their transport mechanism. Different methods to determine the radiative properties of highly porous materials have been investigated in literature [214]·[215]. Simplifying the studied geometry [161]·[63] and using the ray-tracing Monte Carlo method [216]·[217]·[68] have been extensively explored in the literature for addressing the contribution from view factors in radiative conductivity. However, simplifying the geometrical structure underestimating the radiation contribution and Monte Carlo simulations in architected structures require a substantial computational effort.

In the current study, the theoretical radiative conductivity approach for cellular materials proposed by Zhao *et al.* [161] has been adapted to develop a new model based on a more realistic representation of Kelvin foam and octet lattice structures. In this attempt, the microstructure of the lattice structures has been taken into account. Therefore, the radiation view factor of the struts has been calculated based on their spatial configuration. The radiative conductivity is calculated based on the radiation heat flux as a function of the view factors, radiosity, calibrated emissivity, volume fraction, and temperature. To calculate the radiative conductivity ( $k_{rad}$ ), the radiative heat flux must be solved ( $q_{rad}''$ ). The total heat flux will be the summation of conduction and radiation contributions:

$$q_{net}'' = q_{cond}'' + q_{rad}'' = -k_{eff}dT/dy \quad \mathbf{(4-2)}$$



**Figure 4-4** Lattice structure model applied for radiative conductivity and notations a) Octet truss and b) Kelvin foam lattice. The heat flow is parallel to the z-direction.

where  $q_{rad}$  comprises of reflection and emission contributions. As a result, the total irradiation ( $Q_{rad}$ ) will be examined in the z-direction at first as follows:

$$Q_{rad,z} = (Q_{rad,z})_{emission} + (Q_{rad,z})_{reflection} \quad \mathbf{4-3(a)}$$

$$(Q_{rad,z})_{emission} = \sum_{i=1}^N A_i F_{iS_0} \epsilon \sigma T^4 + \sum_{n=S_1}^{S_5} J_n F_{nS_0} A_n \quad \mathbf{(b)}$$

$$(Q_{rad,z})_{reflection} = \sum_{n=S_1}^{S_5} \sum_{i=1}^{36} (J_n F_{ni} A_n) R F_{iS_0} + \sum_{i=1}^{36} \sum_{j=1, j \neq i}^{36} \epsilon A_i F_{ij} \sigma T^4 R F_{iS_0} \quad \mathbf{(c)}$$

In the equations above,  $\sigma = 5.669 \times 10^{-8} W m^{-2} K^{-4}$  is the Stefan-Boltzmann constant,  $R = 1 - \epsilon$  is the solid reflectivity,  $A_i$  is the solid surface of the  $i$ th strut ( $i = 1, 2, \dots, 36$ ) within a unit cell,  $J_n$  and  $A_n$  are the irradiation and surface area of the void surfaces ( $n = S_1 - S_5$ ),  $F_{iS_0}$  is the configuration factor from the  $i$ th strut to surface  $S_0$ ,  $F_{nS_0}$  is the configuration factor from the  $n$ th surface to surface, while  $F_{ni}$  is the configuration factor from the  $n$ th surface to the  $i$ th strut surface.  $F_{ij}$  is the configuration factor between struts, and all view factors are derived based on their angular position towards each other and void surfaces (**Appendix A**). The total

irradiation in both x and y directions follow the same approach; therefore, the radiative conductivity is calculated as below:

$$k_{rad} = q_{rad}'' \cdot H / [(T_h - T_c)] \quad (4-4)$$

As a result, the effective thermal conductivity is a summation of the conduction and radiation contribution.

$$k_{eff} = k_{cond} + k_{rad} \quad (4-5)$$

$k_{rad}$  can be calculated based on the approach proposed by Zhao *et al.* [159] by calculating the radiation heat flux, which is a function of the view factors, radiosity, calibrated emissivity, volume fraction, and temperature. Details of the view factor derivation can be found in **Appendix A**.

### 4.3. Results and Discussion

#### 4.3.1. Temperature-Dependent Thermal Conductivity of SMP Microlattices

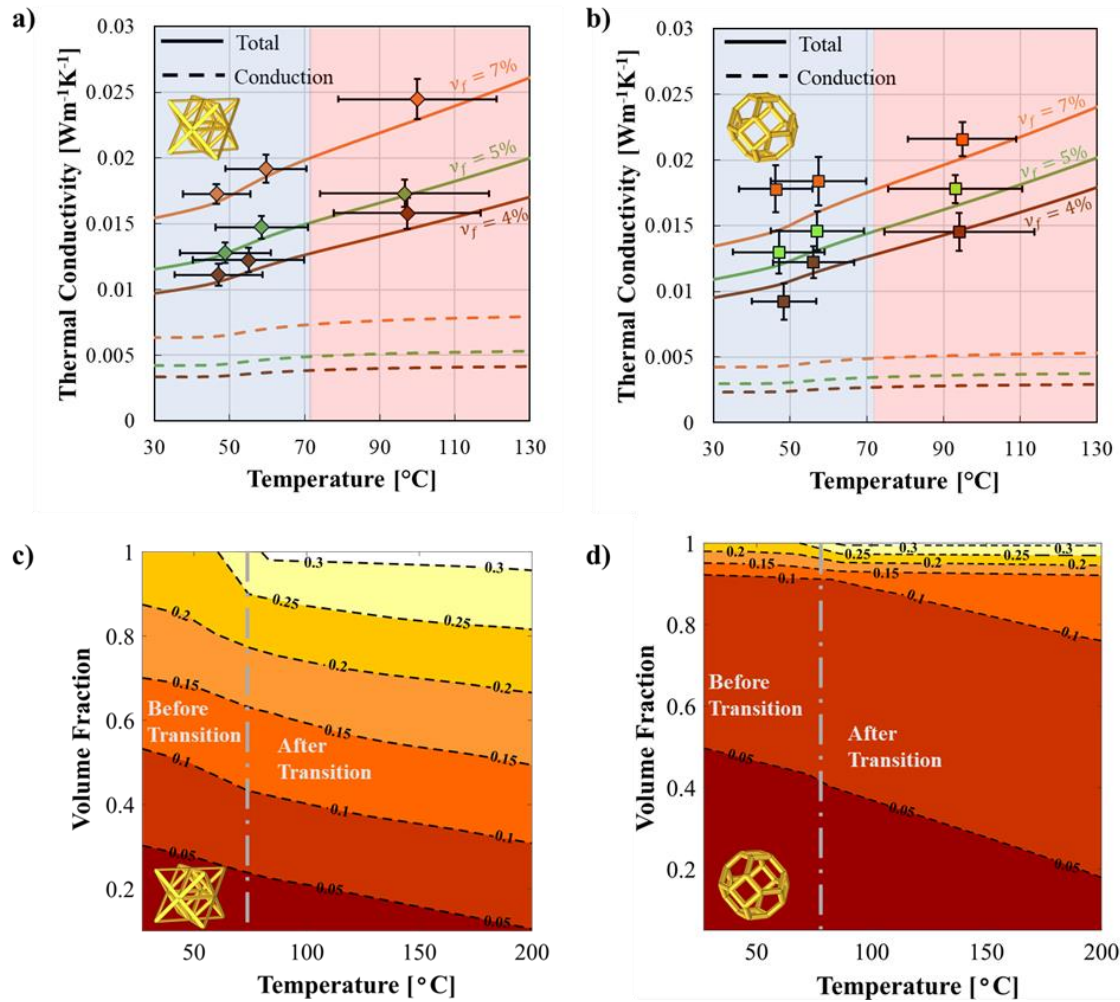
Due to the insulating nature of these low density architected materials, we used the temperature gradient data of the first row of unit cells in each corresponding lattice structure for thermal conductivity measurements. **Figure 4-5(a)** and **Figure 4-5(b)** illustrate the effective thermal conductivity of KF and OT structures, respectively. In both lattice structures, the conduction contribution increases with solid volume fraction as predicted by our analytical modeling (shown by the dashed lines). The increase in conduction contribution as a function of temperature is due to the glass transition of the intrinsic SMP. The radiation contribution increases significantly with temperature because both emission and reflection are highly dependent on temperature. The analytical model predicts that the thermal

radiation contribution to heat transfer across KF cells ranges from 68 to 83% and across OT cells ranges from 59 to 76% over a temperature range of 30 to 130 °C. Due to the non-negligible contribution of radiation heat transfer in low-density microlattices, the overall effective thermal conductivity of both OT and KF, therefore, increases significantly with temperature. The solid lines represent the effective thermal conductivity predicted by analytical modeling, and the linear slope is derived by the surface emissivity and the surface-to-volume ratio of the lattice structures.

The OT structures show a slightly higher effective thermal conductivity ( $\sim 0.002 \text{ Wm}^{-1}\text{K}^{-1}$ ) than their KF counterparts with identical volume fractions. This phenomenon results from a higher geometrical factor in OT (0.35) than KF (0.24). The geometrical factors are based on the contribution of the parallel struts to the heat transfer direction from finite element modeling (FEM) analysis. The analytical modeling was utilized for creating a contour plot of the effective thermal conductivity as a function of volume fraction and temperature for both OT (**Figure 4-5 (c)**) and KF (**Figure 4-5 (d)**) lattice designs. The contour plots represent a design space for the effective thermal conductivity of OT and KF structures, where the dashed lines illustrate the constant thermal conductivity values, and the shaded regions are all thermal conductivity values that come in-between the lines. As shown, the slope of the constant thermal conductivity lines changes after transition for both lattice structures due to glass transition in the SMP material. By increasing the temperature at a constant volume fraction, the increase in the effective thermal conductivity is exhibited due to a higher radiation contribution. However, by increasing the volume fraction at a constant temperature, the contribution of radiation heat transfer mode significantly decreases, and conduction takes over as the primary heat transfer mode. At the volume fraction value of 1,



the thermal conductivity of both designs converges to the intrinsic thermal conductivity of the bulk SMP, and the radiation contribution reaches zero. By increasing the volume fraction in **Figure 4-5 (c)** and **(d)**, the OT lattice design demonstrates a higher effective thermal conductivity compared to the KF lattice due to a higher geometrical factor. For instance, at 50 °C and a volume fraction of 0.4, the OT design results in thermal conductivity of  $\sim 0.07 \text{ Wm}^{-1}\text{K}^{-1}$ , and on an isothermal line, this value increases to  $\sim 0.2 \text{ Wm}^{-1}\text{K}^{-1}$  at 0.8 volume fraction. Conversely, its counterpart KF design demonstrates a thermal conductivity of  $\sim 0.04 \text{ Wm}^{-1}\text{K}^{-1}$  at 50 °C and 0.4 volume fraction, and its thermal conductivity only increases up to  $\sim 0.085 \text{ Wm}^{-1}\text{K}^{-1}$  while moving on an isothermal line to 0.8 volume fraction.

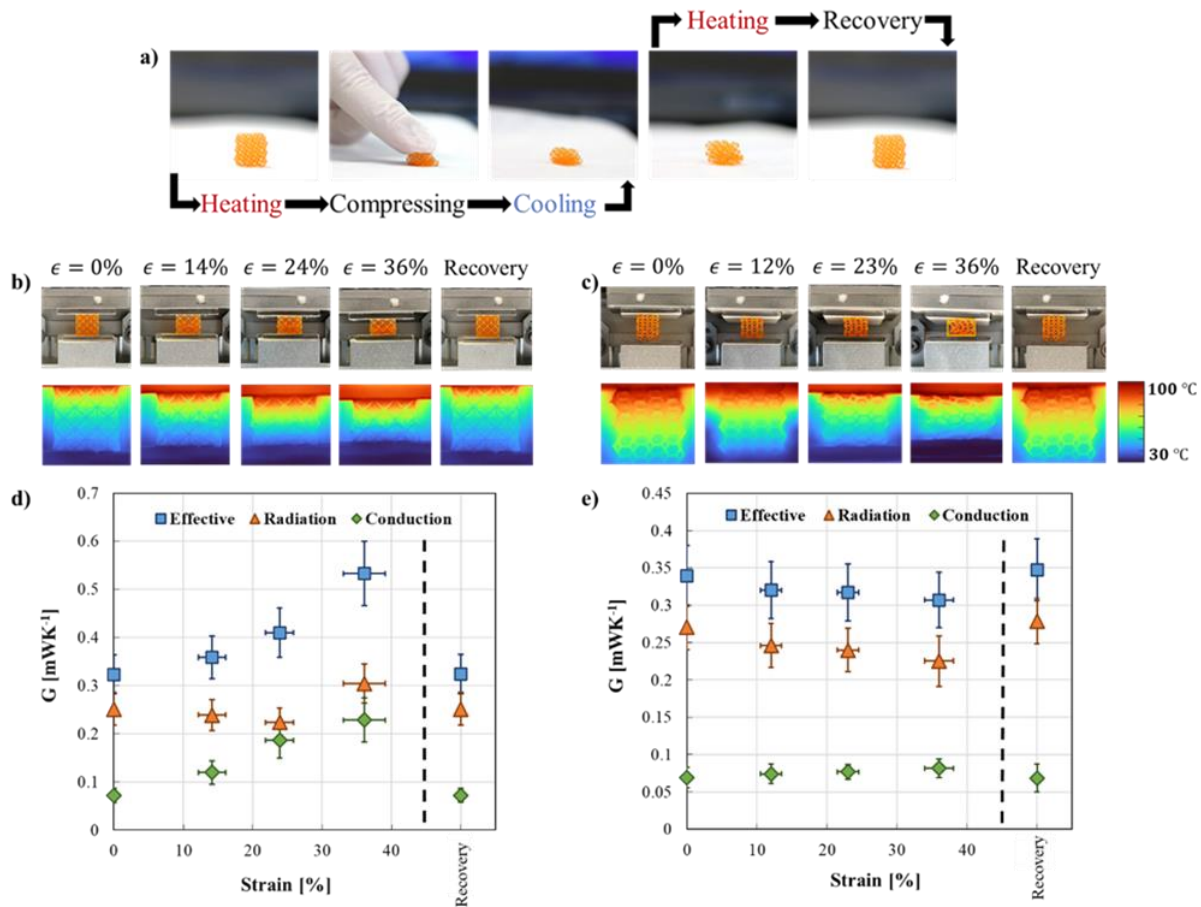


**Figure 4-5** a) Measured thermal conductivity of OT samples, and b) KF samples with 4%-7% volume fraction ratios. The dotted and solid lines represent the analytical predictions for the conduction contribution and radiation contribution, respectively. The increase in the conduction contribution is attributed to the changes in the intrinsic thermal conductivity of bulk SMP as a function of temperature. The increase in the radiation contribution results from increasing the temperature in both samples following the Stefan-Boltzmann law. c) Contour plot of the effective thermal conductivity as a function of volume fraction and temperature for c) OT and d) KF samples. The dashed lines represent the constant thermal conductivity values, while the shaded regions are all thermal conductivity values in-between the dashed lines. By increasing the volume fraction, the radiation contribution in both samples decreases to reach the value of zero when the effective thermal conductivity converges to the intrinsic thermal conductivity of bulk SMP at the volume fraction of 1.

### 4.3.2. Programmable Thermal Conductance of SMP Microlattices

The unique ability of geometrical re-programming and full-shape recovery of the SMP can be utilized to tweak the effective thermal properties of the 4D printed microlattices. As a result of heating the SMP microlattices above their glass transition temperature, they enter the rubbery state, and their thermal conductance can be tuned by mechanical deformation. This programmed thermal conductance can be retained even after removing the mechanical stress below the glass transition temperature and be restored upon geometrical recovery (**Figure 4-6(a)**). Deformation-induced geometrical reconfiguration of the lattice causes radiation view factors of the struts in the lattice to change, resulting in modulation of the radiation contribution. Therefore, the significant radiation contribution in low density architected materials enables a new strategy to manipulate thermal transport. Deformation of OT is stretching-dominated, where micro-struts bear the load primarily through tension and compression[208], whereas KF is bending-dominated where the micro-struts bear load via bending[209]. Since they display specific deformation behaviors during compression, different heat transfer mechanisms drive overall thermal transport changes during shape change. To demonstrate this concept, we measured the effective thermal conductance ( $G_{eff} = q_{in}/\Delta T$ ) of OT and KF with a 5% volume fraction while applying mechanical compression up to 36% compression strain at 105 °C heater temperature. The strain is defined as the ratio of height reduction in the sample over the initial height (i.e., engineering strain). Then, the compression force was removed, and the lattices fully recovered the initial geometry. **Figure 4-6(b)** and **Figure 4-6(c)** show the compression cycles in addition to the corresponding IR image for each strain for the OT and KF samples, respectively. The effective thermal conductance was measured across the samples along with decoupling the role of conduction

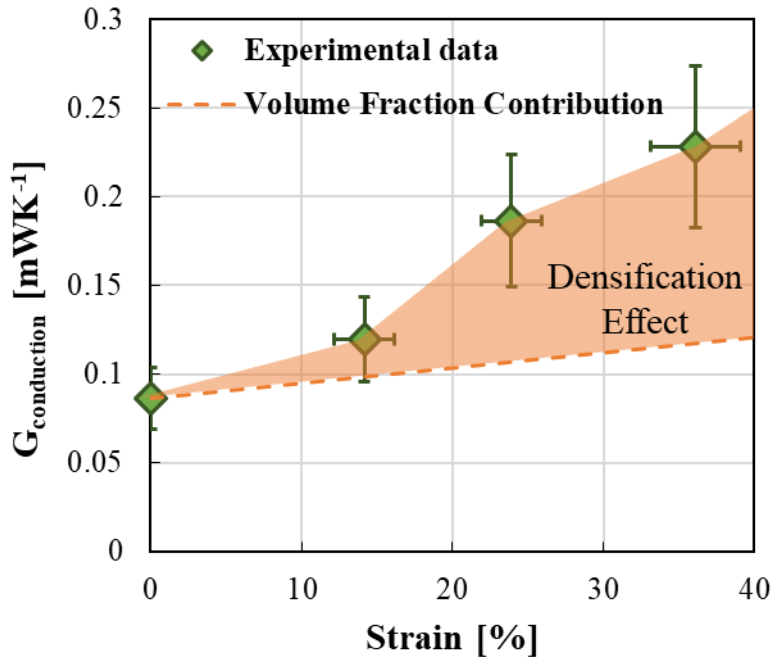
( $G_{cond} = q_{out} / \Delta T$ ) and radiation ( $G_{rad} = G_{eff} - G_{cond}$ ). **Figure 4-6 (d)** and **Figure 4-6(e)** show the measurement results of the thermal conductance and the contribution of conduction and radiation heat transfer modes in the OT and KF samples, respectively. The recovery data point corresponds to the thermal conductance measurements after complete shape recovery.



**Figure 4-6** a) By heating the SMP microlattices above their glass transition and applying an external compression, their thermal conductance can be tuned and retain the programmed value even after removing the compression at below glass transition temperatures. As a result of heating the microlattices above their glass transition, they recover to their initial configuration; therefore, their thermal conductance restores. Programmable thermal conductance in the b) OT and c) KF samples with an initial 5% volume fraction up to 36% strain. The IR images correspond to each strain cycle for deriving the conductance information. d) The measured conductance values for the OT sample illustrate that by increasing the volume fraction and strut

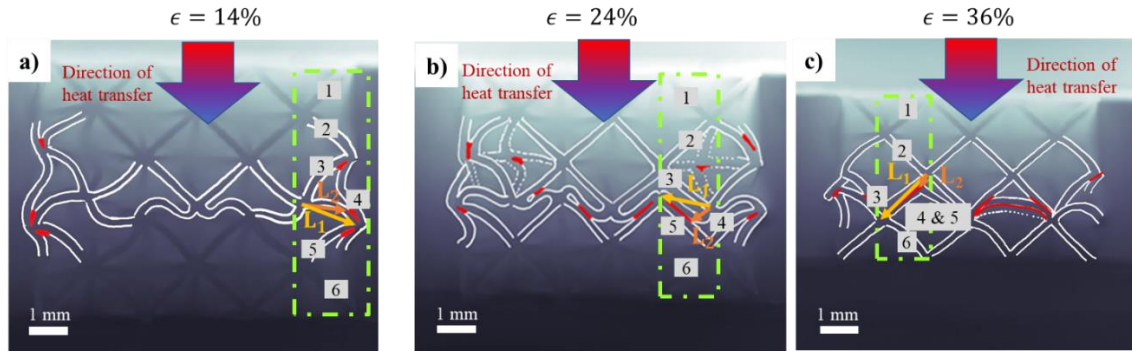
densification, the effective thermal conductance increases by compression. Therefore, increasing the thermal conductance of OT lattices is attributed to conduction contribution. e) The measured conductance values for the KF sample demonstrate no strut densification while decreasing the view factors (i.e., radiation contribution) causes the decreasing trend in the effective thermal conductance. Therefore, decreasing the thermal conductance of KF lattices is attributed to radiation contribution.

As a result of compressing the OT sample, the effective thermal conductance increases by 66 % (**Figure 4-6 (d)**). This increasing trend can be attributed to a significant increase of 156% in the conduction contribution. By compressing the OT lattice from 0% to 36%, the volume fraction of the sample increases from 0.050 to 0.067. More importantly, due to the Euler buckling of the micro-struts and the collapse of the unit cells, this compression cycle creates localized strut densification, which reduces the thermal transport length from junction-to-junction for the conduction heat transfer mode. Densification of struts was observed in some unit cells, even at small compression cycles. The numerical analysis cannot easily capture this phenomenon; therefore, we identified the expected changes from the volume fraction contribution on the experimental results, while the rest can be attributed to the densification effect. **Figure 4-7** demonstrates the conduction contribution in thermal conductance as a function of engineering strain. The dotted line is the predicted volume fraction contribution using our analytical model, and the orange domain illustrates the difference between the measured and calculated conductance, which is attributed to the local densification effect. Compressing the OT sample results in the creation of new contact points in addition to the original junctions in the lattice structure that reduces the thermal resistance from the heat source to the heat sink in the OT medium.



**Figure 4-7** Impact of volume fraction increase vs. strut densification effect to the sharp rise of conduction contribution in thermal conductance of the OT sample with 5% initial volume fraction.

In particular, decreasing the thermal transport length from junction-to-junction reduces the overall thermal resistance and increases the conduction contribution of thermal conductance. For demonstrating this concept, close-up images of the compression cycles of the octet lattice were carefully studied. **Figure 4-8** illustrates the compressed OT structure at different strains, and the front layout of the struts viewing the camera has been highlighted in white. The red lines identify the contact points between the struts while they experience densification. The highlighted column in the dotted line indicates the previous junction-to-junction distance ( $L_1$ ), and the new junction-to-junction length is shown as ( $L_2$ ).



**Figure 4-8** Close-up images of the compressed OT lattice with 0.05 volume fraction at a) 14%, b) 24%, and c) 36% strain. The strut borders of the beams viewing the camera have been highlighted in white, and the contact points resulting from densification have been shown in red—the local strut densification results in a decrease in thermal transport length from one junction to another.

**Table 4-3** demonstrates the  $L_2$  values at different strains with  $L_2=L_1$  when strain is equal to zero. Estimating the changes applied to thermal resistance is a reasonable guideline for addressing the expected increase in thermal conductance due to densification. We used the first-order thermal resistance circuit calculations to quantify the densification impact. For example, for 36% strain, by calculating the thermal resistance of single struts with  $L_1$  and  $L_2$  heat transfer lengths, we have  $R_1 = \frac{L_1}{\kappa A} = 4.07 \text{ K/mW}$  and  $R_2 = \frac{L_2}{\kappa A} = 0.43 \text{ K/mW}$ . As demonstrated in **Figure 4-8**, with struts #3-5 coming to contact from 6 struts in a series configuration, the reduction in thermal resistance of single struts translates into about a 45% decrease in the overall thermal resistance. Therefore, the corresponding value from the thermal resistance reduction can be used to justify the estimated increase in the conduction contribution of thermal conductance (48.6% increase) as a result of densification.

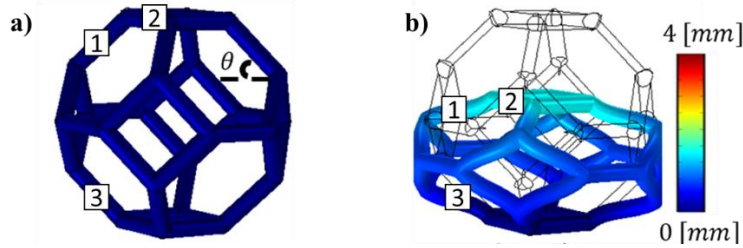
**Table 4-3** Change in the volume fraction ( $\nu$ ) and strut densification contributions in transferring the heat through conduction at different strains. The reducing value of  $L_2$  as a function of strain indicates the decrease in the thermal resistance or the increase in thermal conductance due to strut densification.

Strain [%]	$\nu$ [%]	$\nu$ Contribution [%]	Strut Densification Contribution [%]	$L_2$ [mm]
0	0.05	100	0	1.340
14	0.0565	82.3	17.7	1.060
24	0.0612	57.3	42.7	0.335
36	0.0674	51.4	48.6	0.146

As a result of compressing the KF sample, the effective thermal conductance decreases by 15% (**Figure 4-6 (e)**). This reduction can be attributed to a decreasing trend of the radiation contribution by 24%. In particular, the equivalent view factors decrease with adjacent struts moving further apart. Analytical calculations for compressing a single unit cell demonstrate how increasing the strain has an adverse impact on the radiation contribution. By compressing the KF lattice up to 36% strain, the volume fraction increases from 0.050 to 0.071. Therefore, the contribution of conductance slightly increases as a result of increasing the volume fraction. A similar trend can be observed in the measured data throughout the entire sample. **Figure 4-9** demonstrates the numerical results for the deformation of a single unit cell at 0% (**Figure 4-9 (a)**) and 36% (**Figure 4-9 (b)**). As illustrated, by increasing the strain, the angle between the adjacent struts increases (i.e., struts 1 and 2) while mirrored struts (i.e., struts 1 and 3) view each other at a closer distance. However, the view factor calculation for these highlighted struts demonstrates that the view factor gain between struts 1 and 3 is  $\sim 4$  times smaller than the view factor loss between struts 1 and 2 due to



compressing the unit cells. In all view factor calculations, the struts have been assumed as perfect cylindrical bars, and the analysis is valid for all struts with identical  $F_{12}$  and  $F_{13}$ .

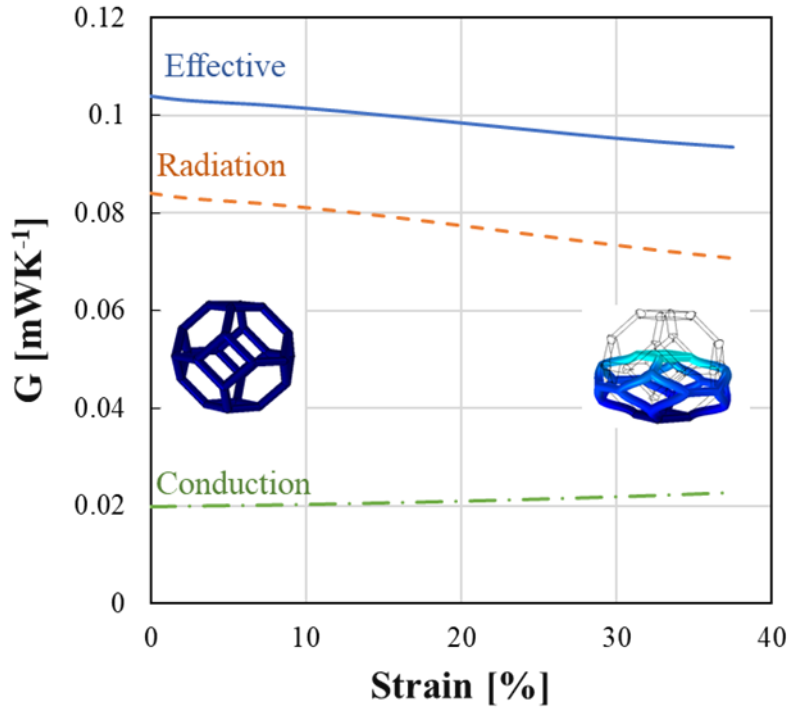


**Figure 4-9** Mechanical deformations of a single kelvin foam unit cell at a) 0% strain and b) 36% strain. The color bar demonstrates the amount of deformation in mm.

**Figure 4-10** demonstrates the analytical prediction for a single KF unit cell as a function of engineering strain. As a result of increasing strain from 0% to 36%, the volume fraction increases from 0.05 to 0.071; therefore, the conduction contribution increases. However, due to decreasing contribution from the view factor calculations, the radiation contribution reduces by 17%.

**Table 4-4** Mechanical deformations of a single kelvin foam unit cell at a) 0% strain and b) 36% strain. The color bar demonstrates the amount of deformation in mm.

Strain	0%	36%
$F_{12}$	0.08	0.0006
$F_{13}$	0.006	0.027



**Figure 4-10** Analytical calculation of thermal conductance in a compressed KF unit cell up to 36% strain. The conduction contribution increases due to increasing the volume fraction, while the radiation contribution decreases due to a reduced accumulative contribution from the strut view factors.

#### 4.4. Conclusions

Additively manufactured architected materials have opened up a new avenue to create novel physical properties in material systems by allowing facile access to previously unattainable topological designs. Among various physical domains being explored, manipulation of thermal properties is attracting growing attention for better performance and energy efficiency in many engineering areas, including electronics and energy storage systems and the automotive and aerospace industry. This study presents a novel strategy to achieve programmable thermal transport in architected materials by employing the 4D printing approach. We investigated geometry- and deformation-dependent thermal transport in architected materials fabricated with a shape memory polymer via projection micro-

stereolithography (PμSL). We also developed an analytical model to decouple conduction and radiation contributions for the investigated geometries. The analytical predictions demonstrated that above 60% of the effective conductivity in both KF and OT samples is due to radiation. Combined with low intrinsic thermal conductivity and high surface emissivity, SMP microlattice geometries with an inherently high surface-to-volume ratio create unique thermal transport mechanisms in architected materials dominated by radiative heat transfer even at low temperatures.

At lower density regimes, radiative thermal transport becomes more significant, and, therefore, the geometrical configuration of the micro-struts becomes more critical in determining overall thermal transport in architected materials. Consequently, mechanical deformation of the architected materials would result in a significant change in the overall heat transfer, which offers a new opportunity to achieve programmable thermal transport with the 4D printing approach. The programmability of thermal conductance through reconfiguring the spatial arrangements of the struts in the KF and OT samples was examined with a 5% volume fraction by applying mechanical compression. Interestingly, OT and KF showed different trends in thermal conductance change during compression tests. Our experimental and theoretical analyses revealed that thermal transport in the bending-dominated microlattice (KF) was suppressed by decreased radiation contribution. In contrast, thermal transport during the deformation of the stretching-dominated microlattice (OT) is enhanced by increased conduction contribution due to decreased junction-to-junction thermal transport length during Euler buckling.

Moreover, taking advantage of the shape memory effect of the SMP, we demonstrated that thermal transport in the 4D printed architected materials can be tailored via shape programming and recovery on demand. These results suggest that more drastic changes to overall thermal transport are attainable if the design of architected materials is optimized to align the direction of changes to conduction and radiation contributions as a function of strut reconfiguration. These findings provide a new understanding of thermal transport in shape-programmable architected materials and may guide designs of future architected materials, dynamic or adaptive thermal control devices, and building blocks of thermal information processing systems.

# CHAPTER 5

## Nanoscale Carbon-based Thermal Metamaterials

### 5.1. Introduction to Thermal Properties of Glassy Carbon Metamaterials

Aerospace vehicles operate in extreme conditions requiring constituent materials to meet stringent constraints, such as withstanding large mechanical loads and sudden impacts while shielding the body from high or low environmental temperatures. However, the coupling between thermal and mechanical properties creates a challenge for synthesizing lightweight thermally insulating and mechanically resilient materials.

The unique ability of architected materials for tunable architecture and structural parameters results in decoupling their mechanical and thermal properties, making them a promising candidate for ultralight [191] and thermally insulating systems [54]. At the nanoscale, new properties emerge as a result of the size effect with structures that possess remarkable mechanical properties, including ultrahigh stiffness [218] and high effective

strength up to 1 GPa [143][219][220]. While the unique mechanical properties of architected nanolattices have been actively investigated in the recent literature [143]-[221], the associated thermal properties or their capabilities of manipulating heat flows have received little attention. However, the thermal advantages of the proposed architected nanolattices are clear for two main reasons. First, heat transfer is mainly confined to the conduction of heat flux within a small volume fraction of the complex network of solid struts and walls, exclusive for each specific geometry. This geometric effect— also valid for macroscale— takes advantage of the porosity of the architecture and the low thermal conductivity of gases which allows architected materials to achieve a tunable range of effective thermal conductivity values [222]-[135]. Second, the intrinsic thermal conductivity of nano-struts can further be modified due to increased contributions of heat-carrier scattering events with boundaries and microscopic heterogeneities [53].[49].

Moreover, the size effect becomes more appreciable when the characteristic length scale of materials such as the film thickness or the grain size becomes smaller than the phonon mean free path [51].[50]. Therefore, the proposed nanolattice structures can offer extremely low thermal conductivity without sacrificing mechanical properties [147]. This combination of high specific strength and low thermal conductivity is not achievable by conventional materials due to the coupling behavior of thermal and mechanical properties. However, nanolattice materials, due to their architecture and nanoscale feature size, can potentially break the coupling between the physical properties of their constituent material and colonize a new category in the material property space.

The exceptional properties of the nanolattices have been a key driving force for the advancement of high-precision additive manufacturing techniques over the past few decades. Evolution of techniques such as self-propagating photopolymer waveguides (SPPW) [191], direct laser writing (DLW) [35], and projection-micro stereolithography [139] have resulted in the progressive fabrication of lattice structures with unit cell dimensions below  $1\mu\text{m}$ . Two-photon polymerization direct laser writing of the structures made from the ultra-violet cured polymers followed by pyrolysis of these polymeric structures allows the fabrication of structurally robust carbon-based nanolattices. This two-step fabrication method enables the production of lattice structures with exquisite feature sizes (20-200 nm) that are achieved by up to 80% polymer shrinkage during pyrolysis. At the same time, this process allows the realization of complex three-dimensional (3D) geometries that are difficult to fabricate with conventional subtractive methods, enabling an enormous design space. Furthermore, we exploit unique size effects in thermal conductivity by simultaneously optimizing the lattice topology and the pyrolytic carbon nanostructure, as demonstrated for mechanical strength [143]. Our objective is to establish fundamental understanding of thermal transport phenomena in carbon lattice structures of varying dimensions that can be engineered to exhibit unique thermal properties.

## **5.2.Theoretical Approaches**

### **5.2.1. Phonon Transport Modeling of Carbon Nanostructures**

While theoretical studies of nanoscale thermal transport have exploited various models, the semi-classical Boltzmann Transport Equation (BTE) model [52] using the relaxation time approximation and full phonon spectral dependencies have adequately captured the thermal

conductivity size dependencies in semiconductor nanostructures. Thus, the thermal conductivity can be expressed as:

$$\kappa = 1/3 \sum_n \int C(\omega) v(\omega)^2 \tau(\omega) d\omega \quad \text{(5-1)}$$

where  $n$  is the phonon mode polarization,  $C$  is the volumetric phonon heat capacity,  $v$  is the phonon group velocity,  $\tau$  is the phonon relaxation time, and  $\omega$  is the phonon frequency. While the heat capacity and the group velocity are based on dispersion relations, the relaxation time accounts for multiple scattering events, which can be expressed via Matthiessen's rule:

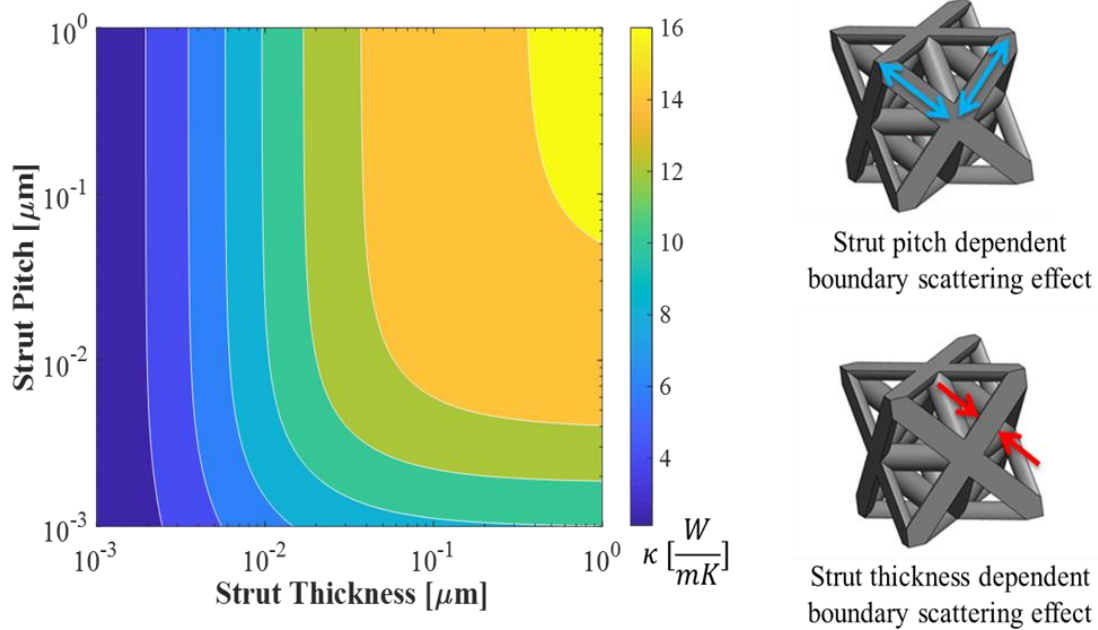
$$\tau^{-1} = \tau_B^{-1} + \tau_D^{-1} + \tau_U^{-1} \quad \text{(5-2)}$$

where  $\tau_B$  is due to boundary scattering,  $\tau_D$  is due to defect scattering, and  $\tau_U$  is due to Umklapp scattering. The Umklapp scattering is described by  $\tau_U^{-1} = AT\omega^2 \exp(-C/T)$ , where  $A$  and  $B$  are fitting parameters to reproduce the bulk thermal conductivity [52]. The defect scattering is described by  $\tau_D^{-1} = C\omega^4$ , where  $C$  is another fitting parameter. The boundary scattering is described by  $\tau_B^{-1} = v/d \times (1-p)/(1+p)$ , where  $d$  is the characteristic length scale and  $p$  is the specular coefficient, which represents the probability of specular phonon reflection from the boundary ( $0 \leq p \leq 1$ ) as described by the Ziman's theory [223]. Using the solutions of BTE, we can identify important phonon transport length scales to guide the sample designs (**Figure 5-1**). Our goal is to investigate the possibilities of ultimate thermal insulation by maximizing the boundary scattering by exploiting spectral phonon properties. The thermal investigations will provide relevant information to the thermal management of advanced semiconductor systems and their efficiency, performance, and reliability. Architected nanolattices will enable studying size effects induced by the thickness and pitch scaling (**Figure 5-1**). Metamaterials are expected to show novel thermal transport mechanisms, including phonon boundary scattering, backscattering, coherence, and confinement effects [48] due to their architecture.

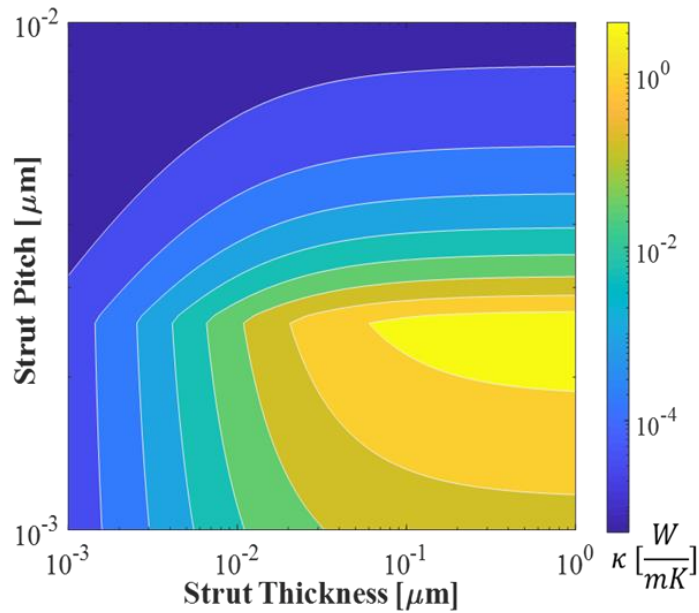


Assuming phonon boundary scattering with completely diffuse boundaries and using bulk dispersion relations in the framework of BTE, contours of constant thermal conductivity lines can be generated and provide the design space of metamaterials. **Figure 5-1** shows the contour plot of carbon lattice structures as the thickness ( $t$ ) or the pitch ( $p$ ) scales, depending on the phonon mean free path ( $\Lambda$ ), the thickness scaling modulates phonon transport from a diffusive ( $t$  or  $p > \Lambda$ ) to a ballistic transport regime ( $t$  or  $p < \Lambda$ ). Ultimately, scaling both the thickness and the pitch will lead to ultrathin nanolattices, with significant reductions in the thermal conductivity. The role of porosity in conjunction with the size effect result in further reduction of the thermal conductivity. Assuming an octet cell lattice for modeling the effective thermal conductivity, we incorporated the volume fraction using  $\bar{\rho} = 6\sqrt{2}\pi \left(\frac{t}{2p}\right)^2$ .

**Figure 5-2** demonstrates the role of porosity provided by the architecture in the effective thermal conductivity of the lattice structure ( $\kappa_{eff} = \frac{\bar{\rho}}{3} \int C(\omega)v(\omega)\Lambda(\omega,T)d\omega$ ). More than 4 orders of magnitude reduction in the effective thermal conductivity would not be practical due to the constraints implemented by additive manufacturing techniques. However, **Figure 5-2** provides the theoretical values to be achieved due to incorporating the porosity and size effect to a specified precursor.



**Figure 5-1** Thermal conductivity contour exploring diffuse to ballistic phonon transport regimes as the strut thickness and the pitch scale, respectively. Each line accounts for a constant thermal conductivity of carbon lattice structures (right). The contour model assumes the size effect in phonon transport by diffuse boundary scattering.



**Figure 5-2** Effective thermal conductivity of glassy carbon nanolattices by incorporating the porosity provided by the architecture of the unit cells.

## **5.3. Materials and Experimental Approaches**

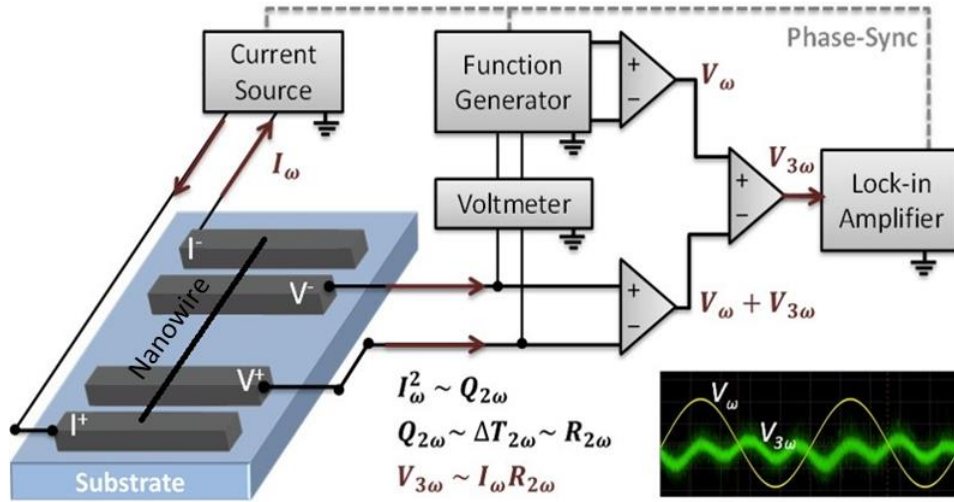
### **5.3.1. Fabrication of Glassy Carbon Structures**

Manufacturing of the glassy carbon nanowires and nanolattices consists of two production steps. First, the polymeric templates are fabricated using the 3D-DLW (Photonic Professional Nanoscribe GmbH). Then, in the subsequent pyrolysis step, the polymeric templates are transformed into glassy carbon structures in a vacuum tube furnace at 900°C. The details of the pyrolysis process can be found in [143]. During the pyrolysis, the polymeric structures shrank by roughly 80% compared to their initial polymeric template. The resulting structures were glassy carbon nanowires with an average length of 48  $\mu\text{m}$  and a diameter of 75 nm.

### **5.3.2. Electrical Resistance Thermometry**

We characterized these glassy carbon nanowires' thermal and electrical properties using electrical resistance thermometry [224]. In particular, we used the  $3\omega$  technique with a 4-probe configuration to do simultaneous measurements of the electrical and thermal conductivities from room temperature to 748K in addition to the measurement of heat capacity. The measurement was performed in a cryostat chamber (Janis VPF-800) in a high vacuum environment ( $<10^5$  Torr). A radiation shield was utilized for minimizing the radiation heat loss. We applied an increasing current (Keithley 6221) and measured both AC (25 Hz) and DC resistance of the sample using the linear region of the resulting voltage curve read by the lock-in amplifier (SR830) and multimeter (Keysight 34465A), respectively. A precise estimation of the change in resistance as a function of temperature is a crucial factor for the accurate measurement of thermal conductivity. To measure the temperature coefficient of

resistance ( $TCR = \frac{1}{R_0} \frac{dR}{dT}$ ), we used an embedded temperature controller inside the chamber (Lake shore 330) for increasing the temperature within 30mK and measured the electrical resistance after the temperature was stabilized. A platinum resistance temperature detector (RTD) was placed on top of the sample holder, and the temperature of the sample was corrected for accurate TCR measurements.



**Figure 5-3** Electrical resistance thermometry technique for thermal conductivity, electrical conductivity, and heat capacity measurement of nanowires and nanolattices.

The experimental setup for the  $3\omega$  technique is demonstrated in **Figure 5-3**. We used an alternating current at the frequency of  $\omega$  that resulted in temperature oscillation and, therefore, resistance oscillation at  $2\omega$ . Consequently, multiplication of the current at  $\omega$  and resistance at  $2\omega$  results in the third harmonic of the voltage ( $V_{3\omega} = I_{\omega} \times R_{2\omega}$ ), which carries information about the thermal conductivity of the sample. The equation below shows the correlation between the third harmonic of the voltage and the thermal conductivity [225]:

$$V_{3\omega} = \frac{4I^3 LR_0^2 TCR}{\pi^4 \kappa A_c \sqrt{1+2\omega\gamma}} \text{ with } \gamma = \frac{L^2}{\pi^2 \alpha}, \text{ when } \frac{16\epsilon\sigma_B T_0^3 L^2}{d\pi^2 \kappa} \ll 1 \quad (5-3)$$

where  $I$  is the applied current,  $R_0$  is the resistance of the sample at room temperature with no induced Joule heating,  $A_c$  is the cross-sectional area,  $L$  is the length,  $\epsilon$  is the emissivity,  $\alpha$  is the thermal diffusivity,  $d$  is the diameter of the sample, and  $\sigma_B$  is the Boltzmann constant. Notice that when  $\omega\gamma \rightarrow 0$ , thermal conductivity becomes independent of frequency and can be calculated without further knowledge of the material's thermal diffusivity. In the case of samples with 75nm average diameter and 48  $\mu m$  lengths, the maximum frequency was found to be 50 Hz. This value is derived experimentally and differs for samples with a different geometry. While this approach is rather complex, it is more sensitive to the temperature rise ( $< 1K$ ) and improves the accuracy of thermal conductivity and heat capacity measurement.

## 5.4. Results and Discussion

### 5.4.1. Electrical Conductivity Measurement

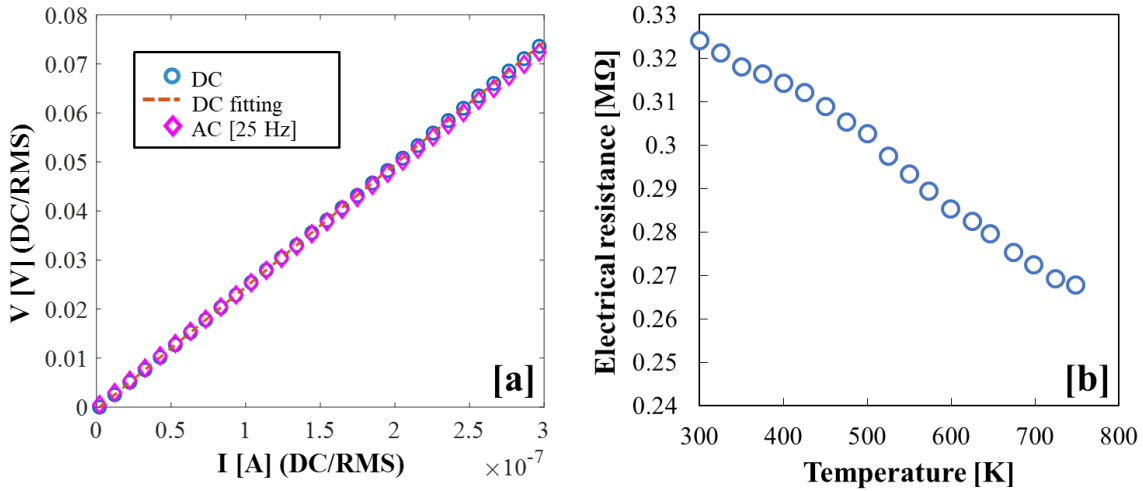
**Figure 5-4(a)** exhibits the I-V curve for both DC and AC (25 Hz) measurements at room temperature. The slope of the linear fit to the ohmic region of the I-V curve is accounted for as the electrical resistance. The resistance starts dropping when Joule heating increases the wire temperature, and in this range, both AC and DC signals start to deviate due to the heat capacity of the wire. **Figure 5-4(b)** shows the electrical resistance values as a function of temperature. Global heating of the chamber was used for heating the sample to 748K, and the temperature was corrected using a resistance temperature detector (RTD) attached on top of the chip holder. Like other carbon allotropes, the TCR is negative in glassy carbon nanowires; therefore, the resistance decreases with temperature. The electrical resistance values can be converted into electrical conductivity using the equation below:

$$\sigma = L/RA \quad (5-4)$$

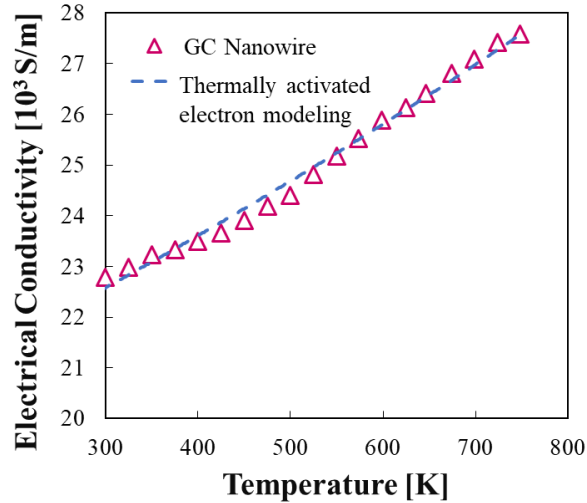
where L is the length, A is the cross-sectional area, and R is the electrical resistance of glassy carbon nanowires. As demonstrated in **Figure 5-5**, the electrical conductivity increases linearly with temperature in the studied temperature range. The dependence of electrical conductivity on temperature can be fitted using the model of the thermally activated electrons [226].[227] :

$$\sigma(T) = \sigma_0 e^{-\epsilon_a/k_B T} \quad (5-5)$$

The activated energy of the glassy carbon nanowires was 8.75 meV which corresponds to an energy of activation at 101.45K, which is in good agreement with previously reported values [228].



**Figure 5-4** a) DC and AC electrical resistance measurement at room temperature. The linear fit on the I-V curve carries information about the resistance of the wire. b) The electrical resistance has been derived using the slope of the DC linear fit to the ohmic region of the I-V curve at each average temperature.



**Figure 5-5** Electrical conductivity of the wires as a function of global heating of the chamber. The electrical conductivity increases as a result of thermally activated electrons. The dashed line represents the modeling for the thermally activated electrons.

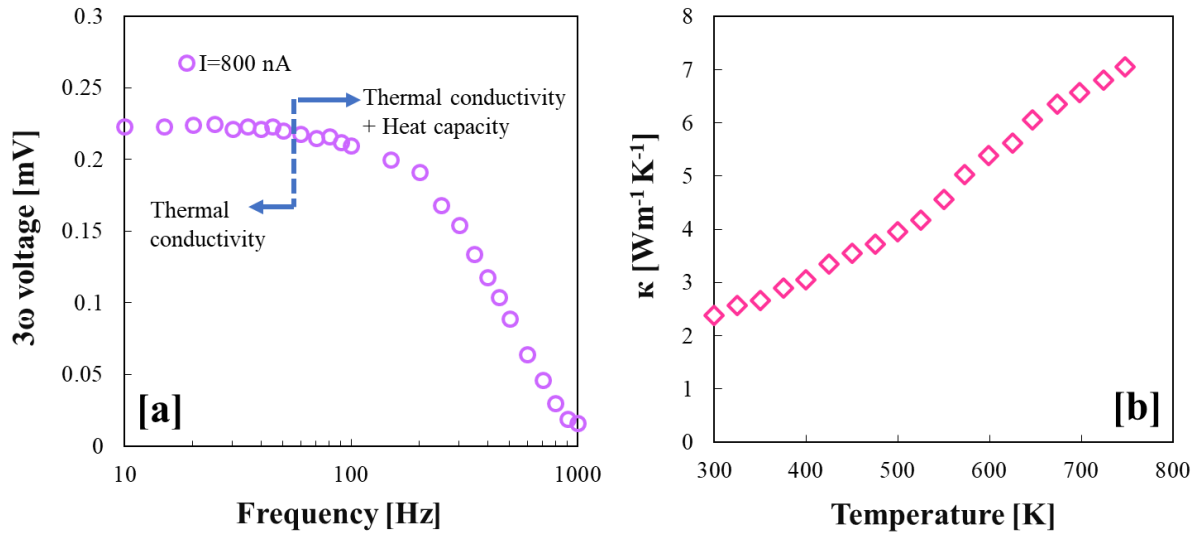
While the  $3\omega$  method is more complex than other thermal characterization techniques, it also provides a higher degree of accuracy for temperature rise. This technique can measure the thermal conductivity of glassy carbon wires with less than 1K temperature rise accuracy. Thus, this method results in more accurate measurement, mainly when the thermal conductivity changes rapidly with the temperature.

### 5.4.2. Thermal Conductivity Measurement

Utilizing the  $3\omega$  technique with a 4-probe configuration, we measured the third harmonic of the voltage by sweeping the frequency between 10-1000 Hz at a constant current value (**Figure 5-6**). The temperature rise due to the Joule heating below 50 Hz is a result of conduction and is independent of the heat capacity of the wire. Therefore, we use this frequency range for measuring the thermal conductivity using the equation below:

$$V_{3\omega} = \frac{4I^3LR_0^2TCR}{\pi^4\kappa A_c} \text{ when } \omega\gamma \rightarrow 0 \quad (5-6)$$

where  $I$  is the applied current,  $R_0$  is the resistance of the sample at room temperature with no induced Joule heating,  $A_c$  is the cross-sectional area,  $L$  is the length,  $\epsilon$  is the emissivity,  $\alpha$  is the thermal diffusivity,  $d$  is the diameter of the sample, and  $\sigma_B$  is the Boltzmann constant. Error! Reference source not found. **Figure 5-6(b)** demonstrates the thermal conductivity as a function of temperature for glassy carbon nanowires. Almost linear trend in the increase of thermal conductivity with the temperature is typical of glass-like structures. This linear trend indicates that the dominant phonon scattering mechanism is lattice disorder [229].



**Figure 5-6:** a) Swiping the third harmonic of the voltage from 10 to 1000 Hz. The values below 50 Hz are frequency-independent; therefore, we can calculate the thermal conductivity using Equation 5. The dependency of the third harmonic of the voltage on frequency contains information on the thermal conductivity and heat capacity of the glassy carbon wires. b) The thermal conductivity of glassy carbon nanowires increases as a function of temperature as an intrinsic behavior of amorphous materials.

### 5.4.3. Heat Capacity Measurement

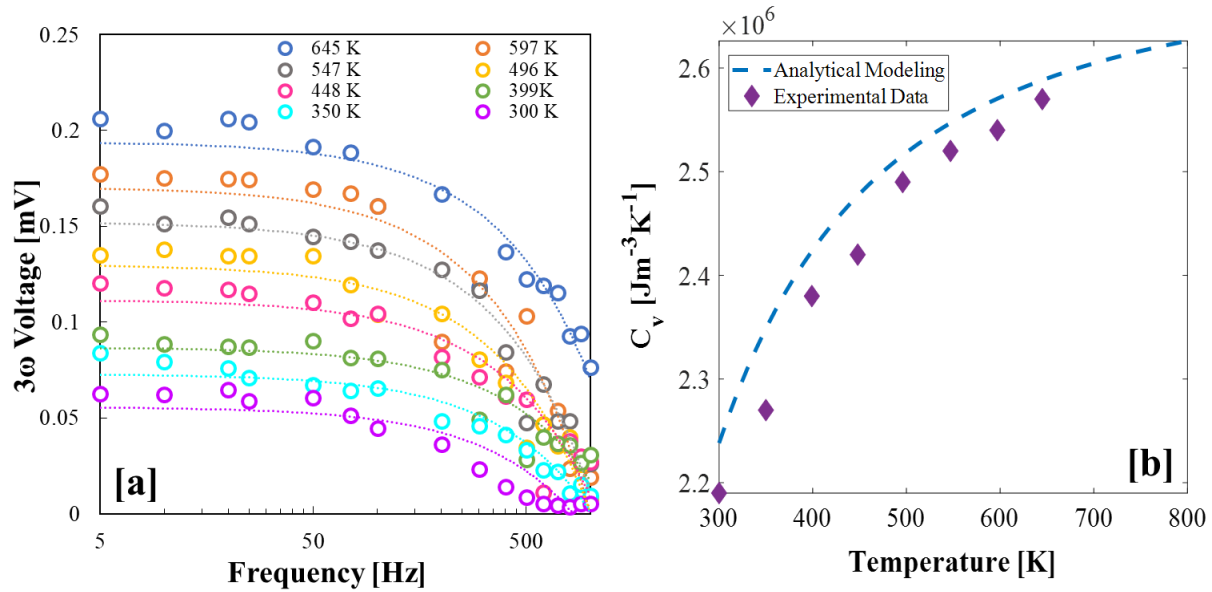
This method also allows us to characterize the heat capacity of the wires as a function of temperature. We measured the third harmonic of the voltage from 300 K- 645 K, sweeping



the frequency between 10-1000 Hz at 250 nA (**Figure 5-7 (a)**). The third harmonic of the voltage above 50 Hz is a function of frequency and contains information about the thermal conductivity and heat capacity of the glassy carbon wires. Using the previously characterized thermal conductivity of glassy carbon wires at elevated temperatures, we could extract the volumetric heat capacity as a function of temperature (**Figure 5-7 (b)**) via global heating of the stage in our JANIS VPF-800 vacuum chamber. We used the Debye model for modeling the volumetric heat capacity of phonons at elevated temperatures as stated in the equation below:

$$C_v = \frac{9n_a k_B T^3}{\theta_D^3} \int_0^{\theta_D/T} \frac{x^4 \exp(x) dx}{(\exp(x)-1)^2} \quad (5-7)$$

where  $n_a$  is the atomic number density and  $\theta_D$  is the Debye temperature. By estimating the Debye temperature as 592 K, the dashed line represents the analytical prediction of volumetric heat capacity for glassy carbon wires. It is worth mentioning that the volumetric heat capacity of diamond-like carbon is  $3.2 \times 10^6 \frac{J}{m^3.K}$  [230] while the volumetric heat capacity of graphite is  $1.4 \times 10^6 \frac{J}{m^3.K}$  [231].



**Figure 5-7:** a) Third harmonic of the voltage as a function of frequency at temperatures between 300 K to 645 K. The third harmonic of the voltage contains information about the thermal conductivity of the glassy carbon wire below 50 Hz and carries information on the heat capacity plus thermal conductivity in frequency ranges above 50 Hz b) The calculated volumetric heat capacity as a function of temperature. The dashed line represents the modeling of the volumetric heat capacity of phonons for glassy carbon nanowires.

## 5.5. Conclusions

Here, we characterized glassy carbon nanowires with an aspect ratio as large as 640, in which the nanowire length is in an average of 48  $\mu\text{m}$ , and the diameter is in an average of 75 nm. The significant length to diameter aspect ratio allowed for the characterization of the heat capacity and thermal conductivity. We used an electrical resistance thermometry technique known as the  $3\omega$  method to simultaneously characterize the glassy carbon nanowires' electrical conductivity, thermal conductivity, and heat capacity over a wide range of temperatures. The electrical conductivity of the glassy carbon nanowires increases from 22740 S/m at room temperature to 27757 S/m at 748 K, and their thermal conductivity increases from 2.4  $\text{Wm}^{-1}\text{K}^{-1}$  at room temperature to 7.0  $\text{Wm}^{-1}\text{K}^{-1}$  at 748 K. The increase in

electrical and thermal conductivities is attributed to an increasing rate in graphitization ratio as a function of temperature. The volumetric heat capacity of glassy carbon nanowires increases from  $2.2 \times 10^6 \text{ J/m}^3\text{K}$  at 300 K to  $2.6 \times 10^6 \text{ J/m}^3\text{K}$  at 645 K, and this increasing trend was captured by modeling the phonon heat capacity in solids.

# CHAPTER 6

## Summary and Conclusions

Additively manufactured thermal metamaterials have opened up a new avenue to synthesize unique physical properties in material systems by controlling previously unattainable topological designs. The properties of these engineered materials are determined by their geometrical structure rather than solely by their chemical composition and micro/nanostructure. Among various physical domains, the manipulation of thermal properties is of particular interest, motivated by the quest for better performance and energy efficiency in many engineering systems, with applications in the electronics, energy storage, automotive, and aerospace industries. This dissertation explored a novel approach for manipulating heat flows by investigating the thermal transport phenomena in micro and nanoscale architected thermal metamaterials. We started by developing a topology optimization approach for tailoring the conduction heat transfer path and employed it to define thermo-mechanically optimized heat guiding structures for thermal management in electronics. Subsequently, we implemented

analytical and experimental techniques to explore the role of architecture on the heat transfer mechanisms in different lattice material systems. The architecture design defines the conduction path for heat transfer, while the high surface-to-volume ratio of architected materials results in a significant radiation contribution, which is surprisingly dominant even at low temperatures. Since thermal transport is closely tied to the spatial configuration of the lattice architecture, reconfiguring the spatial arrangement through deformation enables a new strategy for manipulating the heat flow leading to potential programmability of thermal transport. At the end of this work, we began exploring the role of size effects on the design and performance of thermo-mechanical nanolattice materials. Novel additive manufacturing approaches based on two-photon polymerization Direct Laser Writing and pyrolysis enable fabrication of carbon nanolattices with dimensional control at a scale of  $\sim 100\text{nm}$ . While recent work demonstrated the mechanical advantage of scale reduction in these materials systems (the lack of large-scale defects enables ceramic materials to attain near-theoretical strength), its effect on thermal properties remains unexplored. Here we applied an extremely sensitive thermal metrology technique to measure thermal transfer in simple nanolattice building blocks as a function of temperature. While preliminary, these studies open the door to thermo-structural design and fabrication of nanolattice materials for high-temperature applications.

## **6.1. Contributions of the Dissertation**

- We investigated the role of topology on thermal transport in metallic heat guiding structures (Ch. 2). We developed a numerical platform for topology optimization of

metallic heat guiding structures using thermal, mechanical, and thermomechanical objective functions. The resultant structures possess a topology with optimized thermal resistance and mechanical stiffness, subject to a specific volume fraction constraint. Experimental characterization of topologically optimized 3D printed heat guiding structures demonstrates a 29% lower thermal resistance in the serpentine heat guide compared to its reference counterpart with an identical mass. The thermomechanically optimized heat guiding systems can be a stepping stone for the next generation of multifunctional thermal management solutions for electronic packaging.

- We studied the role of architecture on the thermal conductivity in hollow nickel microlattices with 99.9% porosity (Ch. 3). The high porosity of microlattices strongly limits solid conduction and makes surface radiation the dominant mechanism in thermal transport, even at relatively low temperatures. By comparing hollow nickel microlattices with smooth and rough surfaces, we studied the role of emissivity on the radiation contribution. Our analysis reveals that the sample with the highest surface-to-volume ratio and surface emissivity has the most significant radiation contribution. Additionally, the compression dependant thermal characterizations revealed that the thermal properties can be tuned due to geometry reconfiguration in recoverable lattice structures.
- We investigated a programmable thermal transport in Kelvin foam and octet truss lattice metamaterials (Ch. 4). Due to their distinctive deformation mechanisms, the two lattice topologies exhibit different thermal responses to mechanical compression. For example, in stretching-dominated octet lattices, the effective thermal conductance increases as compression progresses, while bending-dominated Kelvin foams exhibit

the opposite behavior. These findings suggest new avenues for programming the thermal transport in shape memory-based architected materials upon applying external stimuli and can be realized for developing future dynamic thermal systems.

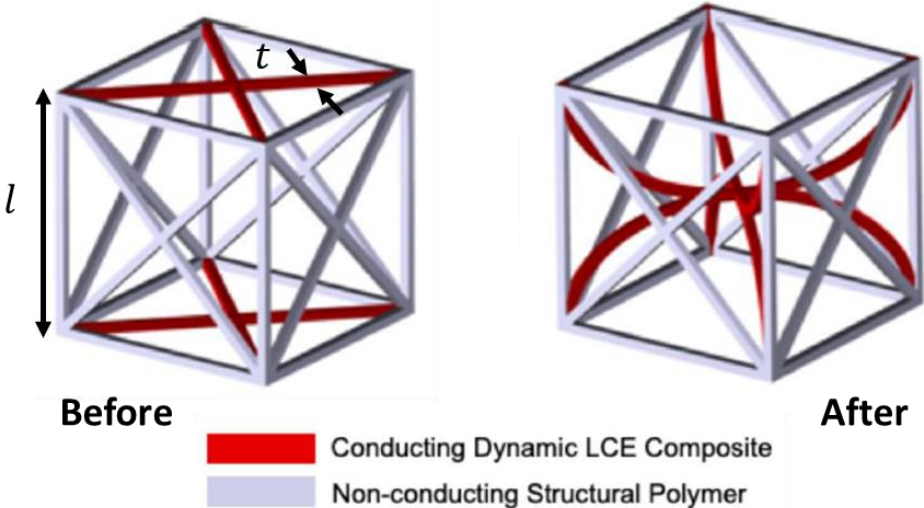
- Finally, we performed a preliminary investigation on heat flow control at the nanoscale by exploring the transition from diffusive to ballistic phonon transport in carbon nanolattices (Ch. 5). Utilizing a state-of-the-art two-step additive manufacturing process, consisting of two-photon polymerization direct laser writing followed by pyrolysis, carbon nanowires could be fabricated with an exquisite feature size of 75 nm as the building blocks of carbon nanolattices. First, the thermal and electrical properties of additively manufactured carbon nanowires were characterized using electrical resistance thermometry. Subsequently, the ultralow thermal conductivity of carbon nanolattices was analyzed by employing architecture to the carbon nanowires. By exploiting both geometric and, size effects in carbon nanolattices, combining high specific strength and low thermal conductivity can help colonize a new territory in the material property space, with unique applications in high-temperature aerospace systems.

## **6.2. Future Research Directions**

### **6.2.1. Passive thermal switches using 4D printed architected materials**

A thermal switch is a device for controlling thermal transport that provides thermal conduction or insulation upon demand. The capability of 4D printed architected materials can be utilized for programming the thermal transport, therefore designing a thermal switch. However, providing external stimuli in SMP systems is the major challenge for passive thermal control.

Liquid crystal elastomers (LCE) are a class of stimuli-responsive polymers that undergo drastic shape changes upon exposure to different stimuli such as heat or light [232][233]. In addition, LCEs can undergo a reversible shape change in the absence of external stimuli due to cross-linking in an aligned state [234]. Requiring no external loads for this reversible change makes them an ideal candidate for passive thermal applications. Furthermore, in response to heat, aligned LCEs contract along the orientation direction in liquid crystal molecules and expand in the perpendicular direction [234]. Therefore, as a result of incorporating LCE to architected materials using 4D printing additive manufacturing technique, passive thermal switches can be realized. Figure 6-1 demonstrates a passive thermal switch metamaterial with LCE struts. Upon heating, the LCE struts bend and create a thermal contact while after being cooled the lattice restores its original shape.



**Figure 6-1:** LCE-based architected materials can create a thermal connection in struts made out of LCE upon heating without any external stimuli. The structure would reverse to its original shape upon cooling. The reversible thermal contact created due to exposure to heat can be realized to define a new class of thermal switches.



We used the analytical approach discussed in Chapters 3 and 4 to identify the effective thermal conductivity of LCE-based thermal switch structures before and after the transition for a rough estimation of the switching ratio of these architected metamaterials. First, we calculated the volume fraction of the architected thermal switch as below:

$$v = 23\sqrt{2}\pi \left(\frac{t}{l}\right)^2 \quad (6-1)$$

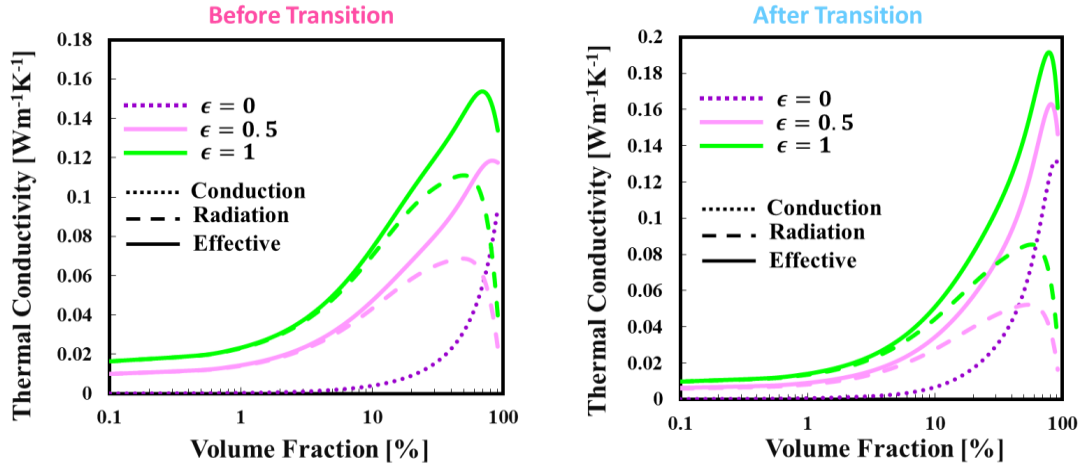
where  $t$  is the strut thickness, and  $l$  is the strut length, as demonstrated in **Figure 6-1**. We estimated the conduction contribution using FEM analysis for structures before and after the transition as below:

$$\text{Before Transition: } \kappa_{cond} \approx \frac{5}{11}v_{pol}\kappa_{pol} + \frac{11}{500}v_{LCE}\kappa_{LCE} \quad (6-2)$$

$$\text{After Transition: } \kappa_{cond} \approx \frac{5}{11}v_{pol}\kappa_{pol} + \frac{3}{10}v_{LCE}\kappa_{LCE} \quad (6-3)$$

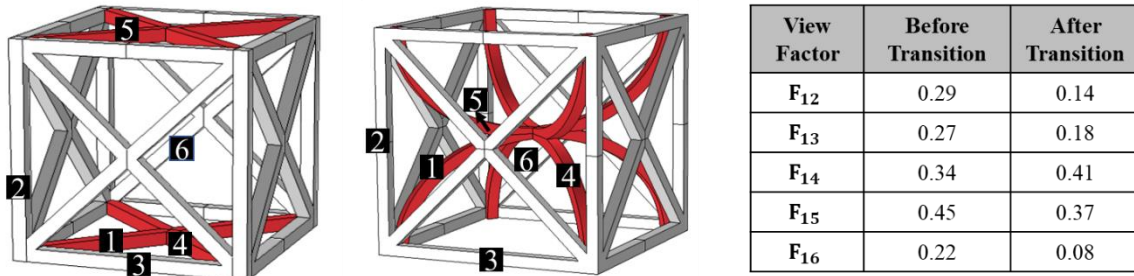
Where  $\kappa_{pol}$  is the intrinsic thermal conductivity of the structural polymer and  $\kappa_{LCE}$  is the intrinsic thermal conductivity of LCE.  $v_{pol}$  and  $v_{LCE}$  are the percentage of volume fraction dedicated to structural polymer and LCE, respectively. By assuming  $\kappa_{pol}$  to be  $0.1 \text{ Wm}^{-1}\text{K}^{-1}$  [235] and  $\kappa_{LCE}$  to be  $0.4 \text{ Wm}^{-1}\text{K}^{-1}$  [236] we examined the thermal conductivity as a function of volume fraction at different surface emissivity values. For evaluating the volume fraction, we assumed a constant strut length of  $l = 1 \text{ mm}$  and swept the thickness from  $1 \mu\text{m}$  to  $140 \mu\text{m}$ . The structures before and after the transition demonstrate an initial increase in the effective thermal conductivity dictated by the increase in conduction and radiation contributions followed by a decrease in the effective thermal conductivity as a result of a reduction in the radiation contribution at higher volume fractions. Different colors represent the investigation of the impact of surface emissivity. At higher emissivity values the effective thermal conductivity increases as a result of the increase in the radiation contribution while

at surface emissivity value of zero the effective thermal conductivity merges to the conduction contribution.



**Figure 6-2:** Thermal conductivity of LCE architected metamaterial before (Left) and after the (Right) transition. The effective thermal conductivity increases at first with the increase of volume fraction due to rising trends in conduction and radiation contributions and then decreases with the sharp reduction in the radiation contribution.

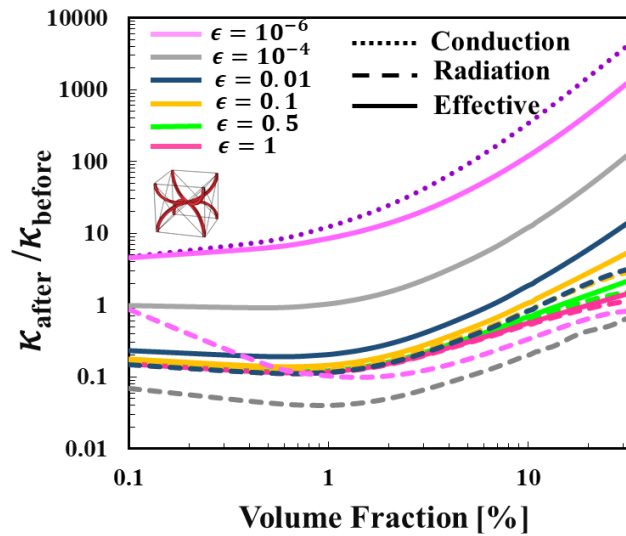
After the transition, the reconfiguration of LCE struts reduces the radiation view factor between most struts, as shown in **Figure 6-3**.



**Figure 6-3:** Reconfiguring LCE struts reduces the view factor between most struts after transition, as shown in the table.

To identify the role of radiation, we investigated the switching ratio by sweeping the surface emissivity between  $10^{-6}$  and  $10^0$  as illustrated in **Figure 6-4**. The switching ratio is defined as the effective thermal conductivity of the architected metamaterial after transition over the effective thermal conductivity before the transition. Since the LCE thermal switch mechanism

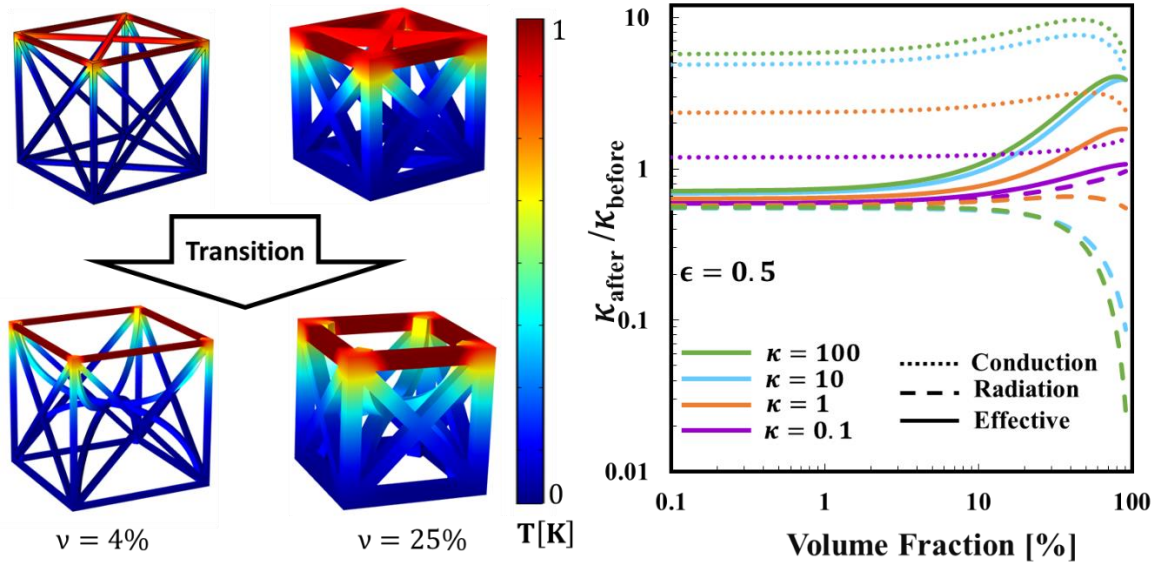
creates a thermal contact, the highest switching ratio is dedicated to the ratio of conduction contributions after and before the transition. Therefore, incorporating the radiation contributions after and before the transition. Therefore, incorporating the radiation contribution reduces the switching ratio significantly. As demonstrated in **Figure 6-4**, the switching ratio of 100 can be achieved at a volume fraction of 5% when only the conduction mode of heat transfer is considered.



**Figure 6-4:** The switching ratio of the LCE architected metamaterial as a function of volume fraction. The conduction switching ratio increases with the volume fraction; however, the radiation switching ratio first decreases then increases due to the ratio of radiative thermal conductivity trends demonstrated in Figure 6-3. The analysis is done for different surface emissivity values to identify the role of radiation. Activation of the radiation heat transfer mode deteriorates the performance of the LCE thermal switch.

We assumed the surface emissivity value of 0.5 and investigated the role of the intrinsic thermal conductivity of LCE in the final switching ratio. As demonstrated in **Figure 6-5**, the increase of volume fraction causes the conduction mode of heat transfer to take over; therefore, the switching ratio of the effective thermal conductivity values increases. On the other hand, the switching ratio of the radiative thermal conductivity decreases with the

advance of volume fraction. Consequently, activating the radiation heat transfer mode results in a decrease in the switching ratio.



**Figure 6-5:** The FEM results demonstrate the temperature distribution in the architected thermal switch at different volume fractions. The plot presents the switching ratio as a function of volume fraction with different intrinsic thermal conductivities of LCE when the thermal conductivity of the structural polymer is fixed at 0.1 Wm-1K-1. The switching ratio increases with the increase of volume fraction since conduction becomes the dominant mode of heat transfer. The increase of LCE thermal conductivity results in a larger switching ratio of the effective thermal conductivity values,

In conclusion, by modifying the volume fraction by changing the design parameter or modifying the intrinsic thermal conductivity of LCE via incorporating highly conductive fillers, we can design a thermal switch with an effective thermal conductivity smaller or larger than the initial structure for the desired application.

### 6.2.2. Thermal rectification in nanoscale architected materials

The idea of controlling the heat flux through thermal rectification in solids has been of significant interest to scientists and engineers for many years. While the early research was

focused on the impact of interfacial effects on dissimilar materials [237][238][239] to realize thermal rectification, advancement of nanomaterials provides a new opportunity for exploring rectification using surface and volumetric processes. Recent studies have demonstrated the possibility of thermal rectification in asymmetric nanostructures using molecular dynamics [240][241][242], Monte Carlo [243], and ray-tracing simulations [244]. The results of these studies indicate that thermal rectification can happen in nanostructures with feature sizes within the length of phonon mean free path by asymmetric boundary scattering effects of ballistic phonons. However, thermal rectification in asymmetric nanostructures has not been experimentally demonstrated in the literature.

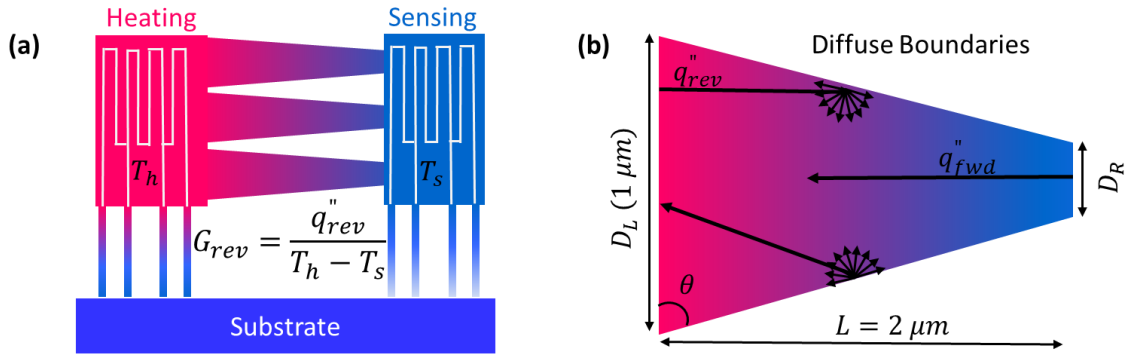
The design of carbon nanolattices by controlling size, geometry, and nanostructure can provide a platform for potential heat flux manipulation beyond classical approaches. However, understanding the heat transfer phenomena in complex nanolattices and asymmetric geometries is challenging; therefore, ray-tracing simulations can be a primary tool for studying multi-dimensional phonon scattering and investigating a potential thermal rectification in asymmetric nanostructures. Using Landauer-Büttiker formulism [245], the thermal conductance can be expressed as below:

$$G = A \int C v \langle \tau \rangle \frac{d\omega}{4} \quad \mathbf{(6-4)}$$

where  $A$  is the cross-sectional area,  $C$  is the volumetric heat capacity,  $v$  is the group velocity,  $\langle \tau \rangle$  is the average transmission coefficient, and  $\omega$  is the phonon frequency. The ray-tracing method with Monte Carlo integration can be used to identify the average transmission coefficient for asymmetric nanolattices where 300000 phonons are launched at one end in a random initial position and  $\langle \tau \rangle$  is calculated based on the ratio of transmitted phonons over

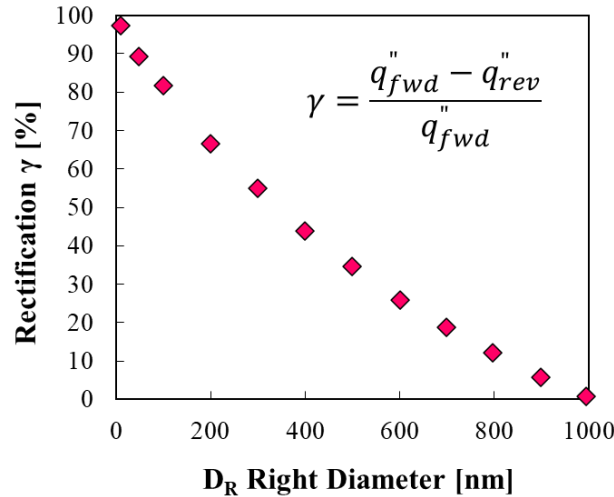
the total number of launched phonons. This method has been validated with the results published for silicon nanomeshes and nanoporous membranes [48].

The design of asymmetric struts (**Figure 6-6 (b)**) for nanolattices shows a potential thermal rectification with diffuse surface boundaries. When the surface boundaries are diffuse, the phonon transport direction becomes randomized upon boundary scattering and the heat flux ( $q_{rev}''$ ) significantly reduces from wide to narrow regions by the increase of asymmetry. However, phonon confinement [241] and changes in the phonon density of states [246] causes a more substantial reduction in the heat flux from the narrow to the wide direction ( $q_{fwd}''$ ). The mismatch in the heat flux reduction in the forward and reverse directions is the key basis for the thermal rectification.



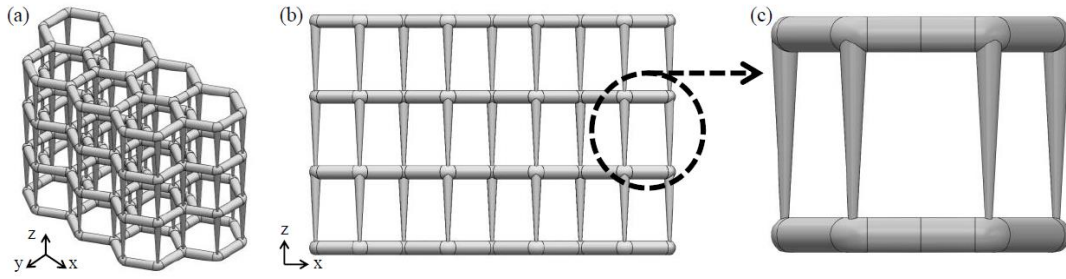
**Figure 6-6:** a) Experimental setup with heating and sensing membranes to measure thermal conductance in reverse and forward directions. b) Ray-tracing simulation setup for the asymmetric nano strut as a building block of nanolattices. The left end diameter is fixed at  $1 \mu m$ , but the right side diameter changes from  $1 \mu m$  to  $10 \text{ nm}$ . The boundaries are assumed to be diffuse.

**Figure 6-7** demonstrates the preliminary simulation results for the asymmetric cone-shaped nano strut. The rectification is scaled by the geometrical asymmetry, which directly results from the phonons entering the interface in parallel with a collimator.



**Figure 6-7:** Preliminary ray-tracing simulation results for the asymmetric nano strut demonstrated in **Figure 6-6 (b)**. The simulation considers the full detail of the geometry for ballistic phonon transport. Phonons were injected in both directions, and the rectification was calculated based on the difference between forward and reverse heat flux values over the forward heat flux value. The top and bottom surface boundaries are assumed to be periodic.

One possible lattice topology that can provide thermal rectification with the investigated asymmetric strut design is depicted in **Figure 6-8**. However, further optimizations of the structure are required for satisfying the mechanical performance and manufacturing constraints of each proposed lattice design. Therefore, integrating the ray-tracing simulation into a genetic optimizer for optimizing the geometrical parameters is required for accessing a topology that meets the optimal thermal rectification performance. The final design would then be fabricated using a combination of two-photon polymerization (2pp), direct laser writing (DLW) followed by pyrolysis in a vacuum furnace at a temperature of  $\sim 900$  °C. The resultant nanostructure comprises graphitic segments that are embedded in amorphous carbon regions [247].



**Figure 6-8:** The asymmetric nanolattice design for realizing a potential thermal rectification. The gradient in the diameter of the struts creates an asymmetric geometry.

While thermal and mechanical properties of the nanostructure are strongly affected by the processing parameters, their relationship is poorly understood. Therefore, a systematic study of the polymerization process and controlling the pyrolysis parameters for examining the phonon transport in the resultant carbon nanostructure is substantially required.



## References

- [1] J. Wang, G. Dai, and J. Huang, "Thermal Metamaterial: Fundamental, Application, and Outlook," *iScience*, vol. 23, no. 10, p. 101637, 2020.
- [2] E. M. Dede, F. Zhou, P. Schmalenberg, and T. Nomura, "Thermal Metamaterials for Heat Flow Control in Electronics," *J. Electron. Packag. Trans. ASME*, vol. 140, no. 010904, 2018.
- [3] J. C. Kim *et al.*, "Recent Advances in Thermal Metamaterials and Their Future Applications for Electronics Packaging," *J. Electron. Packag.*, vol. 143, no. 010801, 2021.
- [4] G. Park, S. Kang, H. Lee, and W. Choi, "Tunable Multifunctional Thermal Metamaterials : Manipulation of Local Heat Flux via Assembly of Unit-Cell Thermal Shifters," *Sci. Rep.*, vol. 7, no. 41000, 2017.
- [5] P. R. Bandaru, K. P. Vemuri, F. M. Canbazoglu, and R. S. Kapadia, "Layered thermal metamaterials for the directing and harvesting of conductive heat," *AIP Adv.*, vol. 5, no. 053403, 2015.
- [6] J. Bauer, L. R. Meza, T. A. Schaedler, R. Schwaiger, X. Zheng, and L. Valdevit, "Nanolattices: An Emerging Class of Mechanical Metamaterials," *Adv. Mater.*, vol. 29, no. 40, pp. 1–26, 2017.
- [7] X. Zheng, H. Lee, T. H. Weisgraber, N. X. Fang, and C. M. Spadaccini, "Ultralight, Ultrastiff Mechanical Metamaterials," *Science (80-. )*, vol. 344, no. 6190, pp. 1373–1377, 2014.
- [8] L. R. Meza, A. J. Zelhofer, N. Clarke, A. J. Mateos, D. M. Kochmann, and J. R. Greer, "Resilient 3D hierarchical architected metamaterials," 2015.
- [9] J. Valentine, S. Zhang, T. Zentgraf, E. Ulin-avila, D. A. Genov, and G. Bartal, "Three-dimensional optical metamaterial with a negative refractive index," vol. 455, no. September, 2008.
- [10] X. Ni, Z. J. Wong, M. Mrejen, Y. Wang, and X. Zhang, "An ultrathin invisibility skin cloak for visible light," *Appl. Opt.*, vol. 349, no. 6254, 2015.
- [11] S. A. Cummer and J. Christensen, "Controlling sound with acoustic metamaterials," no. 16001, 2016.
- [12] Y. Li *et al.*, "Transforming heat transfer with thermal metamaterials and devices," *Nat. Rev. Mater.*, vol. 0123456789, 2021.
- [13] J.-P. Huang, *Theoretical Thermotics: Transformation Thermotics and Extended Theories for Thermal Matamaterials*. 2020.
- [14] S. Guenneau, C. Amra, and D. Veynante, "Transformation thermodynamics: cloaking and concentrating heat flux," *Opt. Express*, vol. 20, no. 7, pp. 1777–1780, 2012.
- [15] T. Han, J. Zhao, T. Yuan, D. Y. Lei, B. Li, and C. W. Qiu, "Theoretical realization of an ultra-efficient thermal-energy harvesting cell made of natural materials," *Energy Environ. Sci.*, vol. 6, no. 12, pp. 3537–3541, 2013.

- [16] J. Y. Li, Y. Gao, and J. P. Huang, "A bifunctional cloak using transformation media," *J. Appl. Phys.*, vol. 108, no. 7, 2010.
- [17] T. Han, T. Yuan, B. Li, and C. W. Qiu, "Homogeneous thermal cloak with constant conductivity and tunable heat localization," *Sci. Rep.*, vol. 3, pp. 1–5, 2013.
- [18] S. Narayana and Y. Sato, "Heat Flux Manipulation with Engineered Thermal Materials," *Phys. Rev. Lett.*, vol. 108, no. 214303, 2012.
- [19] Y. Ma, L. Lan, W. Jiang, F. Sun, and S. He, "A transient thermal cloak experimentally realized through a rescaled diffusion equation with anisotropic thermal diffusivity," *NPG Asia Mater.*, vol. 5, no. 10, pp. 1–6, 2013.
- [20] R. Schittny, M. Kadic, S. Guenneau, and M. Wegener, "Experiments on Transformation Thermodynamics: Molding the Flow of Heat," *Phys. Rev. Lett.*, vol. 110, no. 195901, 2013.
- [21] X. Shen, Y. Li, C. Jiang, and J. Huang, "Temperature Trapping: Energy-Free Maintenance of Constant Temperatures as Ambient Temperature Gradients Change," *Phys. Rev. Lett.*, vol. 117, no. 5, pp. 1–5, 2016.
- [22] T. Han, X. Bai, J. T. L. Thong, B. Li, and C. W. Qiu, "Full control and manipulation of heat signatures: Cloaking, camouflage and thermal metamaterials," *Adv. Mater.*, vol. 26, no. 11, pp. 1731–1734, 2014.
- [23] D. M. Nguyen, H. Xu, Y. Zhang, and B. Zhang, "Active thermal cloak," *Appl. Phys. Lett.*, vol. 107, no. 12, 2015.
- [24] D. G. Baranov, Y. Xiao, I. A. Nechepurenko, A. Krasnok, A. Alù, and M. A. Kats, "Nanophotonic engineering of far-field thermal emitters," *Nat. Mater.*, vol. 18, no. 9, pp. 920–930, 2019.
- [25] K. Ikeda *et al.*, "Controlled thermal emission of polarized infrared waves from arrayed plasmon nanocavities," *Appl. Phys. Lett.*, vol. 92, no. 2, pp. 2–5, 2008.
- [26] X. Liu, T. Tyler, T. Starr, A. F. Starr, N. M. Jokerst, and W. J. Padilla, "Taming the blackbody with infrared metamaterials as selective thermal emitters," *Phys. Rev. Lett.*, vol. 107, no. 4, pp. 4–7, 2011.
- [27] M. De Zoysa, T. Asano, K. Mochizuki, A. Oskooi, T. Inoue, and S. Noda, "Conversion of broadband to narrowband thermal emission through energy recycling," *Nat. Photonics*, vol. 6, no. 8, pp. 535–539, 2012.
- [28] Y. Zhai *et al.*, "Scalable-manufactured randomized glass-polymer hybrid metamaterial for daytime radiative cooling," *Science (80-. )*, vol. 355, no. 6329, pp. 1062–1066, 2017.
- [29] S. Wijewardane and D. Y. Goswami, "A review on surface control of thermal radiation by paints and coatings for new energy applications," *Renew. Sustain. Energy Rev.*, vol. 16, no. 4, pp. 1863–1873, 2012.
- [30] Y. Li, X. Bai, T. Yang, H. Luo, and C. W. Qiu, "Structured thermal surface for radiative camouflage," *Nat. Commun.*, vol. 9, no. 1, 2018.

- [31] E. M. Dede, Z. Yu, P. Schmalenberg, and H. Iizuka, "Thermal metamaterials for radiative plus conductive heat flow control," *Appl. Phys. Lett.*, vol. 116, no. 19, p. 191902, 2020.
- [32] A. J. Jacobsen, W. Barvosa-Carter, and S. Nutt, "Micro-scale truss structures formed from self-propagating photopolymer waveguides," *Adv. Mater.*, vol. 19, no. 22, pp. 3892–3896, 2007.
- [33] X. Zheng *et al.*, "Design and optimization of a light-emitting diode projection micro-stereolithography three-dimensional manufacturing system," *Review of Scientific Instruments*, vol. 83, no. 12. 2012.
- [34] S. Maruo, O. Nakamura, and S. Kawata, "Three-dimensional microfabrication with two-photon-absorbed photopolymerization," *Opt. Lett.*, vol. 22, no. 2, p. 132, 1997.
- [35] A. Selimis, V. Mironov, and M. Farsari, "Direct laser writing: Principles and materials for scaffold 3D printing," *Microelectron. Eng.*, vol. 132, pp. 83–89, 2014.
- [36] T. A. Schaedler *et al.*, "Ultralight Metallic Microlattices," *Science (80-. )*, vol. 334, no. 6058, pp. 962–965, 2011.
- [37] L. R. Meza, S. Das, and J. R. Greer, "Strong, lightweight, and recoverable three-dimensional ceramic nanolattices," *Science (80-. )*, vol. 345, no. 6202, pp. 1322–1326, 2014.
- [38] L. J. Gibson and M. F. Ashby, *Cellular Solids: Structure and Properties, 2d ed*, vol. 2d ed. 1997.
- [39] A. Öchsner and T. Fiedler, *Effective Thermal Properties of Hollow-Sphere Structures: A Finite Element Approach*. 2008.
- [40] R. Courant and D. Hilbert, *Methods of Mathematical Physics.pdf*, 2008th ed. Wiley-VCH Verlag GmbH, 1937.
- [41] L. Gong, Y. Wang, X. Cheng, R. Zhang, and H. Zhang, "A novel effective medium theory for modelling the thermal conductivity of porous materials," *Int. J. Heat Mass Transf.*, vol. 68, pp. 295–298, 2014.
- [42] K. Pietrak and T. S. Winiewski, "A review of models for effective thermal conductivity of composite materials," *Open Access J. J. Power Technol.*, vol. 95, no. 1, pp. 14–24, 2015.
- [43] R. C. Progelhof, J. L. Throne, and R. R. Ruetsch, "Methods for predicting the thermal conductivity of composite systems: A review," *Polym. Eng. Sci.*, vol. 16, no. 9, pp. 615–625, 1976.
- [44] D. P. H. HASSELMAN AND LLOYD F. JOHNSON, "Effective Thermal Conductivity of Composites with Interfacial Thermal Tproperties," no. June, pp. 508–515, 1987.
- [45] T. H. Bauer, "A general analytical approach toward the thermal conductivity of porous media," *Int. J. Heat Mass Transf.*, vol. 36, no. 17, pp. 4181–4191, 1993.
- [46] P. G. Collishaw and J. R. G. Evans, "An assessment of expressions for the apparent thermal conductivity of cellular materials," *J. Mater. Sci.*, vol. 29, no. 2, pp. 486–498,

1994.

- [47] A. M. Marconnet, M. Asheghi, and K. E. Goodson, "From the Casimir limit to phononic crystals: 20 years of phonon transport studies using silicon-on-insulator technology," *J. Heat Transfer*, vol. 135, no. 6, pp. 1–10, 2013.
- [48] J. Lee *et al.*, "Investigation of phonon coherence and backscattering using silicon nanomeshes," *Nat. Commun.*, vol. 8, no. 14054, pp. 1–8, 2017.
- [49] and K. E. G. M. Asheghi, Y. K. Leung, S. S. Wong, "Phonon-boundary scattering in thin silicon layers," *Appl. Phys. Lett.*, vol. 71, no. 13, pp. 1798–1800, 1997.
- [50] and A. M. Deyu Li, Yiyang Wu, Philip Kim, Li Shi, Peidong Yang, "Thermal conductivity of individual silicon nanowires," *Appl. Phys. Lett.*, vol. 83, no. 14, pp. 2934–2936, 2003.
- [51] J. Lee *et al.*, "Thermal Transport in Silicon Nanowires at High Temperature up to 700 K," *Nano Lett.*, vol. 16, no. 7, pp. 4133–4140, 2016.
- [52] N. Mingo, "Calculation of Si nanowire thermal conductivity using complete phonon dispersion relations," *Phys. Rev. B*, vol. 68, no. 113308, pp. 1–4, 2003.
- [53] N. G. Dou and A. J. Minnich, "Heat conduction in multifunctional nanotrusses studied using Boltzmann transport equation," *Appl. Phys. Lett.*, vol. 108, no. 1, 2016.
- [54] N. G. Dou, R. A. Jagt, C. M. Portela, J. R. Greer, and A. J. Minnich, "Ultralow Thermal Conductivity and Mechanical Resilience of Architected Nanolattices," *Nano Lett.*, vol. 18, no. 8, pp. 4755–4761, 2018.
- [55] X. LU, M. C. ARDUINI-SCHUSTER, J. KUHN, O. NILSSON, J. FRICKE, and R. W. PEKALA, "Thermal Conductivity of Monolithic Organic Aerogels," *Science (80-. )*, vol. 255, no. 5047, pp. 971 LP – 972, Feb. 1992.
- [56] T. J. Lu and C. Chen, "Thermal transport and fire retardance properties of cellular aluminum alloys," *Acta Mater.*, vol. 47, no. 5, pp. 1469–1485, 1999.
- [57] K. Wei, R. He, X. Cheng, Y. Pei, R. Zhang, and D. Fang, "Fabrication and heat transfer characteristics of C/SiC pyramidal core lattice sandwich panel," *Appl. Therm. Eng.*, vol. 81, pp. 10–17, 2015.
- [58] C. Y. Zhao, "Review on thermal transport in high porosity cellular metal foams with open cells," *Int. J. Heat Mass Transf.*, vol. 55, no. 13–14, pp. 3618–3632, 2012.
- [59] M. Kaviany, *Principles of Heat Transfer in Porous Media*. 2006.
- [60] D. Doermann and J. F. Sacadura, "Heat transfer in open cell foam insulation," *J. Heat Transfer*, vol. 118, no. 1, pp. 88–93, 1996.
- [61] E. Placido, M. C. Arduini-Schuster, and J. Kuhn, "Thermal properties predictive model for insulating foams," *Infrared Phys. Technol.*, vol. 46, no. 3, pp. 219–231, 2005.
- [62] L. Glicksman, M. Schuetz, and M. Sinofsky, "Radiation heat transfer in foam insulation," *Int. J. Heat Mass Transf.*, vol. 30, no. 1, pp. 187–197, 1987.

- [63] J. Kuhn, H. P. Ebert, M. C. Arduini-Schuster, D. Büttner, and J. Fricke, "Thermal transport in polystyrene and polyurethane foam insulations," *Int. J. Heat Mass Transf.*, vol. 35, no. 7, pp. 1795–1801, 1992.
- [64] A. Kaemmerlen, C. Vo, F. Asllanaj, G. Jeandel, and D. Baillis, "Radiative properties of extruded polystyrene foams: Predictive model and experimental results," *J. Quant. Spectrosc. Radiat. Transf.*, vol. 111, no. 6, pp. 865–877, 2010.
- [65] D. Baillis, M. Raynaud, and J. F. Sacadura, "Spectral radiative properties of open-cell foam insulation," *J. Thermophys. heat Transf.*, vol. 13, no. 3, pp. 292–298, 1999.
- [66] J. F. Sacadura and D. Baillis, "Experimental characterization of thermal radiation properties of dispersed media," *Int. J. Therm. Sci.*, vol. 41, no. 7, pp. 699–707, 2002.
- [67] B. Zeghondy, E. Iacona, and J. Taine, "Determination of the anisotropic radiative properties of a porous material by radiative distribution function identification (RDFI)," *Int. J. Heat Mass Transf.*, vol. 49, no. 17–18, pp. 2810–2819, 2006.
- [68] J. Petrasch, P. Wyss, and A. Steinfeld, "Tomography-based Monte Carlo determination of radiative properties of reticulate porous ceramics," *J. Quant. Spectrosc. Radiat. Transf.*, vol. 105, no. 2, pp. 180–197, 2007.
- [69] S. Dubois and F. Lebeau, "Design, construction and validation of a guarded hot plate apparatus for thermal conductivity measurement of high thickness crop-based specimens," *Mater. Struct. Constr.*, vol. 48, no. 1–2, pp. 407–421, 2015.
- [70] L. S. Horst Czichos, Tetsuya Saito, *Springer Handbook of Materials Measurement Methods*. Springer Berlin, 2006.
- [71] S. Yagi and D. Kunii, "Studies on effective thermal conductivities in packed beds," *AIChE J.*, vol. 3, no. 3, pp. 373–381, 1957.
- [72] J. M. Corsan, "Axial Heat Flow Methods of Thermal Conductivity Measurement for Good Conducting Materials," *Compend. Thermophys. Prop. Meas. Methods*, no. 8, pp. 3–31, 1992.
- [73] L. Fave, M. A. Pouchon, and C. Hébert, "A radial heat flow apparatus for thermal conductivity characterisation of cylindrical samples," *J. Therm. Anal. Calorim.*, vol. 130, no. 3, pp. 1855–1863, 2017.
- [74] J. J. Healy, J. J. de Groot, and J. Kestin, "The theory of the transient hot-wire method for measuring thermal conductivity," *Phys. B+C*, vol. 82, no. 2, pp. 392–408, 1976.
- [75] L. Vozár, "A computer-controlled apparatus for thermal conductivity measurement by the transient hot wire method," *J. Therm. Anal.*, vol. 46, no. 2, pp. 495–505, 1996.
- [76] E. Solórzano, M. A. Rodríguez-Perez, and J. A. De Saja, "Thermal conductivity of cellular metals measured by the transient plane source method," *Adv. Eng. Mater.*, vol. 10, no. 6, pp. 596–602, 2008.
- [77] S. E. Gustafsson, "Transient plane source techniques for thermal conductivity and thermal diffusivity measurements of solid materials," *Rev. Sci. Instrum.*, vol. 62, no. 3,

pp. 797–804, 1991.

- [78] A. G. L. A. W. J. PARKER, R. J. JENKINS, c. P. BUTLER, “Flash Method of Determining Thermal Diffusivity, Heat Capacity, and Thermal Conductivity,” *J. Appl. Phys.*, vol. 32, no. 9, pp. 1683–1683, 1961.
- [79] J. Lee, J. Lim, and P. Yang, “Ballistic Phonon Transport in Holey Silicon,” 2015.
- [80] Z. Ren, Z. Yu, J. C. Kim, and J. Lee, “TSV-integrated thermoelectric cooling by holey silicon for hot spot thermal management,” *Nanotechnology*, vol. 30, no. 3, 2019.
- [81] D. M. Nguyen, H. Xu, Y. Zhang, and B. Zhang, “Active thermal cloak,” *Appl. Phys. Lett.*, vol. 107, no. 12, 2015.
- [82] H. Xu, X. Shi, F. Gao, H. Sun, and B. Zhang, “Ultrathin Three-Dimensional Thermal Cloak,” *Phys. Rev. Lett.*, vol. 112, no. 054301, 2014.
- [83] G. Langer, M. Leitgeb, J. Nicolics, M. Unger, H. Hoschopf, and F. P. Wenzl, “Advanced Thermal Management Solutions on PCBs for High Power Applications,” *J. Microelectron. Electron. Packag.*, vol. 11, pp. 104–114, 2014.
- [84] D. L. Saums and R. A. Hay, “Developments for Copper-Graphite Composite Thermal Cores for PCBs for High-Reliability RF Systems Expansion-Matched Substrates,” *Addit. Pap. Present.*, no. HiTEC, pp. 000073–000078, 2016.
- [85] S. S. Sapatnekar, “Addressing thermal and power delivery bottlenecks in 3D circuits,” *Proc. Asia South Pacific Des. Autom. Conf. ASP-DAC*, pp. 423–428, 2009.
- [86] E. M. Dede, T. Nomura, P. Schmalenberg, and J. S. Lee, “Heat flux cloaking, focusing, and reversal in ultra-thin composites considering conduction-convection effects considering conduction-convection effects,” *Appl. Phys. Lett.*, vol. 103, no. 063501, 2013.
- [87] J. H. Lau, “Recent advances and trends in fan-out wafer/panel-level packaging,” *J. Electron. Packag. Trans. ASME*, vol. 141, no. 4, pp. 1–27, 2019.
- [88] J. H. Lau, “Recent advances and trends in heterogeneous integrations,” *J. Microelectron. Electron. Packag.*, vol. 16, no. 2, pp. 45–77, 2019.
- [89] E. M. Dede, Y. Liu, S. N. Joshi, F. Zhou, D. J. Lohan, and J. W. Shin, “Optimal design of three-dimensional heat flow structures for power electronics applications,” *J. Therm. Sci. Eng. Appl.*, vol. 11, no. 021011, 2019.
- [90] Y. M. Xie and G. P. Steven, “A Simple Evolutionary Procedure For Structural Optimization,” *Computers & Structures*, vol. 49, no. 5, pp. 885–896, 2006.
- [91] M. P. Bendsoe, “Generating Optimal Topologies in Structural Design Using a Homogenization Method,” *Comput. Methods Appl. Mech. Eng.*, vol. 71, pp. 197–224, 1988.
- [92] J. A. Sethian and A. Wiegmann, “Structural Boundary Design via Level Set and Immersed Interface Methods,” *J. Comput. Phys.*, vol. 163, pp. 489–528, 2000.

- [93] M. Y. Wang, X. Wang, and D. Guo, "A level set method for structural topology optimization," *Comput. Methods Appl. Mech. Eng.*, vol. 192, pp. 227–246, 2003.
- [94] Y. Min, X. Yang, J. Shen, X. Yan, A. Ghaedizadeh, and J. Rong, "Designing orthotropic materials for negative or zero compressibility," *Int. J. Solids Struct.*, vol. 51, pp. 4038–4051, 2014.
- [95] O. Sigmund, "Tailoring materials with prescribed elastic properties," *Mech. Mater.*, vol. 20, pp. 351–368, 1995.
- [96] F. Wang, O. Sigmund, and J. S. Jensen, "Design of materials with prescribed nonlinear properties," *J. Mech. Phys. Solids*, vol. 69, pp. 156–174, 2014.
- [97] A. Iga, S. Nishiwaki, K. Izui, and M. Yoshimura, "Topology optimization for thermal conductors considering design-dependent effects , including heat conduction and convection," *Int. J. Heat Mass Transf.*, vol. 52, pp. 2721–2732, 2009.
- [98] J. Zhang, S. Wang, G. Zhou, and S. Gong, "Topology optimization of thermal structure for isotropic and anisotropic materials using the element-free Galerkin method," *Eng. Optim.*, vol. 52, no. 7, pp. 1097–1118, 2020.
- [99] C. Lundgaard, K. Engelbrecht, and O. Sigmund, "A density-based topology optimization methodology for thermal energy storage systems," *Struct. Multidiscip. Optim.*, vol. 60, pp. 2189–2204, 2019.
- [100] M. Zhou, J. Alexandersen, O. Sigmund, and C. B. W. Pedersen, "Industrial Application of Topology Optimization for Combined Conductive and Convective Heat Transfer Problems," *Struct. Multidiscip. Optim.*, vol. 54, pp. 1045–1060, 2016.
- [101] K. Haertel, J. Hendrik, and B. Stefanov, "Topology Optimization of an Actively Cooled Electronics Section for Downhole Tools," *Proceedings. COMSOL Conf.*, 2015.
- [102] T. Matsumori, A. Kawamoto, and T. Kondoh, "Topology optimization for thermal stress reduction in power semiconductor module," *Struct. Multidiscip. Optim.*, vol. 60, pp. 2615–2620, 2019.
- [103] C. Chen, Y. Weng, and G. Subbarayan, "Topology Optimization for Efficient Heat Removal in 3D Packages," *IEEE ITherm Conf.*, vol. 15, 2016.
- [104] D. Martínez-maradiaga, A. Damonte, A. Manzo, J. H. K. Haertel, and K. Engelbrecht, "Design and testing of topology optimized heat sinks for a tablet," *Int. J. Heat Mass Transf.*, vol. 142, no. 118429, 2019.
- [105] Y. Chen, S. Zhou, and Q. Li, "Multiobjective topology optimization for finite periodic structures," *Comput. Struct.*, vol. 88, no. 11–12, pp. 806–811, 2010.
- [106] E. M. Dede, "Simulation-Based Design and Optimization for Future Mobility Electronics Systems," *22nd Int. Conf. Therm. Mech. Multi-Physics Simul. Exp. Microelectron. Microsystems, EuroSimE 2021*, 2021.
- [107] A. Takezawa, G. H. Yoon, S. H. Jeong, M. Kobashi, and M. Kitamura, "Structural topology optimization with strength and heat conduction constraints," *Comput. Methods Appl.*

- Mech. Eng.*, vol. 276, pp. 341–361, 2014.
- [108] X. Zhu, C. Zhao, X. Wang, Y. Zhou, P. Hu, and Z. D. Ma, “Temperature-constrained topology optimization of thermo-mechanical coupled problems,” *Eng. Optim.*, vol. 51, no. 10, pp. 1687–1709, 2019.
- [109] O. Giraldo-londoño, L. Mirabella, L. Dalloro, and G. H. Paulino, “Multi-material thermomechanical topology optimization with applications to additive manufacturing : Design of main composite part and its support structure,” *Comput. Methods Appl. Mech. Eng.*, vol. 363, no. 112812, 2020.
- [110] C. Wu, J. Fang, and Q. Li, “Multi-material topology optimization for thermal buckling criteria,” *Comput. Methods Appl. Mech. Engrg.*, vol. 346, pp. 1136–1155, 2019.
- [111] Y. Du, Z. Luo, Q. Tian, and L. Chen, “Topology optimization for thermo-mechanical compliant actuators using mesh-free methods,” *Eng. Optim.*, vol. 41, no. 8, pp. 753–772, 2009.
- [112] T. Wu, J. C. Najmon, and A. Tovar, “Thermomechanical Topology Optimization of Lattice Heat Transfer Structure Including Natural Convection and Design Dependent Heat Source,” in *Proceedings of ASME 2019 International Design Engineering Technical Conferences and Computers and Information in Engineering Conference*, 2019.
- [113] M. Bruggi and A. Taliercio, “Design of masonry blocks with enhanced thermomechanical performances by topology optimization,” *Constr. Build. Mater.*, vol. 48, pp. 424–433, 2013.
- [114] L. Li, Z. Du, and H. A. Kim, “Design of Architected Materials for Thermoelastic Macrostructures Using Level Set Method,” *JOM*, vol. 72, no. 4, pp. 1734–1744, 2020.
- [115] N. De Kruijf, S. Zhou, Q. Li, and Y.-W. Mai, “Topological design of structures and composite materials with multiobjectives,” *Int. J. Solids Struct.*, vol. 44, pp. 7092–7109, 2007.
- [116] L. Li and H. A. Kim, “Multiscale Topology Optimization of Thermoelastic Structures using Level Set Method,” in *American Institute of Aeronautics and Astronautics Scitech 2020 Forum*, 2020.
- [117] E. M. Dede, “Simulation and optimization of heat flow via anisotropic material thermal conductivity,” *Comput. Mater. Sci.*, vol. 50, no. 2, pp. 510–515, 2010.
- [118] E. M. Dede, T. Nomura, and J. Lee, “Thermal-composite design optimization for heat flux shielding, focusing, and reversal,” *Struct. Multidiscip. Optim.*, vol. 49, no. 1, pp. 59–68, 2014.
- [119] G. Fujii and Y. Akimoto, “Optimizing the structural topology of bifunctional invisible cloak manipulating heat flux and direct current,” *Appl. Phys. Lett.*, vol. 115, no. 174101, 2019.
- [120] L. B. S. and O. Sigmund, “Filters in topology optimization based on Helmholtz-type differential equations,” *Int. J. Numer. Methods Eng.*, vol. 86, pp. 765–781, 2011.



- [121] E. D. Sanders, M. A. Aguiló, and G. H. Paulino, "Multi-material continuum topology optimization with arbitrary volume and mass constraints," *Comput. Methods Appl. Mech. Eng.*, vol. 340, pp. 798–823, 2018.
- [122] B. Zhang, L. Dembinski, and C. Coddet, "The study of the laser parameters and environment variables effect on mechanical properties of high compact parts elaborated by selective laser melting 316L powder," *Mater. Sci. Eng. A*, vol. 584, pp. 21–31, 2013.
- [123] M. Yakout, M. A. Elbestawi, and S. C. Veldhuis, "Influence of thermal properties on residual stresses in SLM of aerospace alloys," *Rapid Prototyp.*, vol. 26, no. 1, pp. 213–222, 2020.
- [124] D. Li, X. Zhang, Y. Guan, and J. Zhan, "Topology optimization of thermo-mechanical continuum structure," in *IEEE/ASME International Conference on Advanced Intelligent Mechatronics*, 2010, pp. 403–408.
- [125] K. Svanberg, "THE METHOD OF MOVING ASYMPTOTES-A NEW METHOD FOR STRUCTURAL OPTIMIZATION," *Int. J. Numer. Methods Eng.*, vol. 24, pp. 359–373, 1987.
- [126] K. Svanberg, "A CLASS OF GLOBALLY CONVERGENT OPTIMIZATION METHODS BASED ON CONSERVATIVE CONVEX SEPARABLE APPROXIMATIONS," *Soc. Ind. Appl. Math.*, vol. 12, no. 2, pp. 555–573, 2002.
- [127] M. P. Bendsøe and O. Sigmund, *Topology Optimization Theory, Methods and Applications*. 2004.
- [128] C. Comotti, D. Regazzoni, C. Rizzi, and A. Vitali, "Additive manufacturing to advance functional design: An application in the medical field," *J. Comput. Inf. Sci. Eng.*, vol. 17, no. 3, pp. 1–9, 2017.
- [129] J. Ivorra-Martinez, L. Quiles-Carrillo, D. Lascano, S. Ferrandiz, and T. Boronat, "Effect of infill parameters on mechanical properties in additive manufacturing," *Dyna*, vol. 95, no. 4, pp. 412–417, 2020.
- [130] J. C. Steuben, A. P. Iliopoulos, and J. G. Michopoulos, "Implicit slicing for functionally tailored additive manufacturing," *Comput. Aided Des.*, vol. 77, pp. 107–119, 2016.
- [131] S. M. Sohel Murshed and C. A. Nieto de Castro, "A critical review of traditional and emerging techniques and fluids for electronics cooling," *Renew. Sustain. Energy Rev.*, vol. 78, no. May, pp. 821–833, 2017.
- [132] M. Jung, D. Z. Pan, and S. K. Lim, "Chip/package co-analysis of thermo-mechanical stress and reliability in TSV-based 3D ICs," in *Proceedings - Design Automation Conference*, 2012, pp. 317–326.
- [133] R. Rashid, S. H. Masood, D. Ruan, S. Palanisamy, R. A. R. Rashid, and M. Brandt, "Effect of scan strategy on density and metallurgical properties of 17-4PH parts printed by Selective Laser Melting ( SLM )," *J. Mater. Process. Tech.*, vol. 249, pp. 502–511, 2017.
- [134] G. Kasperovich, J. Haubrich, J. Gussone, and G. Requena, "Correlation between porosity

- and processing parameters in TiAl<sub>6</sub>V<sub>4</sub> produced by selective laser melting," *JMADE*, vol. 105, pp. 160–170, 2016.
- [135] S. Farzinazar, T. Schaedler, L. Valdevit, and J. Lee, "Thermal transport in hollow metallic microlattices," *APL Mater.*, vol. 7, no. 101108, 2019.
- [136] M. C. K. Swamy and Satyanarayan, "A Review of the Performance and Characterization of Conventional and Promising Thermal Interface Materials for Electronic Package Applications," *J. Electron. Mater.*, vol. 48, no. 12, pp. 7623–7634, 2019.
- [137] J. Bauer, S. Hengsbach, I. Tesari, R. Schwaiger, and O. Kraft, "High-strength cellular ceramic composites with 3D microarchitecture," *Proc. Natl. Acad. Sci.*, vol. 111, no. 7, pp. 2453–2458, 2014.
- [138] A. J. Jacobsen, W. Barvosa-Carter, and S. Nutt, "Micro-scale Truss Structures formed from Self-Propagating Photopolymer Waveguides," *Adv. Mater.*, vol. 19, no. 22, pp. 3892–3896, 2007.
- [139] X. Zheng *et al.*, "Design and optimization of a light-emitting diode projection micro-stereolithography three-dimensional manufacturing system," *Rev. Sci. Instrum.*, vol. 83, no. 12, 2012.
- [140] X. Zheng *et al.*, "Multiscale metallic metamaterials," vol. 15, no. October, 2016.
- [141] L. C. Montemayor and J. R. Greer, "Mechanical Response of Hollow Metallic Nanolattices : Combining Structural and Material Size Effects," vol. 82, no. July, pp. 1–10, 2015.
- [142] T. Bückmann *et al.*, "Tailored 3D Mechanical Metamaterials Made by Dip-in Direct-Laser-Writing Optical Lithography," pp. 2710–2714, 2012.
- [143] J. Bauer, A. Schroer, R. Schwaiger, and O. Kraft, "Approaching theoretical strength in glassy carbon nanolattices," *Nat. Mater.*, vol. 15, no. 4, pp. 438–443, 2016.
- [144] E. Sadeghi, S. Hsieh, and M. Bahrami, "Thermal conductivity and contact resistance of metal foams," *J. Phys. D. Appl. Phys.*, vol. 44, no. 12, 2011.
- [145] A. Torrents, T. A. Schaedler, A. J. Jacobsen, W. B. Carter, and L. Valdevit, "Characterization of nickel-based microlattice materials with structural hierarchy from the nanometer to the millimeter scale," *Acta Mater.*, vol. 60, no. 8, pp. 3511–3523, 2012.
- [146] J. Bauer, S. Hengsbach, I. Tesari, R. Schwaiger, and O. Kraft, "High-strength cellular ceramic composites with 3D microarchitecture," *Proc. Natl. Acad. Sci.*, vol. 111, no. 7, pp. 2453–2458, Feb. 2014.
- [147] N. G. Dou, R. A. Jagt, C. M. Portela, J. R. Greer, and A. J. Minnich, "Ultralow Thermal Conductivity and Mechanical Resilience of Architected Nanolattices," *Nano Lett.*, p. acs.nanolett.8b01191, 2018.
- [148] N. H. N. Babcsa', I. Me'sza'ros, "Thermal and Electrical Conductivity Measurements on Aluminum Foams," vol. 394, pp. 391–394, 2003.

- [149] E. N. Schmieder and A. Razani, "Self-Consistent Open-Celled Metal Foam Model for Thermal Applications," *J. Heat Transfer*, vol. 128, no. November 2006, 2006.
- [150] V. V. Calmidi and R. L. Mahajan, "The Effective Thermal Conductivity of High Porosity Fibrous Metal Foams," vol. 121, no. May 1999, pp. 466–471, 1999.
- [151] X. Xiao, P. Zhang, and M. Li, "Effective thermal conductivity of open-cell metal foams impregnated with pure paraffin for latent heat storage," *Int. J. Therm. Sci.*, vol. 81, no. 1, pp. 94–105, 2014.
- [152] L. Valdevit, S. W. Godfrey, T. A. Schaedler, A. J. Jacobsen, and W. B. Carter, "Compressive strength of hollow microlattices: Experimental characterization, modeling, and optimal design," *J. Mater. Res.*, vol. 28, no. 17, pp. 2461–2473, 2013.
- [153] S. Godfrey and L. Valdevit, "A Novel Modeling Platform for Characterization and Optimal Design of Micro-Architected Materials," *53rd AIAA/ASME/ASCE/AHS/ASC Struct. Struct. Dyn. Mater. Conf.*, no. April, 2012.
- [154] D. Gall, "Electron mean free path in elemental metals," *Appl. Phys.*, vol. 085101, pp. 1–5, 2016.
- [155] F. Jeffali, B. EL Kihel, A. Nougauoui, and F. Delaunois, "Monitoring and diagnostic misalignment of asynchronous machines by infrared thermography," *J. Mater. Environ. Sci.*, vol. 6, no. 4, pp. 1192–1199, 2015.
- [156] R. C. Agarwala and V. Agarwala, "Electroless alloy / composite coatings : A review," vol. 28, no. August, pp. 475–493, 2003.
- [157] R. W. Powell, M. J. Hickman, B. P. Division, and T. National, "THE THERMAL CONDUCTIVITY OF NICKEL," vol. 8, 1965.
- [158] K. Pietrak and T. S. Wiśniewski, "A review of models for effective thermal conductivity of composite materials," *J. Power Technol.*, vol. 95, no. 1, pp. 14–24, 2014.
- [159] M. F. Ashby, "The properties of foams and lattices," *Philos. Trans. R. Soc. A Math. Phys. Eng. Sci.*, vol. 364, no. 1838, pp. 15–30, 2006.
- [160] L. Salari-Sharif, S. W. Godfrey, M. Tootkaboni, and L. Valdevit, "The effect of manufacturing defects on compressive strength of ultralight hollow microlattices: A data-driven study," *Addit. Manuf.*, vol. 19, pp. 51–61, 2018.
- [161] C. Y. Zhao, S. A. Tassou, and T. J. Lu, "Analytical considerations of thermal radiation in cellular metal foams with open cells," *Int. J. Heat Mass Transf.*, vol. 51, no. 3–4, pp. 929–940, 2008.
- [162] F. Clouet, "The Rosseland approximation for radiative transfer problems in heterogeneous media," *Quatitative Spectrosc. Radiat. Transf.*, vol. 58, no. I, 1997.
- [163] Yeram Sarkis Touloukian, R. W. Powell, C. Y. Ho, and P. G. Klemens, *Thermophysical Properties of High Temperature Solid Materials*, vol. SBN (Volum, no. 10. 1970.
- [164] T. M. Tillotson and L. W. Hrubesh, "Transparent ultralow-density silica aerogels

- prepared by a two-step sol-gel process," *J. Non. Cryst. Solids*, vol. 145, no. C, pp. 44–50, 1992.
- [165] "by Lorna Jane Gibson A dissertation submitted to the University of Cambridge for the Degree of Doctor of Philosophy Churchill College August 1981," 1981.
- [166] M. A. Worsley *et al.*, "Mechanically robust and electrically conductive carbon nanotube foams," *Appl. Phys. Lett.*, vol. 94, no. 073115, pp. 1–4, 2009.
- [167] J. L. Silverberg *et al.*, "Using origami design principles to fold reprogrammable mechanical metamaterials," *Science (80-. )*, vol. 345, no. 6197, pp. 647–650, 2014.
- [168] B. Florijn, C. Coulais, and M. Van Hecke, "Programmable mechanical metamaterials," *Phys. Rev. Lett.*, vol. 113, no. 17, pp. 1–5, 2014.
- [169] Y. Zhang, B. Li, Q. S. Zheng, G. M. Genin, and C. Q. Chen, "Programmable and robust static topological solitons in mechanical metamaterials," *Nat. Commun.*, vol. 10, no. 1, pp. 1–8, 2019.
- [170] Y. Jiang and Q. Wang, "Highly-stretchable 3D-architected Mechanical Metamaterials," *Sci. Rep.*, vol. 6, no. May, pp. 1–11, 2016.
- [171] Q. Ge, A. H. Sakhaei, H. Lee, C. K. Dunn, N. X. Fang, and M. L. Dunn, "Multimaterial 4D Printing with Tailorable Shape Memory Polymers," *Sci. Rep.*, vol. 6, no. January 2017, 2016.
- [172] J. Zhou *et al.*, "Terahertz chiral metamaterials with giant and dynamically tunable optical activity," *Phys. Rev. B*, vol. 86, no. 035448, pp. 2–7, 2012.
- [173] D. F. Gardner, J. S. Evans, and I. I. Smalyukh, "Towards reconfigurable optical metamaterials: Colloidal nanoparticle self-assembly and self-alignment in liquid crystals," *Mol. Cryst. Liq. Cryst.*, vol. 545, pp. 3/[1227]-21/[1245], 2011.
- [174] J. Y. Ou, E. Plum, L. Jiang, and N. I. Zheludev, "Reconfigurable photonic metamaterials," *Nano Lett.*, vol. 11, no. 5, pp. 2142–2144, 2011.
- [175] Q. Wang *et al.*, "Optically reconfigurable metasurfaces and photonic devices based on phase change materials," *Nat. Photonics*, vol. 10, no. 1, pp. 60–65, 2016.
- [176] T. J. Cui, M. Q. Qi, X. Wan, J. Zhao, and Q. Cheng, "Coding metamaterials, digital metamaterials and programmable metamaterials," *Light Sci. Appl.*, vol. 3, no. 10, pp. e218–e218, 2014.
- [177] Y. I. A. Al-Yasir, N. O. Parchin, R. A. Abd-Alhameed, A. M. Abdulkhaleq, and J. M. Noras, "Recent progress in the design of 4G/5G reconfigurable filters," *Electronics*, vol. 8, no. 1, 2019.
- [178] J. J. Yang, J. Borghetti, D. Murphy, D. R. Stewart, and R. S. Williams, "A family of electronically reconfigurable nanodevices," *Adv. Mater.*, vol. 21, no. 37, pp. 3754–3758, 2009.
- [179] N. I. Zheludev, "The road ahead for metamaterials," *Science (80-. )*, vol. 328, no. 5978,

pp. 582–583, 2010.

- [180] C. Z. Fan, Y. Gao, and J. P. Huang, “Shaped graded materials with an apparent negative thermal conductivity,” *Appl. Phys. Lett.*, vol. 92, no. 25, pp. 1–4, 2008.
- [181] T. Chen, C. N. Weng, and J. S. Chen, “Cloak for curvilinearly anisotropic media in conduction,” *Appl. Phys. Lett.*, vol. 93, no. 11, pp. 10–13, 2008.
- [182] M. N. Luckyanova *et al.*, “in Superlattices,” *Science (80-. )*, vol. 338, no. November, pp. 2010–2013, 2012.
- [183] J. K. Yu, S. Mitrovic, D. Tham, J. Varghese, and J. R. Heath, “Reduction of thermal conductivity in phononic nanomesh structures,” *Nat. Nanotechnol.*, vol. 5, no. 10, pp. 718–721, 2010.
- [184] B. L. Davis and M. I. Hussein, “Nanophononic metamaterial: Thermal conductivity reduction by local resonance,” *Phys. Rev. Lett.*, vol. 112, no. 5, 2014.
- [185] A. P. Raman, M. A. Anoma, L. Zhu, E. Rephaeli, and S. Fan, “Passive radiative cooling below ambient air temperature under direct sunlight,” *Nature*, vol. 515, no. 7528, pp. 540–544, 2014.
- [186] X. Nie, Y. Yoo, H. Hewakuruppu, J. Sullivan, A. Krishna, and J. Lee, “Cool White Polymer Coatings based on Glass Bubbles for Buildings,” *Sci. Rep.*, vol. 10, no. 1, pp. 1–10, 2020.
- [187] T. Han, X. Bai, D. Gao, J. T. L. Thong, B. Li, and C. W. Qiu, “Experimental demonstration of a bilayer thermal cloak,” *Phys. Rev. Lett.*, vol. 112, no. 5, pp. 1–5, 2014.
- [188] L. Zhou, S. Huang, M. Wang, R. Hu, and X. Luo, “While rotating while cloaking,” *Phys. Lett. Sect. A Gen. At. Solid State Phys.*, vol. 383, no. 8, pp. 759–763, 2019.
- [189] F. Chen and D. Yuan Lei, “Experimental Realization of Extreme Heat Flux Concentration with Easy-to-Make Thermal Metamaterials,” *Sci. Rep.*, vol. 5, no. March, pp. 1–8, 2015.
- [190] T. Han *et al.*, “Manipulating Steady Heat Conduction by Sensu-shaped Thermal Metamaterials,” *Sci. Rep.*, vol. 5, pp. 1–7, 2015.
- [191] T. A. Schaedler *et al.*, “Ultralight Metallic Microlattices,” *Science*, vol. 334, no. 6058, pp. 962–965, 2011.
- [192] H. Cui *et al.*, “Three-dimensional printing of piezoelectric materials with designed anisotropy and directional response,” *Nat. Mater.*, vol. 18, no. 3, pp. 234–241, 2019.
- [193] Z. Zhao, J. Wu, X. Mu, H. Chen, H. J. Qi, and D. Fang, “Origami by frontal photopolymerization,” *Sci. Adv.*, vol. 3, no. 4, pp. 1–8, 2017.
- [194] Z. Ding, C. Yuan, X. Peng, T. Wang, H. J. Qi, and M. L. Dunn, “Direct 4D printing via active composite materials,” *Sci. Adv.*, vol. 3, no. 4, 2017.
- [195] H. Zhang, X. Cheng, D. Yan, Y. Zhang, and D. Fang, “A nonlinear mechanics model of soft network metamaterials with unusual swelling behavior and tunable phononic band gaps,” *Compos. Sci. Technol.*, vol. 183, no. February, p. 107822, 2019.

- [196] H. Wei, Q. Zhang, Y. Yao, L. Liu, Y. Liu, and J. Leng, "Direct-write fabrication of 4D active shape-changing structures based on a shape memory polymer and its nanocomposite," *ACS Appl. Mater. Interfaces*, vol. 9, no. 1, pp. 876–883, 2017.
- [197] Z. X. Khoo *et al.*, "3D printing of smart materials: A review on recent progresses in 4D printing," *Virtual Phys. Prototyp.*, vol. 10, no. 3, pp. 103–122, 2015.
- [198] X. Kuang *et al.*, "Advances in 4D Printing: Materials and Applications," *Adv. Funct. Mater.*, vol. 29, no. 1805290, 2019.
- [199] Y. J. Li, F. H. Zhang, Y. J. Liu, and J. S. Leng, "4D printed shape memory polymers and their structures for biomedical applications," *Sci. China Technol. Sci.*, vol. 63, no. 4, pp. 545–560, 2020.
- [200] C. Yang *et al.*, "4D printing reconfigurable, deployable and mechanically tunable metamaterials," *Mater. Horizons*, vol. 6, no. 6, pp. 1244–1250, 2019.
- [201] R. Tao *et al.*, "4D printed origami metamaterials with tunable compression twist behavior and stress-strain curves," *Compos. Part B Eng.*, vol. 201, no. July, p. 108344, 2020.
- [202] Q. Ge, H. J. Qi, and M. L. Dunn, "Active materials by four-dimension printing," *Appl. Phys. Lett.*, vol. 103, no. 13, 2013.
- [203] Q. Ge, C. K. Dunn, H. J. Qi, and M. L. Dunn, "Active origami by 4D printing," *Smart Mater. Struct.*, vol. 23, no. 9, 2014.
- [204] J. Wu *et al.*, "Multi-shape active composites by 3D printing of digital shape memory polymers," *Sci. Rep.*, vol. 6, no. March, pp. 1–11, 2016.
- [205] W. Zhao, J. Zhu, L. Liu, J. Leng, and Y. Liu, "Analysis of small-scale topology and macroscale mechanical properties of shape memory chiral-lattice metamaterials," *Compos. Struct.*, vol. 262, no. January, p. 113569, 2021.
- [206] M. Lei *et al.*, "3D Printing of Auxetic Metamaterials with Digitally Reprogrammable Shape," *ACS Appl. Mater. Interfaces*, 2019.
- [207] C. Sun, N. Fang, D. M. Wu, and X. Zhang, "Projection micro-stereolithography using digital micro-mirror dynamic mask," *Sensors Actuators, A Phys.*, vol. 121, no. 1, pp. 113–120, 2005.
- [208] V. . Deshpande, N. A. Fleck, and M. . Ashby, "Effective properties of the octet-truss lattice material," *J. Mech. Phys. Solids*, vol. 49, no. 8, pp. 1747–1769, 2001.
- [209] Y. Takahashi, D. Okumura, and N. Ohno, "Yield and buckling behavior of Kelvin open-cell foams subjected to uniaxial compression," *Int. J. Mech. Sci.*, vol. 52, no. 21, pp. 377–385, 2010.
- [210] E. A. Pieczyska *et al.*, "Thermomechanical properties of polyurethane shape memory polymer-experiment and modelling," *Smart Mater. Struct.*, vol. 24, no. 4, p. 45043, 2015.
- [211] David I. Bower, "An introduction to polymer physics," *Cambridge Univ. Press*, vol. 40, no.

- 1, p. 26, 2002.
- [212] I.M. Ward and D.W Hadley, "An Introduction to the Mechanical Properties of Solid Polymers," *John Wiley Sons, Inc.*, no. 2, 2004.
- [213] Y. Liu, K. Gall, M. L. Dunn, A. R. Greenberg, and J. Diani, "Thermomechanics of shape memory polymers : Uniaxial experiments and constitutive modeling," vol. 22, pp. 279–313, 2006.
- [214] J. R. Howell, M. P. Mengüç, and R. Siegel, *Thermal radiation heat transfer, sixth edition.* 2015.
- [215] M. F. Modest, "RADIATIVE HEAT TRANSFER," *Elsevier Inc*, vol. Third ed., 2013.
- [216] G. Contento, M. Oliviero, N. Bianco, and V. Naso, "The prediction of radiation heat transfer in open cell metal foams by a model based on the Lord Kelvin representation," *Int. J. Heat Mass Transf.*, vol. 76, pp. 499–508, 2014.
- [217] M. Tancrez and J. Taine, "Direct identification of absorption and scattering coefficients and phase function of a porous medium by a Monte Carlo technique," *Int. J. Heat Mass Transf.*, vol. 47, no. 2, pp. 373–383, 2004.
- [218] X. Zheng *et al.*, "Ultralight, ultrastiff mechanical metamaterials," *Science (80-. )*, vol. 344, no. 6190, pp. 1373–1377, 2014.
- [219] J. J. do Rosário, J. B. Berger, E. T. Lilleodden, R. M. McMeeking, and G. A. Schneider, "The stiffness and strength of metamaterials based on the inverse opal architecture," *Extrem. Mech. Lett.*, vol. 12, pp. 86–96, 2017.
- [220] L. R. Meza, S. Das, and J. R. Greer, "Strong, lightweight, and recoverable three-dimensional ceramic nanolattices," *Science (80-. )*, vol. 345, no. 6202, pp. 1322–1326, 2014.
- [221] X. Wendy Gu and J. R. Greer, "Ultra-strong architected Cu meso-lattices," *Extrem. Mech. Lett.*, vol. 2, no. 1, pp. 7–14, 2015.
- [222] I. V Belova, C. Veyhl, T. Fiedler, and G. E. Murch, "Analysis of anisotropic behaviour of thermal conductivity in cellular metals," *Scr. Mater.*, vol. 65, no. 5, pp. 436–439, 2011.
- [223] J. M. Ziman, *Electrons and Phonons: The Theory of Transport Phenomena in Solids.* OUP Oxford, 2001.
- [224] D. G. Cahill, "Thermal conductivity measurement from 30 to 750 K: the  $3\omega$  method," vol. 802, no. May 1989, 2006.
- [225] L. Ferrer-Argemi, E. S. Aliabadi, A. Cisquella-Serra, A. Salazar, M. Madou, and J. Lee, "Size-dependent electrical and thermal conductivities of electro-mechanically-spun glassy carbon wires," *Carbon N. Y.*, vol. 130, pp. 87–93, Apr. 2018.
- [226] C. M. Lentz, B. A. Samuel, H. C. Foley, and M. A. Haque, "Synthesis and Characterization of Glassy Carbon Nanowires," *J. Nanomater.*, vol. 2011, pp. 1–8, 2011.

- [227] W. Bucker, "PREPARATION AND DC CONDUCTIVITY OF," vol. 12, pp. 115–128, 1973.
- [228] R. W. F. H. S. Powell, "The thermal and electrical conductivities of carbon and graphite to high temperatures," *Proc. Phys. Soc*, vol. 51, no. 1, p. 153, 1939.
- [229] L. Ferrer-argemi, A. Cisquella-serra, M. Madou, and J. Lee, "Temperature-Dependent Electrical and Thermal Conductivity of Glassy Carbon Wires," *2018 17th IEEE Intersoc. Conf. Therm. Thermomechanical Phenom. Electron. Syst.*, pp. 1280–1288, 2018.
- [230] C. J. Morath *et al.*, "Picosecond optical studies of amorphous diamond and diamondlike carbon : Thermal conductivity and longitudinal sound velocity and longitudinal sound velocity," vol. 2636, no. 1994, 2008.
- [231] D. M. Mceligot, W. D. Swank, D. L. Cottle, and F. I. Valentin, "Thermal Properties of G-348 Graphite," no. May, 2016.
- [232] D. L. Thomsen *et al.*, "Liquid crystal elastomers with mechanical properties of a muscle," *Macromolecules*, vol. 34, no. 17, pp. 5868–5875, 2001.
- [233] M. Warner, C. D. Modes, and D. Corbett, "Curvature in nematic elastica responding to light and heat," *Proc. R. Soc. A*, vol. 466, no. 2122, pp. 2975–2989, 2010.
- [234] H. Wermter and H. Finkelmann, "Liquid crystalline elastomers as artificial muscles," *E-Polymers*, vol. 1, no. 13, pp. 1–13, 2001.
- [235] C. Huang, X. Qian, and R. Yang, "Thermal conductivity of polymers and polymer nanocomposites," *Mater. Sci. Eng. R Reports*, vol. 132, no. July, pp. 1–22, 2018.
- [236] M. J. Ford *et al.*, "A multifunctional shape-morphing elastomer with liquid metal inclusions," *Proc. Natl. Acad. Sci. U. S. A.*, vol. 116, no. 43, pp. 21438–21444, 2019.
- [237] P. W. O'Callaghan, S. D. Probert, and A. Jones, "A thermal rectifier," *J. Phys. D. Appl. Phys.*, vol. 3, no. 9, pp. 1352–1358, 1970.
- [238] P. F. Stevenson, G. P. Peterson, and L. S. Fletcher, "Thermal rectification in similar and dissimilar metal contacts," *J. Heat Transfer*, vol. 113, no. 1, pp. 30–36, 1991.
- [239] R. R. Somers, L. S. Fletcher, and R. D. Flack, "Explanation of thermal rectification," *AIAA J.*, vol. 25, no. 4, pp. 513–520, 1987.
- [240] J. Lee, V. Varshney, A. K. Roy, J. B. Ferguson, and B. L. Farmer, "Thermal Rectification in Three-Dimensional Asymmetric Nanostructure," *Nano Lett.*, vol. 12, no. 7, pp. 3491–3496, 2012.
- [241] Y. Wang, A. Vallabhaneni, J. Hu, B. Qiu, Y. P. Chen, and X. Ruan, "Phonon lateral confinement enables thermal rectification in asymmetric single-material nanostructures," *Nano Lett.*, vol. 14, no. 2, pp. 592–596, 2014.
- [242] R. Dettori, C. Melis, R. Rurali, and L. Colombo, "Thermal rectification in silicon by a graded distribution of defects," *J. Appl. Phys.*, vol. 119, no. 215102, pp. 1–6, 2016.
- [243] N. A. Roberts and D. G. Walker, "Monte Carlo study of thermal transport of frequency



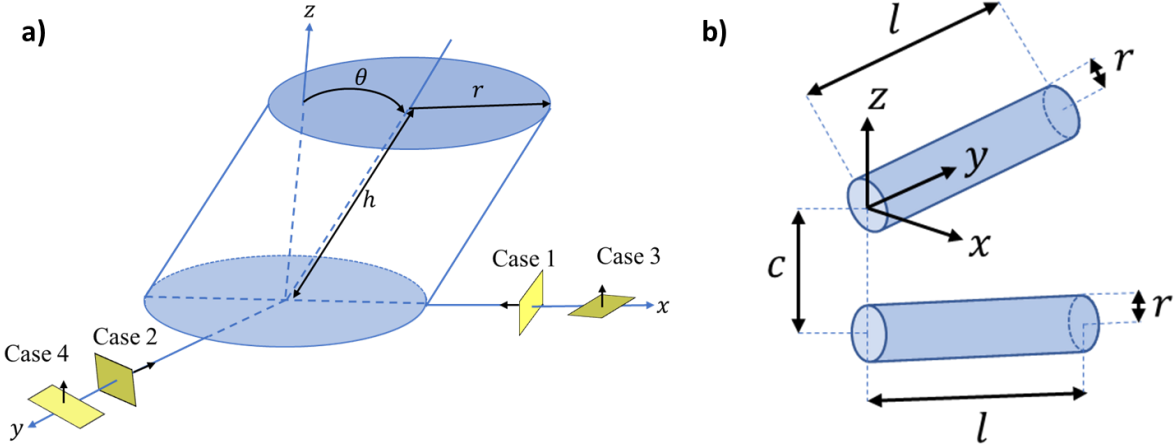
and direction dependent reflecting boundaries in high Kn systems,” in *2008 11th IEEE Intersociety Conference on Thermal and Thermomechanical Phenomena in Electronic Systems, I-THERM*, 2008, pp. 993–998.

- [244] Z. Yu, L. Ferrer-argemi, and J. Lee, “Investigation of thermal conduction in symmetric and asymmetric nanoporous structures,” *J. Appl. Phys.*, vol. 122, no. 24, pp. 1–8, 2017.
- [245] C. Jeong, S. Datta, and M. Lundstrom, “Full dispersion versus Debye model evaluation of lattice thermal conductivity with a Landauer approach,” *J. Appl. Phys.*, vol. 109, no. 7, 2011.
- [246] L. Medrano Sandonas, R. Gutierrez, A. Dianat, and G. Cuniberti, “Engineering thermal rectification in MoS<sub>2</sub> nanoribbons: a non-equilibrium molecular dynamics study,” *RSC Adv.*, vol. 5, no. 67, pp. 54345–54351, 2015.
- [247] G. S. Bisht *et al.*, “Controlled continuous patterning of polymeric nanofibers on three-dimensional substrates using low-voltage near-field electrospinning,” *Nano Lett.*, vol. 11, no. 4, pp. 1831–1837, 2011.
- [248] Henry Weckman, “Measurements of the Explosibility of Peat Dust,” *Fire Saf.*, vol. 12, pp. 97–102, 1987.
- [249] ALIASGHAR AMERI and JAMES D. FELSKE, “RADIATION CONFIGURATION FACTORS FOR OBLIQUELY ORIENTED FINITE LENGTH CIRCULAR CYLINDERS,” *Int. J. Heat Mass Transf.*, pp. 728–736, 1982.

# Appendix A

## A.1. View Factor Derivation

The topology of the lattice structure requires providing the view factors between the struts and the void space and among struts. **Figure A-0-1(a)** demonstrates the configuration of a tilted cylinder, which creates four different cases in terms of the view factors.



**Figure A-0-1:** a) Configuration factor between an inclined cylinder and planes of void surfaces b) between adjacent tilted cylinders.

Following the approach used by Henry Weckman [248], we define new variables in **Equation (A-1)** with the parameters defined in **Figure A-0-1(a)** as below:

$$\begin{aligned}
 a &= \frac{h}{r}, & b &= \frac{x}{r}, & A &= \sqrt{a^2 + (b+1)^2 - 2a(b+1)\sin\theta} \\
 B &= \sqrt{a^2 + (b-1)^2 - 2a(b+1)\sin\theta}, & C &= \sqrt{1 + (b^2 - 1)\cos^2\theta}, & D &= \sqrt{(b-1)(b+1)} \\
 E &= \frac{a \cdot \cos\theta}{b - a \cdot \sin\theta}, & F &= \sqrt{(b^2 - 1)}, & G &= \sqrt{(a^2 + b^2 + 1)^2 - 4(b^2 + a^2 \sin^2\theta)} \\
 H &= a^2 + (b+1)^2, & I &= \sqrt{(b^2 - \sin^2\theta)}
 \end{aligned}$$

**(A-1)**

Utilizing the new variables, the view factor for each of the 4 cases are listed below:

**Case 1:**

$$\begin{aligned}
 \pi F_v &= -E \tan^{-1} D + E \left[ \frac{a^2 + (b+1)^2 - 2b(1+a \cdot \sin\theta)}{AB} \right] \tan^{-1} \left( \frac{AD}{B} \right) + \frac{\cos\theta}{C} \left[ \tan^{-1} \left( \frac{AB - F^2 \sin\theta}{FC} \right) + \right. \\
 &\left. \tan^{-1} \left( \frac{F \sin\theta}{C} \right) \right]
 \end{aligned}$$

**(A-1(a))**

**Case 2:**

$$\begin{aligned}
 2\pi F_v &= - \left( \frac{a^2 \sin\theta \cos\theta}{2(a^2 \sin^2\theta + b^2)} \right) \ln \left[ \frac{a^2 + b^2 - 1 - \frac{2aF}{b} \sin\theta}{a^2 + b^2 - 1 + \frac{2aF}{b} \sin\theta} \right] + \left( \frac{\cos\theta}{I} \right) \left[ \tan^{-1} \left( \frac{ab + \sin\theta}{I} \right) + \tan^{-1} \left( \frac{ab - \sin\theta}{I} \right) \right] + \\
 &\left( ab \cdot \frac{\cos\theta}{b^2 + a^2 \sin\theta} \right) \left( \frac{a^2 + b^2 + I}{G} \right) \left[ \tan^{-1} \frac{HD - 2a \cdot \sin\theta}{G} + \tan^{-1} \frac{HD + 2a \cdot \sin\theta}{G} \right] - \left( 2ab \cdot \frac{\cos\theta}{b^2 + a^2 \sin\theta} \right) \tan^{-1} D
 \end{aligned}$$

**(A-1(b))**

**Case 3:**

$$\begin{aligned}
 \pi F_h &= \tan^{-1} \left( \frac{1}{D} \right) + \frac{\sin\theta}{C} \left[ \tan^{-1} \left( \frac{ab - F^2 \sin\theta}{FC} \right) + \tan^{-1} \left( \frac{F \sin\theta}{C} \right) \right] - \\
 &\left[ \frac{a^2 + (b+1)^2 - 2(b+1+ab \cdot \sin\theta)}{AB} \right] \tan^{-1} \left( \frac{AD}{B} \right)
 \end{aligned}$$

**(A-1(c))**

**Case 4:**

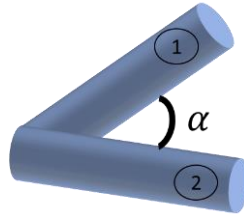
$$2\pi F_h = 2 \tan^{-1} \left( \frac{1}{D} \right) + \left( \frac{F \sin \theta}{I} \right) \left[ \tan^{-1} \left( \frac{ab + \sin \theta}{I} \right) - \tan^{-1} \left( \frac{ab - \sin \theta}{I} \right) - 2 \tan^{-1} \left( \frac{\sin \theta}{I} \right) \right] - \left( \frac{a^2 + b^2 - 1}{G} \right) \left[ \tan^{-1} \left( \frac{HD - 2a \sin \theta}{G} \right) + \tan^{-1} \left( \frac{HD + 2a \sin \theta}{G} \right) \right] \quad (\text{A-1(d)})$$

Following the approach provided by Ameri *et al.*[249], we use the geometric parameters specified in **Figure A-0-1(b)** for changing the variables in **Equation (A-2)**, and we calculate the view factor in **Equation (A-2(a))**.

$$C = \frac{c}{r}, L = \frac{l}{r}, X = 2.42C - 2.24 \quad (\text{A-2})$$

$$F_{1-2} = 0.089 \left( \frac{X}{2.59} \right)^{-0.95} \left( \frac{L}{X} \right)^{-0.16} \exp \left( -\frac{1}{1.86} \left| \frac{\ln L}{X} \right|^{1.61} \right) \quad (\text{A-2(a)})$$

Lastly, the view factor of adjacent equal struts at an angle of  $\alpha$ , as demonstrated in, is calculated (**Equation A-3**) using the approach introduced by Howell *et al.* [214].



**Figure A-0-2:** Schematic of adjacent equal bars located at an angle of  $\alpha$  towards each other.

**Figure A-0-2** demonstrates the schematic of adjacent equal bars located at an angle of  $\alpha$  towards each other.

$$F_{1-2} = F_{2-1} = 1 - \sin \left( \frac{\alpha}{2} \right) \quad (\text{A-3})$$